UC Berkeley
UC Berkeley Electronic Theses and Dissertations

Title

Ultra-low field MRI of prostate cancer using SQUID detection

Permalink

https://escholarship.org/uc/item/5bc9x0rr

Author

Busch, Sarah Elizabeth

Publication Date

2011

Peer reviewed|Thesis/dissertation

Ultra-low field MRI of prostate cancer using SQUID detection

by

Sarah Elizabeth Busch

A dissertation submitted in partial satisfaction of the

requirements for the degree of

Doctor of Philosophy

in

Physics

in the

Graduate Division

of the

University of California, Berkeley

Committee in charge:

Professor John Clarke, Chair
Professor Erwin Hahn
Professor Steven Conolly

Spring 2011

Ultra-low field MRI of prostate cancer using SQUID detection

© 2011

Sarah Elizabeth Busch

Abstract

Ultra-low field MRI of prostate cancer using SQUID detection

by

Sarah Elizabeth Busch

Doctor of Philosophy in Physics

University of California, Berkeley

Professor John Clarke, Chair

In this dissertation, I investigate various applications of prepolarized magnetic resonance imaging (MRI) at ultralow fields, typically at 132 µT, detected with a superconducting quantum interference device (SQUID). One of the major advantages of working at ultralow fields is enhanced longitudinal-relaxation-time (T_1)-weighted contrast. I measure T_1 of healthy and cancerous prostate tissue specimens—within a few hours of their surgical removal—from approximately 50 patients. The measurements involve a field-cycling imaging technique in which I prepolarize protons in fields up to 150 mT. After this field turns off, the image of each pair of samples is encoded using magnetic field gradients, and the proton nuclear magnetic resonance signal is measured using a SQUID inductively coupled to an untuned, second-derivative gradiometer. The observed T_1 contrast is significantly greater than that at (say) 1.5 T, suggesting that one may be able to distinguish tumors from healthy tissue without a contrast agent: on average I find that T_1 of 100% tumor is 66% that of 100% normal prostate tissue. To make this imaging system suitable for *in vivo* imaging of human prostates, I integrate a 200-A, 150-mT prepolarizing coil that will adequately polarize the human prostate. Assuming a prepolarizing field of 150 mT at the prostate, and a noise of 0.2 fT $Hz^{-1/2}$, we can acquire a T_1-weighted contrast image of the prostate with resolution 2×2×3 mm^3 in 22 minutes with a contrast-to-noise ratio of 4. Measurements of preliminary standard phantoms designed by NIST in Boulder, CO for measuring T_1, proton density, and resolution are discussed. I also present calculations for a method of tuning the input coil of the SQUID at low frequencies (~10 kHz) while adding minimal noise. This tuning would be useful to block very low frequency, high amplitude drifts of the ambient second-order gradient magnetic field while preserving the high balance of the gradiometer.

Contents

List of figures

List of tables

Acknowledgments

First, I am deeply grateful to my advisor, Professor John Clarke, for his encouragement, guidance, and support over the course of my graduate study. I thank Prof. Ivo Souza and Prof. Michael Lustig, who served on my qualifying exam committee, Prof. Steve Conolly who read my dissertation, and Prof. Erwin Hahn, who did both.

I thank our collaborators at UCSF for their efforts in the cancer studies, especially Jeff Simko, Kevin Chew, Lars Schmidt, and Kyle Kuchinsky. Ben Inglis, Rick Redfern, Steve Conolly were all a big help in this project, bringing with them experience in MRI and medical MRI techniques.

The work done for the second generation MRI system would have taken much longer and been much less enjoyable if it were not for the skilled work, dedication, and spirit of the undergraduates that have passed through the lab – thank you to Adam Hunt, Peter Koo, Sal Barriga, Travis Wong, Kevin Lee, and Matthew Nichols. Thank you to Dr. Darin Kinion for his carpentry work on the coil systems. The MRI project has given me a chance to work briefly with many wonderful people including Dr. Whittier Myers, Koos Zevenhoven, Fredrik Öisjöen, and Dr. Paul SanGiorgio. I am glad to know them and wish I could have worked with them longer.

The Clarke group has been an excellent support structure for everything from physics to social gatherings to swimming. I am indebted to all of them: Dr. Shane Cybart, Stephen Wu, Steve Anton, Sean O'Kelley, Jeffrey Birenbaum, Dr. Travis Hime, Dr. Paul Reichardt, Jed Johnson, and Dr. Emile Hoskinson. I gratefully acknowledge Barbara Salisbury for her help throughout my time in grad school.

When I joined the MRI project, I shadowed Dr. Michael Moessle, learning the techniques for optimal operation of the MRI system. He was very patient with me, and I appreciate his friendship and instruction. I learned general lab techniques and much more from Dr. Michael Hatridge, who was a friend throughout our time at Berkeley. He and I were a good team, through classes and MRI research. I would have been lost without him. I also thank Dr. Nathan Kelso for many discussions on physics, the history of the MRI system, and navigating graduate school, and for always having an entertaining tidbit of this or that to share.

I thank my good friends Monica Smith and Shannon McCurdy for centering me. Monica did a rotation with the MRI project, and we became great friends – someone I could call at any time of day for commiseration or celebration. Shannon was a friend from the beginning. We relied on each other to be a sounding board for ideas and a trouble-shooter for problems.

I am grateful to my family for their support through the years. Above all, I am immensely thankful for my husband David for his tolerance, encouragement, and love. Without him, I would not be where I am today.

Chapter 1

Introduction

Magnetic resonance imaging (MRI) is a very powerful, noninvasive imaging technique [1]. It is useful for distinguishing soft tissues in the human body, such as the diagnosis of brain disease. MRI is based on nuclear magnetic resonance (NMR) of protons in a magnetic field B_0. The magnetization M of the sample scales linearly with the strength of B_0. The protons precess about B_0 at their Larmor frequency $\omega_0 = \gamma B_0$, where γ is the gyromagnetic ratio. For hydrogen, $(\gamma/2\pi) \approx 42.6$ MHz/T. The spatial distribution of the magnetization is determined by the application of magnetic field gradients. In clinical MRI systems, B_0 is produced by a superconducting solenoid with magnitude around 1.5 T, so that protons precess at a frequency of 64 MHz. The precessing protons generate an oscillating magnetic field which is coupled to a nearby detection coil. An oscillating voltage V is induced in the coil with an amplitude that, by Faraday's Law, scales as $\omega_0 M$. Since M itself scales as ω_0, V scales as ω_0^2 or B_0^2. With a higher signal-to-noise ratio, images can be acquired with higher resolution or in a shorter time, so it has been the trend for MRI research to concentrate on imaging at higher fields, even up to 7 T.

However, because of various advantages of MRI at ultralow fields in the microtesla range (ULF MRI), there has also been interest in developing lower field imagers. For example, at lower fields, the imaging system has the possibility to be cheaper and more open, with lower constraints on the precision of magnet fabrication [2]. Because susceptibility artifacts are dramatically decreased at lower fields, images can be acquired in the presence of metal such as titanium implants [3,4]. In many cases, tissues can be distinguished better because the difference in their longitudinal relaxation times is enhanced [5,6]. This can result in low field images distinguishing features which are invisible to conventional imaging, for example, certain cancers.

To combat the decrease in signal from using a smaller B_0 field, the nuclear spins can be prepolarized [7] in a field B_p which can be several orders of magnitude larger than the B_0 field. Thus the magnetization of the sample is independent of B_0. To overcome the sensitivity loss of Faraday detectors at low frequency, sensitive magnetometers based on the Superconducting QUantum Interference Device (SQUID) are used to detect the NMR and MRI signals [8]. This dissertation describes the applications of such an ULF MRI system, with $B_0 = 132$ µT.

To push the ULF MRI technology toward medical applications, we have investigated the feasibility of using this technology to distinguish tissues where conventional imaging has a difficult time. For example, we have examined prostate cancer, where high field imaging requires a multiparametric T_2 MRI/^{1}H MRSI/DTI/DCE exam at 3T [9], but the cost of such a multiparametric exam is very high, limiting its clinical utility. If the contrast between the cancer and normal tissue is enhanced at ULF, then ULF MRI, with its lower cost and infrastructure requirements, may be a useful non-invasive imaging modality to integrate into the prostate cancer treatment options. It could be used, for example, to guide biopsies, and to monitor active surveillance patients. In this dissertation, we investigate the T_1 of prostate tumors and normal tissue *ex vivo*, with the conclusion that T_1 does indeed change relative to the percentage of tumor in each voxel.

There are still many avenues in parameter space that we can explore if we were able to acquire images of the prostate *in vivo*. However, imaging a specimen at the distance of the prostate *in vivo* requires a much more powerful prepolarizing coil than we originally used, and in fact required a redesign of the entire prepolarizing technology. Our previous prepolarizing coil technology used litz wire combined with liquid nitrogen pre-cooling to dissipate the heat generated by the pulse. The current density in this case could never be high enough, so we changed our design to hollow copper tubing, where water is flowed continuously through the windings to dissipate the 20 kW of power. We luckily received a spare coil from Steve Conolly and adapted the electronics designed by his group to our purpose [10].

This dissertation is organized in the following way. Chapter 2 gives a brief introduction to the dc SQUID, flux transformers, and the readout electronics used in this system. Chapter 3 describes the basic principles of NMR including polarization and precession. Chapter 3 also introduces the concepts of MRI, including a brief description of the use of gradients, *k*-space, and T_1 and T_2 time constants and their effect on imaging. I also describe the typical pulse sequences used in this dissertation. Chapter 4 gives an overview of the MRI system including the details of the dewar and SQUID readout, the magnetic field coils, and the aluminum shielding surrounding the entire system. Chapter 5 describes the implementation of the large, water-cooled prepolarizing coil, along with the issues encountered and the solutions we have employed. In Chapter 6, I present data acquired from phantoms developed by NIST, assisting in developing some low field MRI standards for T_1, proton density, and resolution. Chapter 7 contains the prostate cancer data, along with calculations and phantom images to analyze the system performance requirements for *in vivo* imaging. Chapter 8 contains a model for tuning the SQUID input circuit and the advantages of tuning.

Chapter 2

SQUID fundamentals

The dc Superconducting QUantum Interference Device (SQUID) is an extremely sensitive magnetic flux to voltage transducer. State-of-the-art devices operated at 4.2 K have a sensitivity of 1 $\mu\Phi_0$ in a 1 Hz bandwidth. The application of SQUIDs is extremely versatile. They are able to measure any quantity that can be converted to magnetic flux, such as magnetic susceptibility, current, voltage, or mechanical displacement. In this chapter, I give a brief overview of SQUIDs. A more detailed treatment can be found in [11] and references therein.

2.1 Flux quantization in superconductors and Josephson junctions

The operation of a SQUID is based on two phenomena in superconductivity [12]: flux quantization and the Josephson effect. Flux quantization arises from the requirement that the macroscopic wave function of the Cooper pairs in a superconductor,

$$\psi(\boldsymbol{r}) = \sqrt{n(\boldsymbol{r})}\, e^{i\theta(\boldsymbol{r})}, \tag{2.1}$$

must be single valued in going once around a superconducting loop (where n is the density of Cooper pairs and θ is the phase). The flux threading the loop is quantized in units of $\Phi_0 = h/2e \approx 2.07 \times 10^{-15}\ Tm^2$ (h is Planck's constant and e is the charge of the electron), and the phase around the loop changes by $2\pi n$, where n is the number of enclosed flux quanta.

When a superconducting path is interrupted by a weak link (known as a Josephson junction), typically consisting of a thin layer of insulating or normal-conducting material, a phase difference $\varphi = \theta_1 - \theta_2$ is allowed across the weak link [13]. The dc Josephson effect states that a zero voltage supercurrent can flow across a junction and that its magnitude is related to the phase difference by

$$I = I_c \sin\varphi, \tag{2.2}$$

where I_c is the critical current, the maximum supercurrent the junction can support.

As the current through the junction is increased from zero, the flow of Cooper pairs constitutes a supercurrent and the voltage across the junction remains zero until the current exceeds the

critical current. At higher currents, the phase difference evolves according to Equation 2.3, and a voltage appears across the junction, given by

$$\frac{d\varphi}{dt} = \frac{2e}{\hbar}V. \tag{2.3}$$

2.2   The dc SQUID and readout electronics

A dc SQUID consists of 2 resistively shunted Josephson junctions in parallel on a superconducting loop (Figure 2.1A). Assuming identical junctions, the critical current of the SQUID is

$$I = I_c(\sin\varphi_A + \sin\varphi_B), \tag{2.4}$$

where φ_A and φ_B represent the phase difference across the junctions A and B. From fluxoid quantization in a superconducting ring, the phases are constrained by

$$\varphi_A - \varphi_B = 2\pi\Phi/\Phi_0 \ (\text{mod } 2\pi), \tag{2.5}$$

where Φ is the flux enclosed in the SQUID loop. These two equations combined show that the maximum critical current of the SQUID for a given applied flux is

$$I_m = 2I_c|\cos\pi\Phi/\Phi_0|. \tag{2.6}$$

Equation 2.6 is a periodic function of flux, with a period of one flux quantum. The critical current is a maximum when $\Phi = n\Phi_0$, and minimum when $\Phi = (n+1/2)\ \Phi_0$ (n is an integer). The current-voltage characteristic of a SQUID is shown in Figure 2.1B. If an appropriate constant bias current $I_b > 2I_c$ is applied, a voltage appears across the SQUID which is also periodic in applied flux (Figure 2.1C)

Although it is possible simply to count the flux quanta as the external magnetic field is changed, this procedure will not make use of the full sensitivity of a SQUID. For this reason, one
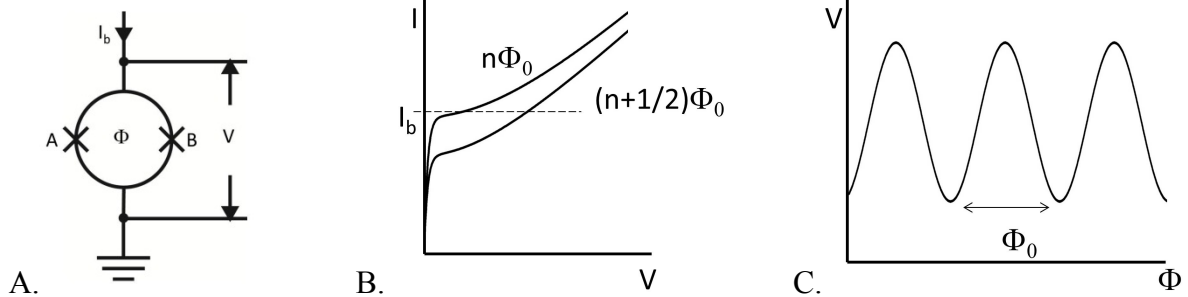
Figure 2.1. Principle of a SQUID. A: Schematic showing two Josephson junctions, A and B (marked "x") connected in parallel on a superconducting loop. A current, I, flows through the SQUID, and above a threshold current, a voltage, V, is developed across it. A flux Φ threads the loop. The device is typically operated with a constant current bias, I_b, which is larger than the critical current. B: Current-voltage characteristic for integer (n) and half-integer (n + ½) values flux threading the SQUID loop. C: Voltage, V, across the SQUID versus applied flux for fixed bias current through the SQUID.
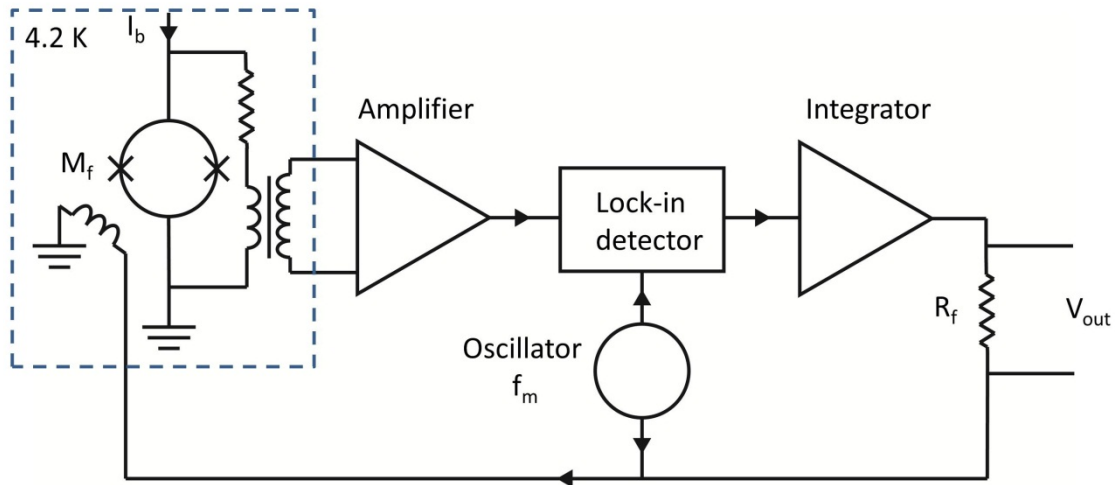
Figure 2.2. Flux modulation and feedback circuit for the dc SQUID.

A.   B.
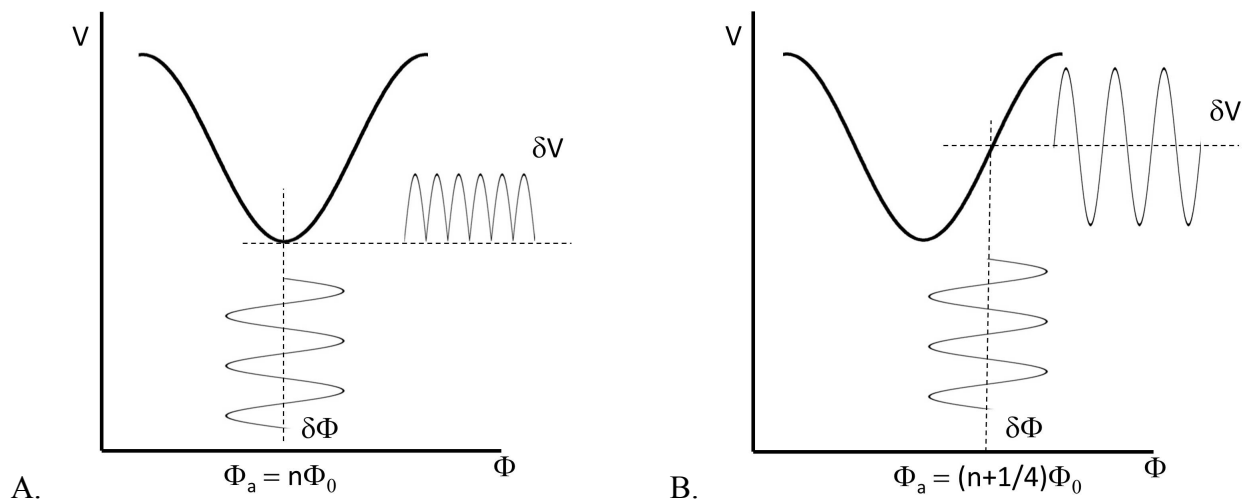
Figure 2.3. Flux modulation of the dc SQUID. A: The quasi-static applied flux is $\Phi_a = n\Phi_0$. The voltage response has a component at $2f_m$, but not at f_m. B: The quasi-static applied flux is $\Phi_a = (n+1/4) \Phi_0$. The voltage response to the flux modulation at frequency f_m has a component that is also at f_m.

generally operates the SQUID in a feedback circuit as a null detector for magnetic flux. This is achieved by passing a current through a small coil located close to the SQUID, called the feedback coil. As the magnetic flux through the SQUID changes, the corresponding voltage across the SQUID changes as well. The SQUID electronics now change the current through the feedback coil until the magnetic flux from the feedback coil cancels the externally applied flux. The feedback current is sensed as a voltage across a resistor in that circuit, and this voltage is linear in applied flux. This allows measurement of very large ($\gg \Phi_0$) and very small ($\ll \Phi_0$) changes in applied flux. The response of the SQUID itself is independent of frequency, but the response of the feedback loop is limited to one-half of the modulation frequency.

A circuit diagram for the SQUID readout electronics is shown in Figure 2.2. A bias current I_b is applied to the SQUID. A modulating flux is applied to the SQUID via the feedback coil, with a

peak-to-peak amplitude of about $\Phi_0/2$ and a frequency f_m (2 MHz in this case). The resulting voltage across the SQUID is amplified by a cold transformer, amplified again in the electronics, and fed into a lock-in detector referenced to the modulation frequency f_m. If the quasi-static flux in the SQUID is exactly $n\Phi_0$ (Figure 2.3A), the resulting voltage across it is a rectified version of the input signal. Thus, it contains frequency components at $2nf_m$, but no component at f_m, and the output of the lock-in amplifier referenced to f_m will be 0. No voltage is supplied to the integrator and the current through the feedback coil will not change. If, on the other hand, the quasi-static flux is different from $n\Phi_0$ (Figure 2.3B), the voltage across the SQUID has a frequency component at f_m, which is a maximum for a flux $(n+1/4) \Phi_0$. After integration, the signal from the lock-in is coupled via a resistor to the same coil as that producing the flux modulation. The voltage change across the feedback resistor V_{out} is proportional to the change in the applied flux.

2.3   Flux transformers

A SQUID is intrinsically a detector of magnetic flux. Its sensitivity to magnetic field is determined by its flux sensitivity divided by the effective area of the detector. To increase its effective area, and thus its sensitivity to magnetic fields, low T_c SQUIDs are often operated in conjunction with a superconducting flux transformer, consisting of a large area pickup coil (inductance L_p, area A_p) tightly coupled to the sample, and an input coil (inductance L_i), which is tightly coupled to the SQUID washer (inductance L_{SQ}) with mutual inductance $M_i = \alpha\sqrt{L_i L_{SQ}}$ (α is the coupling constant). The input coil is typically fabricated onto the SQUID itself, separated by an insulating layer.

The use of a flux transformer (Figure 2.4) allows the SQUID to be placed in a separate superconducting shield, such as a niobium shield in this case, to protect it from large time-varying magnetic fields, like those used in an NMR experiment, that could potentially trap flux in the SQUID causing a lower critical current and higher noise. Additionally, the input signal can be filtered by placing an RC shunt across the input coil. Further protections, such as an array of 20 Josephson junctions, can be added to protect the input coil from large currents caused by
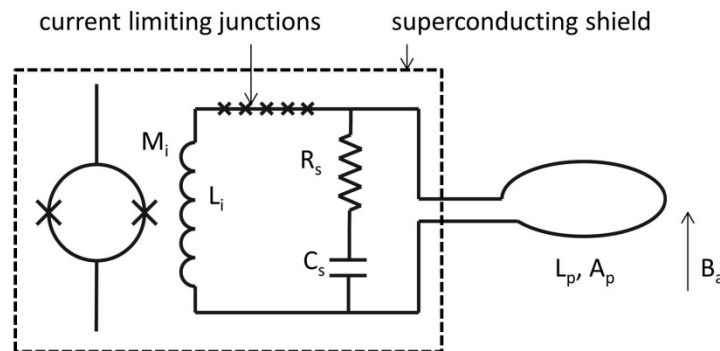
Figure 2.4. Example of a SQUID coupled to a superconducting flux transformer configured as a magnetometer. The RC shunt across the input coil serves as a filter. Typical values: $R_s = 47\Omega$, $C_s = 1$ nF. The current limiting junctions protect the SQUID input coil from large currents produced by large pulsed magnetic fields coupled to the pickup loop.

pulsed magnetic fields. This current-limiting array acts as a self-resetting fuse, remaining superconducting when the current in the input coil is small (< 20 μA), and increasing the resistance of the flux transformer (to ~1 kΩ) when the current is large. The junctions rapidly switch back to the superconducting state once the current in the pickup coil is small.

A flux transformer can take many forms, but the simplest of these is a loop of superconducting wire, such as niobium (Figure 2.4). From the principle of flux quantization within a superconducting loop, a magnetic field B_a applied to the pickup coil causes a supercurrent to flow in the transformer, with magnitude $i = B_a A_p / (L_p + L_i)$. This current couples a flux Φ_s into the SQUID, which is directly related to the applied field B_a by the effective area, A_{eff}:

$$\Phi_s = M_i i = A_p \frac{M_i}{(L_p + L_i)} B_a = A_{eff} B_a \qquad (2.7)$$

$$A_{eff} = A_p \frac{M_i}{(L_p + L_i)} = A_p \frac{\alpha \sqrt{L_i L_{SQ}}}{(L_p + L_i)} \qquad (2.8)$$

For a given pickup loop, the effective area is maximized when $L_i = L_p$. If L_i is a factor of 2 larger or smaller than L_p, however, this decreases A_{eff} by only 6% compared to the optimally matched situation.

In the case of a SQUID operated with minimal magnetic shielding, it is often desirable to configure the pickup coil to reject signals from distant noise sources while maintaining the
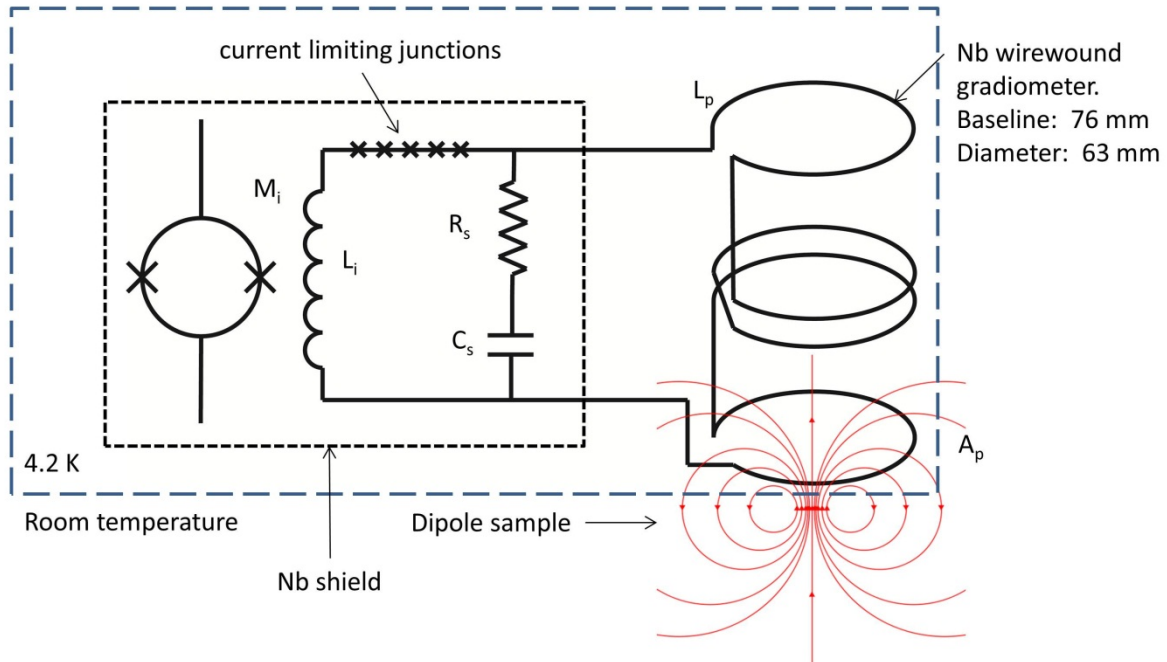
Figure 2.5. SQUID and second-order gradiometer, as configured in the ULF MRI system. $M_i = 20$ nH, $L_i = 1.2$ μH, $L_p = 1.6$ μH, $R_s = 47$ Ω, $C_s = 1$ nF.

sensitivity to nearby signal sources. This is often achieved by the use of a gradiometer, which can take many configurations. An axial gradiometer consists of two coaxial loops wound in opposite senses and separated by a baseline distance b. When a uniform field is applied to the gradiometer, no net flux is coupled to the transformer, and no currents flow in the input coil. The magnetic field from a dipole falls off as $1/r^3$, and therefore when placed near the sensing loop of gradiometer, will couple a net flux into the gradiometer. For further noise rejection, a second-order gradiometer can be used (Figure 2.5), which consists of two counter-wound first-order gradiometers, or even higher order gradiometers. The drawback of using gradiometers is that there is more "dead" inductance in the pickup loop—inductance that is neither sensing the magnetic field from the sample nor coupled to the SQUID. This dead inductance decreases the effective area of the SQUID, decreasing the flux coupled to the SQUID compared to a given uniform field applied to only the sensing loop of the gradiometer. Therefore, there will be an ideal configuration to give the lowest detected noise. This configuration must be experimentally determined, balancing the internal noise of the SQUID with the external noise coupled into the SQUID from the pickup coil.

Chapter 3

Ultra low field MRI

3.1 Polarization

The nucleus of an atom that contains an odd number of protons and/or an odd number of neutrons possesses a magnetic moment $\boldsymbol{\mu}$, associated with its nuclear spin $\boldsymbol{S}$ by $\boldsymbol{\mu} = \gamma\boldsymbol{S}$, where γ, the gyromagnetic ratio, is a known constant unique for each nuclear species. In the experiments presented here, as well as in most medical applications, the atom studied is the hydrogen atom, ^{1}H, which has a gyromagnetic ratio of $\gamma/2\pi \approx 42.6\ Hz/\mu T$.

According to the Zeeman effect, an atom with magnetic moment $\boldsymbol{\mu}$ in the presence of a magnetic field $\boldsymbol{B} = B_0\hat{\boldsymbol{z}}$ has potential energy E given by

$$E = -\boldsymbol{\mu} \cdot \boldsymbol{B} = -\mu_z B_0 = -\gamma S_z B_0. \tag{3.1}$$

From quantum mechanics, S_z is quantized. For a spin-1/2 system such as hydrogen, $S_z = \pm\ \hbar/2$, leading to two energy states (parallel and antiparallel to B_0) separated by

$$\Delta E = \gamma\hbar B_0. \tag{3.2}$$

The ratio of populations parallel to antiparallel $N_\uparrow/N_\downarrow$ is given by the Boltzmann factor,

$$N_\uparrow/N_\downarrow = e^{\Delta E/k_B T}, \tag{3.3}$$

where k_B is Boltzmann's constant and T is the temperature of the spin system. For B_0=1 T at room temperature, the populations are nearly equal, with their ratio approximately equal to 1.000007. The net equilibrium magnetization of the system, M_0, of spin density ρ is given by the net density of spins aligned with B_0 times the magnetic moment $|\mu_z| = \gamma\hbar/2$ of each spin,

$$M_0 = \left(\frac{\gamma\hbar}{2}\right)\rho\frac{N_\uparrow - N_\downarrow}{N_\uparrow + N_\downarrow} = \left(\frac{\gamma\hbar}{2}\right)\rho\frac{e^{\Delta E/k_B T} - 1}{e^{\Delta E/k_B T} + 1} \approx \left(\frac{\gamma\hbar}{2}\right)\frac{\rho\ \Delta E}{2k_B T} = \frac{\rho\gamma^2\hbar^2 B_0}{4k_B T}. \tag{3.4}$$

The amplitude of the NMR signal is proportional to the magnetization, which is proportional to the magnetic field. Ultralow field NMR and MRI, that use a magnetic field in the microtesla range, often use a technique called prepolarization [7]. A transient, strong field (10-300 mT) is applied in the beginning of the experiment to build up magnetization, and is then switched off for the rest of the experiment. For this system, the prepolarization field is applied in a direction perpendicular to the B_0 field. It is turned off adiabatically so that the spins stay aligned with the total field, ending up aligned with the homogeneous B_0 field.

3.2 The Bloch equation of motion

At thermal equilibrium, M and B will be pointed in the same direction. If the direction of M is disturbed from thermal equilibrium, M will exhibit Larmor precession at a frequency $\omega = \gamma B$ clockwise around B, where γ is the gyromagnetic ratio and B is the magnitude of the field. The dynamics of M including relaxation effects are given by the phenomenological Bloch equation

$$\frac{d\boldsymbol{M}}{dt} = \boldsymbol{M} \times \gamma \boldsymbol{B} - \frac{M_x \hat{\boldsymbol{x}} + M_y \hat{\boldsymbol{y}}}{T_2} - \frac{(M_z - M_0)\hat{\boldsymbol{z}}}{T_1}, \tag{3.5}$$

where M_x, M_y, and M_z are the components of M, M_0 is the equilibrium magnetization due to the external field (Equation 3.4), and T_1 and T_2 are the longitudinal and transverse relaxation times, respectively. The first term of the Bloch equation describes precession, the second term describes the decrease in net magnetization from the dephasing of the spins in the transverse plane, and the third term describes the relaxation of the longitudinal magnetization to equilibrium. The relaxation terms are valid for a field pointing along the z axis.

The transverse relaxation interactions include the collective dephasing effect, where no energy is lost, as well as the same spin-lattice couplings giving rise to T_1 effects; thus, $T_2 < T_1$. In practice, there is an additional dephasing of the magnetization introduced by external field inhomogeneities that can sometimes be characterized by a separate decay time T_2'. The total relaxation rate is then $1/T_2^* = 1/T_2 + 1/T_2'$, where T_2 is the intrinsic dephasing time. The decrease in transverse magnetization due to $1/T_2'$ is 'recoverable' with an additional pulse to recover their initial phase relationship, but the intrinsic T_2 dephasing is related to local, random, time-dependent field variations and is not recoverable.

Solving Equation 3.5 for a constant field $\boldsymbol{B} = B_0 \hat{\boldsymbol{z}}$, we see the transverse components exhibit precession at frequency $\omega_0 = \gamma B_0$ with decaying magnitude, and the longitudinal component relax to equilibrium exponentially:

$$M_x(t) = e^{-t/T_2} \left[M_x(0) \cos \omega_0 t + M_y(0) \sin \omega_0 t \right], \tag{3.6}$$

$$M_y(t) = e^{-t/T_2} \left[M_y(0) \cos \omega_0 t - M_x(0) \sin \omega_0 t \right], \tag{3.7}$$

$$\text{and } M_z(t) = M_0 - e^{-t/T_1} \left[M_0 - M_z(0) \right]. \tag{3.8}$$

A convenient way to represent the transverse magnetization is

$$M_\perp(t) = M_x(t) + iM_y(t) = M_\perp(0)e^{-t/T_2}e^{-i\omega_0 t}. \tag{3.9}$$

In the case of prepolarized NMR, the magnetization is allowed to come to equilibrium in a high field. This field is then switched off and the magnetization is left in an elevated state, and relaxes toward zero. It has long been established that T_1 varies with applied field, and the difference in T_1 between some tissues is enhanced at fields of ~100 µT compared to more conventional fields of ~1 T [5]. We take advantage of this in this ULF MRI system.

3.3 Detection

In NMR and MRI experiments, the detection coil is oriented perpendicularly to B_0 (Figure 3.1) and is only sensitive to the dipoles which are oriented perpendicularly to B_0, and therefore precessing. Additionally, in typical NMR experiments, the detection coil is a loop of copper wire in a resonant circuit tuned to the precession frequency. This type of detector has a voltage output proportional to the rate of change of flux in the detection coil. At microtesla fields, and therefore kilohertz precession frequencies, the signal-to-noise ratio of this type of detector becomes very small [14]. A detector such as the SQUID combined with an untuned superconducting input coil, such as that described in the previous chapter, has a voltage output proportional to the flux in the detection coil. The signal-to-noise ratio is adequate for MR images, and the frequency independent nature of the detector allows the precession frequency to be arbitrarily low, allowing SQUID-detected ULF MRI to take full advantage of any increased T_1 contrast at low fields.

3.4 Excitation

Additional pulsed magnetic fields are needed to excite the magnetization away from thermal equilibrium and into the transverse plane. The magnetization precesses around the net field, so adding a short-lived pulse in a direction perpendicular to B_0 will cause the magnetization to tip away from the z-axis and begin precessing. As shown in detail in [1], a field in the y direction $\boldsymbol{B_1}(t) = B_1 \sin \omega_0 t \, \hat{\boldsymbol{y}}$ causes the magnetization to rotate away from the z axis so that it forms an angle $\theta = \gamma B_1 t/2$. The most common applications of this excitation pulse in the experiments described in this dissertation are the 90° and 180° pulses. A 90° pulse is often used to tip the magnetization from the z-axis into the transverse plane. A 180° pulse is often used to invert the
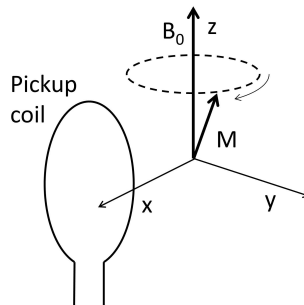
Figure 3.1. Clockwise precession of magnetic moment *M* around B_0, and orientation of pickup coil perpendicular to B_0.
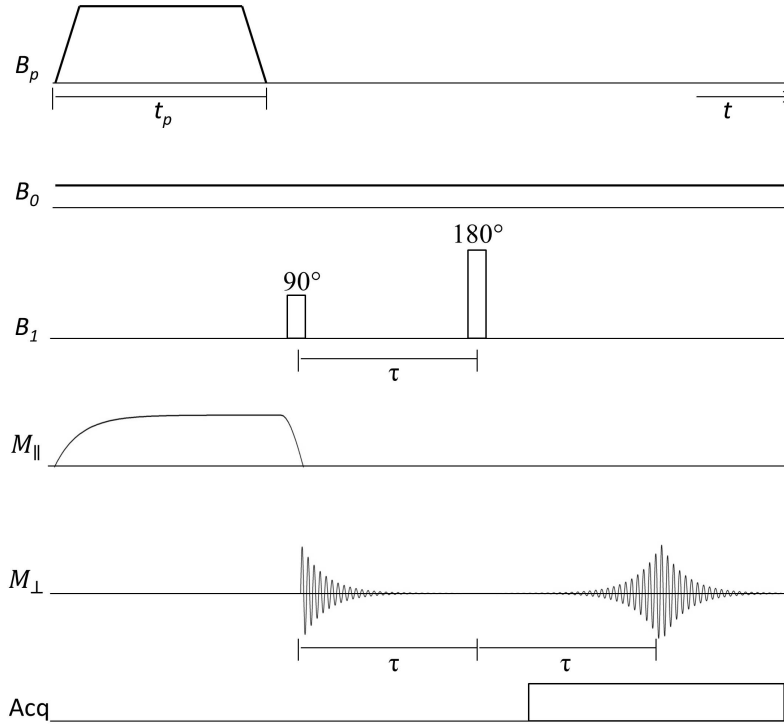
Figure 3.2.   Pulse sequence for prepolarized NMR.   The B_p pulse is applied for time t_p, during which the magnetization parallel to the field increases to equilibrium in that field.   After the B_p is turned off, the B_0 field remains.   The B_1 field is applied.   The figure shows the amplitude of the envelopes for the resonant excitation at frequency ω_0.   After the 90° pulse, all magnetization that was parallel to the magnetic field has been excited to be perpendicular, and begins precessing and dephasing.   After a time τ, a 180° pulse is applied which rephases the spins, and an echo occurs after another time τ.   The data is acquired during the echo.

phases of magnetization which are already precessing in the transverse plane.   This type of pulse is called a Hahn spin echo [15], which has the effect of refocusing the phase of an ensemble of precessing spins that have been dephased because of different precession frequencies due to magnetic field inhomogeneities, such as those caused by magnetic field gradients.

For the prepolarized ULF MRI system described in this dissertation, a typical magnetic field pulse sequence is shown in Figure 3.2.   A large prepolarizing field B_p (~100 mT) is applied for a time t_p (~500 ms) comparable to the T_1 of the sample in that field.   During this time, the longitudinal magnetization $M_\parallel$ builds up.   Subsequently, B_p is turned off and the excitation field B_1 is applied to rotate the spins θ=90° into the transverse plane where they begin precessing, and therefore dephasing ($M_\perp$).   After a time τ (~10 ms) that is small compared to the T_2 time of the material, B_1 is applied again to rotate the spins θ=180°.   The measurement begins after this field is turned off, and a time τ after the 180° pulse, the spins rephase in an echo.

3.5   Gradients, k-space and imaging

The frequency in Equation 3.9 can depend on position and on time with the application of time dependent magnetic field gradients, $\boldsymbol{G} \equiv \frac{\partial B_z}{\partial x}\widehat{\boldsymbol{x}} + \frac{\partial B_z}{\partial y}\widehat{\boldsymbol{y}} + \frac{\partial B_z}{\partial z}\widehat{\boldsymbol{z}}$.   Each component can be

controlled separately. We assume the gradients are linear and unidirectional, changing only the magnitude of the z component of the magnetic field. A discussion of the effects of when this assumption is not valid and the concomitant perpendicular components of the gradients become an issue can be found in [16,17]. The spatially and time dependent frequency of precession is given by

$$\omega(\boldsymbol{r},t) = \gamma B(\boldsymbol{r},t) = \gamma[B_0 + \boldsymbol{G}(t)\cdot\boldsymbol{r}]. \tag{3.10}$$

For an inhomogeneous sample, the flux in the pickup coil $\Phi_r(r,t)$ from each point $\boldsymbol{r}$ is an oscillating signal proportional to its magnetization $m(\boldsymbol{r})$, with phase given by Equation 3.12:

$$\Phi_r(\boldsymbol{r},t) \propto \mathrm{Re}\big[m(\boldsymbol{r})e^{-i\phi(r,t)}\big] \tag{3.11}$$

$$\phi(\boldsymbol{r},t) = \int_0^t \omega(\boldsymbol{r},t')\,dt' = \omega_0 t + \gamma\left[\int_0^t \boldsymbol{G}(t')\,dt'\right]\cdot\boldsymbol{r}. \tag{3.12}$$

Since we detect the flux from the entire sample at the same time, to get the total flux in the pickup loop $\Phi_p(t)$, we integrate $\Phi_r(r,t)$ over the volume of the sample:

$$\Phi_p(t) = \mathrm{Re}\left[\int_V m(\boldsymbol{r})e^{-i\phi(r,t)}d^3r\right] \tag{3.13}$$

$$\Phi_p(t) = \mathrm{Re}\left[\int_V m(\boldsymbol{r})e^{-i\omega_0 t}exp\left(-i\gamma\left[\int_0^t \boldsymbol{G}(t')dt'\right]\cdot\boldsymbol{r}\right)d^3r\right]. \tag{3.14}$$

The detected voltage from our SQUID detection system is directly proportional to the flux in the pickup coil $\Phi_p(t)$. Demodulating the detected voltage by the spatially independent factor $e^{-i\omega_0 t}$, gives a signal $s(t)$:

$$s(t) = \int_V m(\boldsymbol{r})exp\left(-i\gamma\left[\int_0^t \boldsymbol{G}(t')dt'\right]\cdot\boldsymbol{r}\right)d^3r. \tag{3.15}$$

This expression has the form of a spatial Fourier transform, and is easily seen if we identify terms in the following way:

$$s[\boldsymbol{k}(t)] = \int_V m(\boldsymbol{r})exp(-i2\pi\boldsymbol{k}\cdot\boldsymbol{r})d^3r \tag{3.16}$$

$$\text{and } \boldsymbol{k}(t) = \frac{\gamma}{2\pi}\left[\int_0^t \boldsymbol{G}(t')dt'\right]. \tag{3.17}$$

This expression indicates that the inherent signal acquisition in MRI is in reciprocal space (k-space), and that the applied gradient strength is the velocity at which you move through reciprocal space. From the definition of $\boldsymbol{k}$ in Equation 3.17, the effect of a 180° pulse is to invert

the phase, transforming $k \rightarrow -k$.   From the properties of the Fourier transform, sufficient coverage of k-space is required to successfully reconstruct the spatial image.   The field of view in a direction x_i is given by the inverse of the sampling rate in k-space in that direction, $FOV_i = 1/\Delta k_i$ and the resolution is the field of view in direction x_i divided by the number of samples in that direction, $\Delta x_i = FOV_i/N_{s,i}$.

There are many different ways to apply the gradients to cover k-space, but the method that is used in this the data acquired in this dissertation is the simplest.   For a two dimensional image, the pulse sequence (Figure 3.3A) is similar to the NMR sequence except for the addition of two gradients.   One, called the *frequency encoding gradient,* is usually turned on at a certain amplitude, and left on during the acquisition.   The second, called the *phase encoding gradient*, is turned on during the time between the two excitation pulses, and is off during the acquisition. Figure 3.3B shows the method of covering k-space; it assumes that the frequency encoding gradient is in the z direction, and the phase encoding direction is in the y direction.

To translate this to a three-dimensional image, a third gradient, used as a second phase encoding gradient, is incorporated to acquire the three-dimensional k-space.
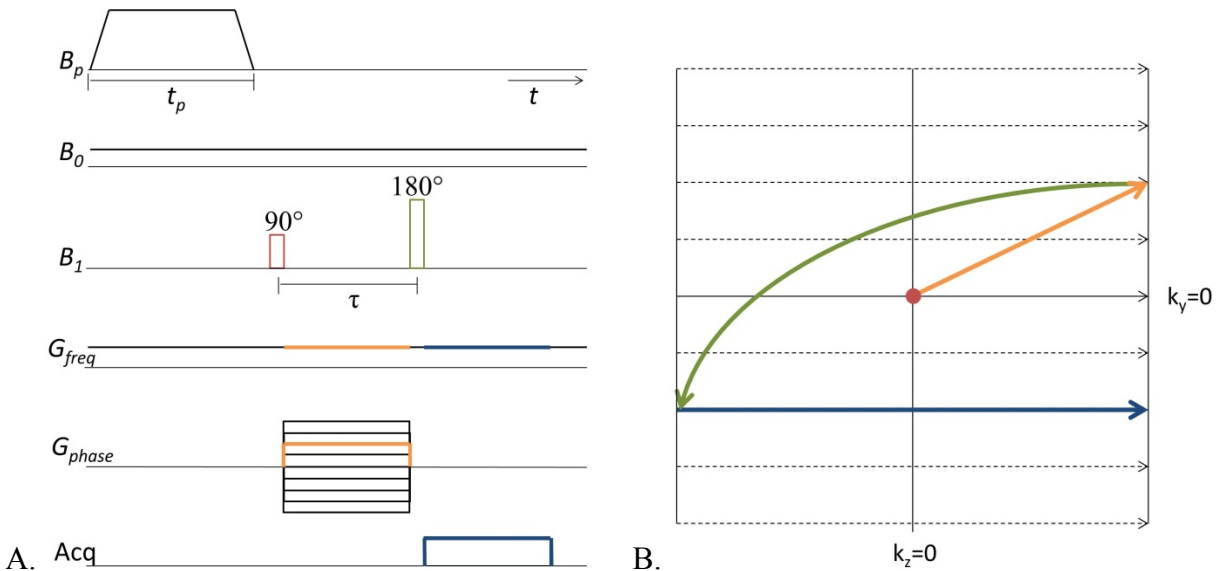
Figure 3.3. 2D MRI pulse sequence and k-space coverage. A: Pulse sequence for 2D imaging. The frequency encoding gradient is left on constantly, while the phase encoding gradient is pulsed between the 90° and 180° pulses. The phase encoding gradient shows many different lines, indicating that the sequence is repeated a number of times, each time choosing a single amplitude. B: The evolution of the spins in k-space for the phase encoding gradient shown by the orange line in A. This figure is color coded to correspond to part A, with the frequency encoding gradient in the z direction and the phase encoding gradient in the y direction. The 90° excitation pulse excites the spins at k=0. During the time between the 90° and 180° pulses, both the z and y gradients are on at a constant value (orange lines in A), so the spins travel at constant velocity along the orange arrow in B. The 180° pulse (green) sends $k \rightarrow -k$. Subsequently, only the z gradient is on, so the spins stay at constant k_y and travel along k_z. The signal is acquired during the time the spins are traveling along the blue arrow. This sequence is repeated for different values of G_{phase}, and therefore covers many lines of k-space.

3.6   Excitation in a non-uniform field

As can be seen in Figure 3.3A, in our pulse sequence we leave the frequency encoding gradient on throughout the entire measurement. In this case, the precession frequency varies across the sample, so it is impossible to excite all of the spins at their resonant frequency. The frequency content of a given excitation pulse is found by taking its Fourier transform (Figure 3.4). A pulse with a rectangular envelope at frequency f_0 lasting for a total time τ_{exc} has a frequency selection profile of sinc[π (f-f_0) τ_{exc}]. As an example (Figure 3.4A), a 6400 Hz pulse containing 8 cycles, for total pulse length of 1.25 ms has a frequency selection profile of a sinc function, with zeros at 5600 Hz and 7200 Hz. Conversely, if the B_1 pulse shape has a sinc envelope of sinc(t/Δt), the frequency selection profile is a rectangular function of width 1/($\pi\Delta$t) centered on the pulse frequency. In Figure 3.4B, the 6400 Hz B_1 pulse is modulated in time by the 4 lobe sinc envelope sinc(t/0.0002 s) and gives a frequency profile of width 1600 Hz centered on 6400 Hz.

This technique can be used to excite only certain portions of the sample, called slice selection. To use this technique, one would apply a (fairly strong) gradient in conjunction with an excitation pulse with a properly designed sinc envelope. Only the spins which are precessing at the frequencies "selected" by the B_1 pulse will be excited. This technique allows a 2D image to be acquired from a slice of a 3D object, dramatically decreasing imaging time.

In our case, this analysis was done to ensure that we were exciting the entire sample adequately in the presence of a gradient. Since the bandwidth of our measurements was not usually greater than 400 Hz, Figure 3.4A shows that the excitation pulse will affect the spins in this bandwidth roughly equally despite the applied gradient. We therefore concluded it was adequate to leave this gradient on constantly, even during the B_1 pulses.
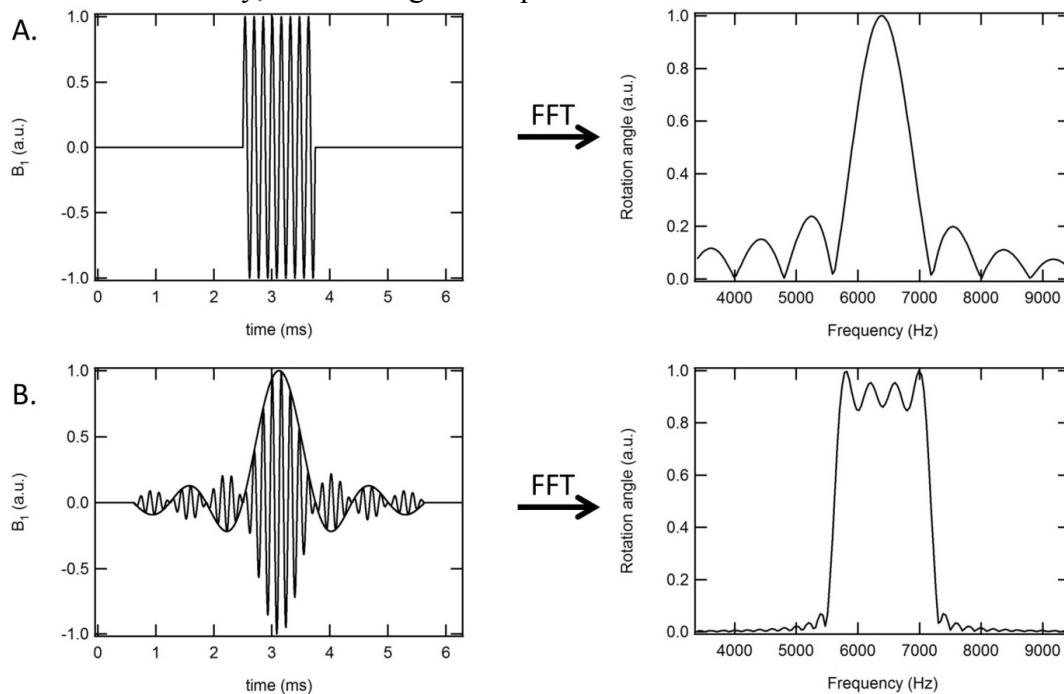
Figure 3.4. Relationship between B_1 time series and frequency excitation profile. A: Rectangular envelope in time yields a sinc frequency profile. B: Sinc envelope in time yields a rectangular frequency profile.

3.7   Magnetization preparation: T_1 contrast and inversion recovery

The brightness of a specific area in an MRI depends on the magnitude of the precessing magnetization. As seen from sections 3.1 and 3.2, the amplitude of the precessing magnetization depends on the spin density, T_1 and T_2. For most applications presented in this dissertation, we assume a uniform spin density over the whole sample. We measure as quickly as possible after excitation to minimize the effect of T_2 weighting. The mechanism of contrast we exploit the most in these measurements is T_1 contrast.

In most cases, the acquisition of an MR image or NMR spectrum is as described in previous sections of this chapter. The main difference between the different techniques described in this section is in the magnetization preparation stage. The brightness in an MR image of the different materials in the sample are affected by this magnetization preparation stage, which I will show in the figures as the part of the sequence before the 90° B_1 pulse designed to excite the spins as in a typical sequences like Figure 3.2 and Figure 3.3.

A pulse sequence for prepolarized T_1 weighting is shown in Figure 3.5 [6,18]. After an initial prepolarizing pulse, the magnetization of the two species (red and blue) are at an elevated state compared to thermal equilibrium in the B_0 field. During the low field evolution time, t_{ev}, the magnetization of each species decays back to the equilibrium in the B_0 field (~1% of the equilibrium at B_p) with their different time constants T_1. After t_{ev}, the two magnetizations have different amplitudes, and a 90° B_1 pulse is applied followed by a standard NMR or MRI sequence. In Figure 3.5, the red species will appear brighter in the image compared to the blue species.
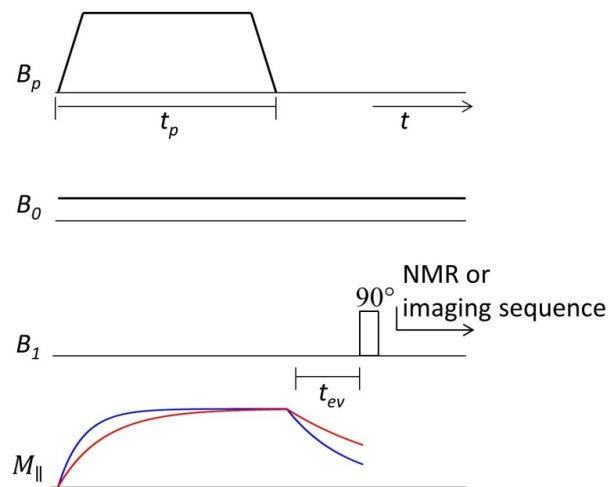
Figure 3.5. T_1-weighted pulse sequence.   The red and blue lines in the magnetization plot represent the magnetizations of different species in the sample which have different T_1 relaxation times. We prepolarize such that the magnetization of both species comes to equilibrium in the prepolarization field. After B_p is switched off, there is a low field evolution time t_{ev} in which the spins are still aligned parallel to B_o and are not precessing. During this delay period, the elevated magnetization decays back to equilibrium (essentially 0 in the B_0 field) with time constants T_1. If the 2 species have different T_1 times, the amplitude of their magnetizations will diverge during this time. Beginning an image at a time such as this time will show the red species to be brighter in the image than the blue species.

Instead of looking at a single image after a time t_{ev}, it is possible to measure the T_1 of each pixel in an image. This is done by acquiring exactly the same image after the 90° pulse for many different times t_{ev}. We plot the amplitude of each pixel versus the different evolution times, and fit this to $\exp(-t_{ev}/T_1)$ to find the T_1 of that pixel.

Another method of magnetization preparation is called inversion recovery (Figure 3.6). This preparation stage begins in the same way as the T_1-weighted pulse sequence. At the end of the low field evolution time, a 180° pulse is applied.   This inverts the magnetization to be anti-aligned with the B_0 field. Next, a second polarizing pulse is applied for a time t_{p2}, which can be chosen such that the magnetization of one of the species crosses zero. At this point, the B_p pulse is turned off and a 90° B_1 pulse is applied to begin the imaging sequence. With the timing shown in Figure 3.6, there would be zero signal from the red species, and a nonzero signal from the blue species.
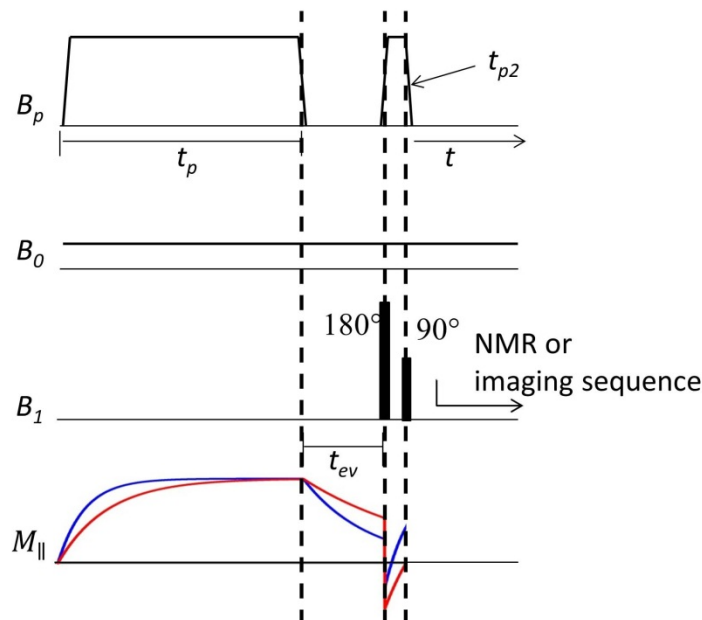
Figure 3.6. Inversion recovery pulse sequence. The red and blue lines in the magnetization plot represent the magnetizations of different species with different T_1 times. The preparation is the same as in Figure 3.5 until the B_1 pulse. Here, at the end of the low field evolution time, a 180° pulse is applied. This inverts the spins to be anti-aligned with the B_0 field. A second polarizing pulse is applied for a time t_{p2}, which is normally chosen such that magnetization of one of the species is crossing zero. At this point, the B_p pulse is turned off and a 90° B_1 pulse is applied to begin the imaging sequence. As shown here, there would be zero signal from the red species, while the blue species would have a nonzero signal.

Chapter 4

System Overview

Our ULF MRI system has been continuously improved upon since its original construction in 2001. A description of the original system can be found in [19] and [2]. This chapter describes the system with which I worked the most, commonly referred to amongst ourselves as the "second generation system". In Chapter 5, I will describe the changes we have subsequently made to the system detailed in this chapter for the purpose of integrating a larger prepolarization coil. In summary, these changes include: a new prepolarization coil, a third generation aluminum shield, an additional coil to aid with the adiabatic turnoff of the prepolarization field, and a method of reducing the effect of the B_p pulse on coils that have a large mutual inductance to it, along with the requisite changes in pulse sequence. A schematic of the "second generation" coil system and a photograph of the system are shown in Figure 4.1.

In this chapter, Section 4.1 gives a broad overview of the system. Section 4.2 describes the liquid helium dewar, the gradiometer input circuit, and SQUID readout. Section 4.3 describes

A.

B_x, B_y compensation coils
low noise cryostat
gradiometer
dB_z/dz gradient coil
dB_z/dx gradient coil
B_0 coil (measurement field)
polarization coil and sample
B_1 coil (excitation field)
(dB_z/dy gradient coils not shown for clarity)

B.
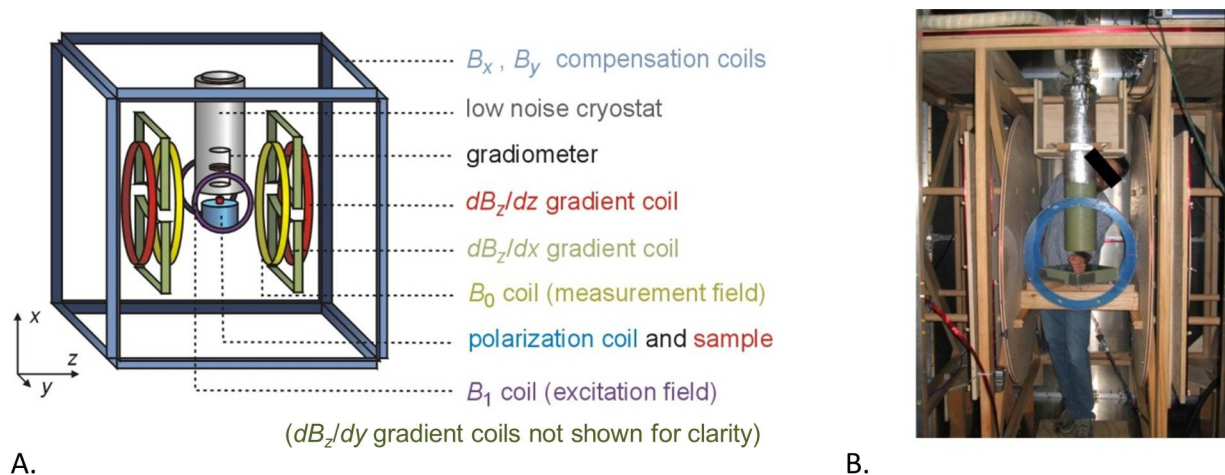
Figure 4.1. ULF MRI system. A: Schematic of the SQUID MRI system showing magnetic field and gradient coils and the liquid helium dewar; for clarity G_y coils are not shown. B: Photograph of the system in the configuration to image human extremities. The sample is at the center of the blue coils, in this case, a forearm.

the magnetic field coils and operating circuits, and typical operating conditions. Section 4.4 describes the aluminum shielding which encloses the entire apparatus.

4.1 Overview

The sample, detector and magnetic field coils are housed inside an aluminum shielded room that screens from radiofrequencies down to kilohertz frequencies. All of the coils are connected to the inside wall of the shielded room with twisted pair to grounded BNC coaxial connectors. The field coils are either static throughout the imaging sequence, or are pulsed. The static fields are powered with floating DC current controlled power supplies and filtered at the wall of the shielded room. The pulsed fields are powered with voltage amplifiers during the encoding, and the lines are opened with relays at the wall of the shielded room during signal acquisition. A computer interfaces with a Tecmag Orion^{TM}, a commercial MRI pulse shaper and ADC. The control pulses for the voltage amplifiers are output from the Tecmag, as well as TTL pulses for controlling relays and other aspects of the system. The magnetic fields from the coils affect the magnetization of the sample. The magnetic field from the sample is in turn detected by the gradiometer and SQUID. These superconducting components are at 4.2 K and are housed inside a custom-built low noise dewar. The flux-locked loop electronics for the SQUID are battery powered and located inside the shielded room. The voltage output from the SQUID electronics exits the room through a grounded BNC coaxial connector, passes through a bandpass filter, and is read in by the Tecmag. Post processing is done in IGOR Pro.
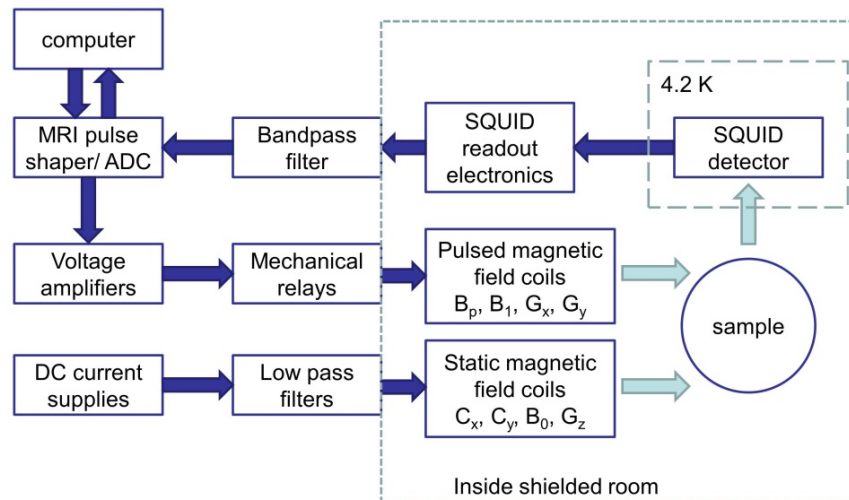
Figure 4.2. Block diagram of system. Dark blue arrows indicate wired connections. Light blue arrows indicate coupling of magnetic fields. There may also be parasitic coupling of noise from magnetic field coils to the SQUID detector. This noise has been reduced by the filters and relays.
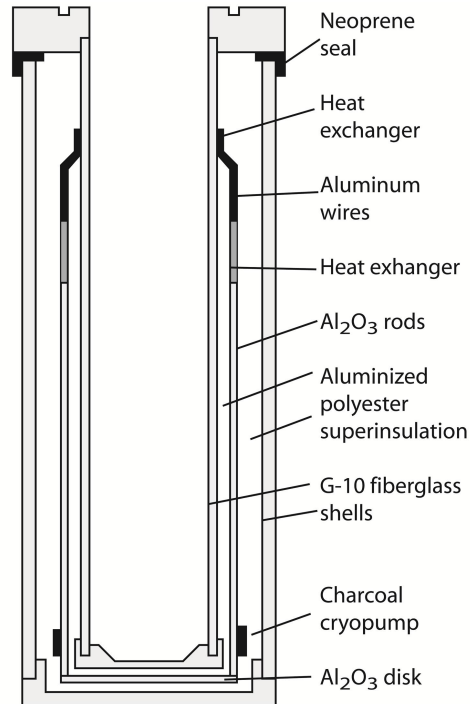
Figure 4.3.   A schematic of the fiberglass liquid helium cryostat, with ceramic thermal shield and aluminized polyester cloth superinsulation.

4.2   Dewar, Gradiometer and SQUID readout

The superconducting components of the probe (the SQUID and gradiometer) are immersed in a bath of liquid helium inside a custom-built low-noise fiberglass dewar in the design of Seton *et al.* [20], while the sample and magnetic field coils are situated outside the dewar, as shown in Figure 4.1.   Like all helium dewars, this dewar consists of an inner vessel containing liquid helium separated from the outer vessel by vacuum. The body of this dewar is made of cylinders of G-10 fiberglass purchased from Langtec Ltd., UK. To reduce the thermal radiation load on the inner vessel, we have installed a thermal shield in the vacuum space that is anchored to the neck of the inner vessel, along with many layers of superinsulation. The industry standard for these components is to use aluminized mylar superinsulation and a copper mesh thermal shield. However, Nyquist noise currents in these components create a magnetic field noise of about 10 fT Hz$^{-1/2}$ [2], a value substantially larger than the intrinsic noise of our detector (< 1 fT Hz$^{-1/2}$). Following Seton's method to circumvent this problem, the metallic components of the shield are greatly reduced, and the mylar superinsulation is replaced with polyester superinsulation kindly provided by Hugh Seton. The coarse weave of the polyester breaks up the deposited aluminum into small   disconnected   islands,   decreasing   the   contribution   of   Nyquist   noise   from   the superinsulation. Our thermal shield is constructed of 1-mm diameter alumina rods placed 1 mm apart, and bonded with epoxy to a thin fiberglass tube for support. The bottom of the shield is made from a 5-mm thick disk purchased from Coorstek, Inc., USA and machined to 2 mm thick by the Lawrence Berkeley National Laboratory ceramics shop. The shield is connected to the neck of the dewar via short lengths of 1-mm diameter aluminum rods which have been bonded
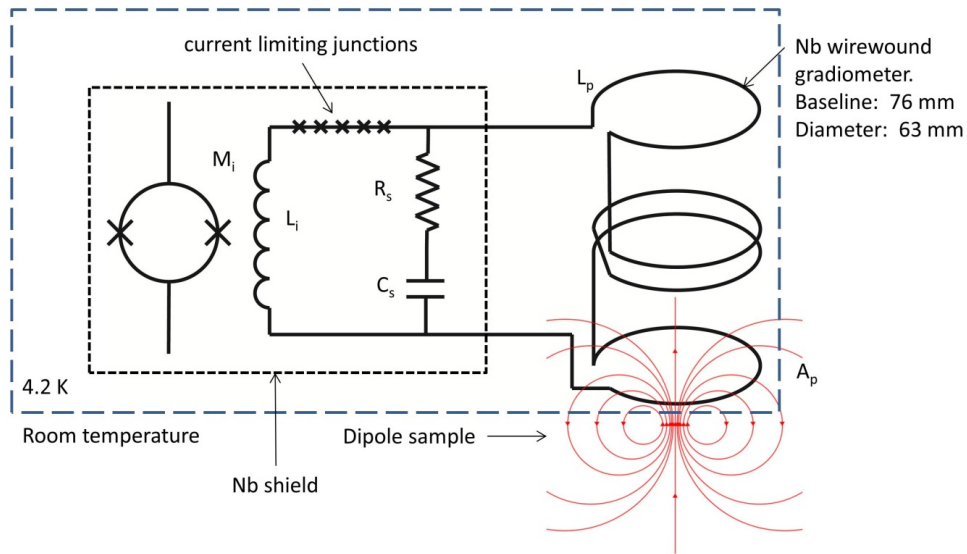
Figure 4.4.   Schematic of magnetic field coupling from sample (dipole) to second-order gradiometer, and subsequently to SQUID.

with Stycast to both the shield and the neck. Seton *et al.* estimates the noise contribution from the dewar the built to be 0.035 fT Hz$^{-1/2}$ [20]. The distance between the bottom of the inner vessel and the sample space on the outside of the dewar is 25 mm when cooled. A schematic of the dewar is pictured in Figure 4.3.

The magnetic field from the sample is inductively coupled to the SQUID via a superconducting second-order axial gradiometer, as shown in Figure 4.4. The center 2 loops are wound in the opposite orientation with respect to the top and bottom loops.

The gradiometer is hand-wound on a machined paper phenolic tube, using 75-µm diameter niobium wire with formvar insulation. The loops are 63.5 mm in diameter. The distance between the end loop and the next closest loop is 76 mm for each side. The distance between the center two loops is 2.5 mm. The inductance of the gradiometer is 1.6 µH, and the mutual inductance between the gradiometer and a test coil wound around the outside of the dewar, 25 mm from the bottom, is 10 nH. For calibration of the effective area of the SQUID (Chapter 2), a current is passed through the test coil, and the flux in the SQUID is measured. The gradiometer has a measured balance against uniform fields of ~1/760 in the axial direction.

The gradiometer wire ends are stripped and pressed against niobium pads on the SQUID chip holder (Figure 4.5) with brass screws. Niobium wire bonds are overlapped with the gradiometer leads under the brass screws, and connect to the input circuit of the SQUID. The input circuit on one side is interrupted by a 20 Josephson junction series array current limiter, with critical current of 30 µA. This current limiter protects the circuit from large magnetic field pulses from, for example, the prepolarization coil. On the back side of the board, an RC shunt is soldered across the nuts. This shunt consists of a 47 Ω resistor in series with a 1 nF capacitor, and has a roll-off frequency of $1/(2\pi RC) = 3.4$ MHz.
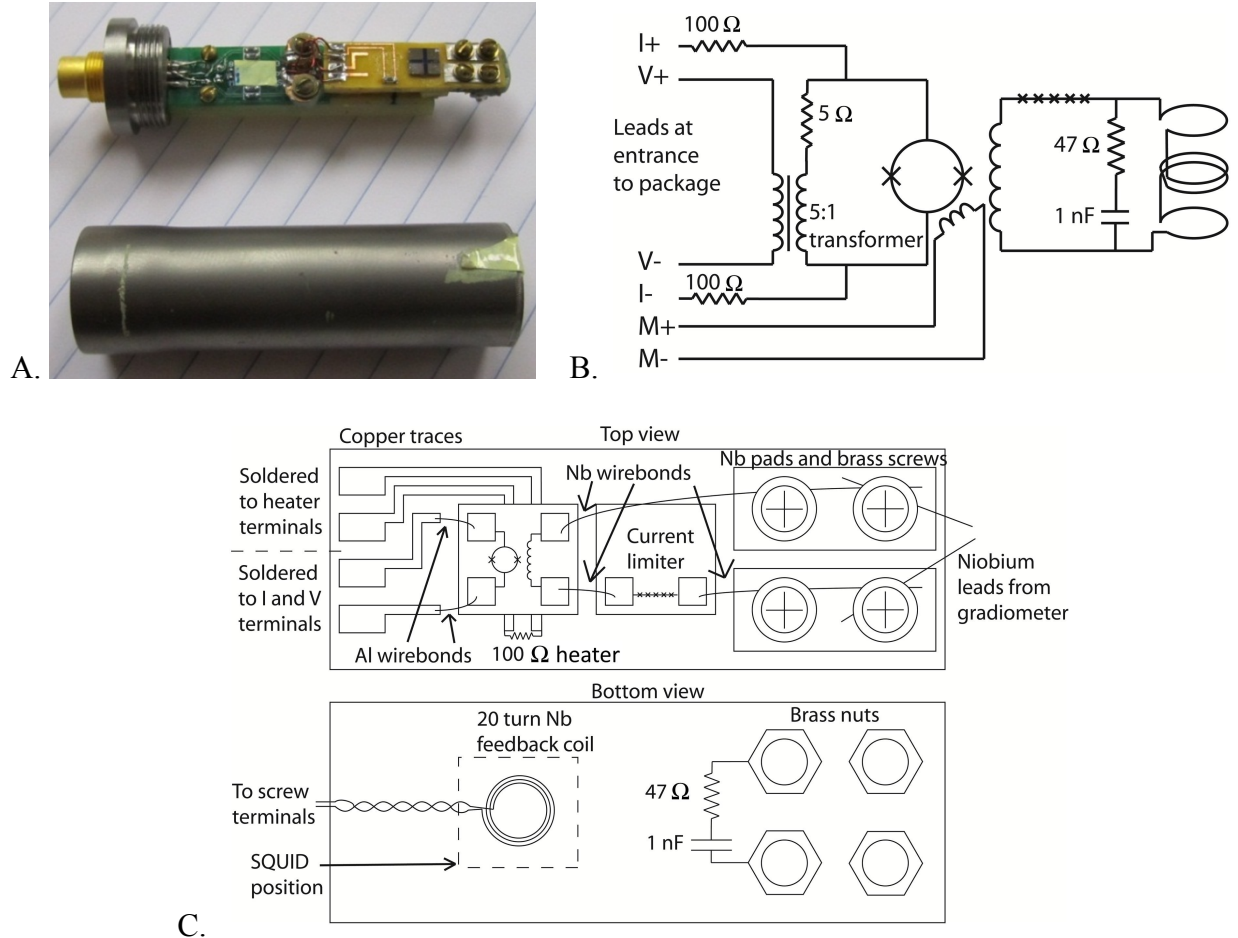
Figure 4.5. SQUID detection circuit. A: Photograph of the SQUID board and niobium shield. The SQUID chip is missing in this photo, and would usually be placed just to the left of the current limiter chip. B: Schematic of detection circuit beginning at entrance of niobium shield. C: Detailed schematic of yellow SQUID chip holder.

The various SQUIDs used all had 60-turn input coils and were provided by ez-SQUID (Michael Mueck). Because of the high inductance of our pickup loop (1.6 µH), we required a high input coil inductance (in this case, 1.2 µH), giving a mutual inductance to the SQUID of nominally 20 nH. The SQUID is bonded with aluminum wire bonds to pads which are soldered to the current and voltage leads of the SQUID package, part number LS2076 purchased from Star Cryoelectronics. A schematic of the circuit is shown in Figure 4.5B and C. The voltage leads have a 20:100 turn transformer on a molypermalloy core (part # A-358083-8 from Group Arnold) with inductance factor 83 mH/1000 turns (located on the backside of the green board shown in Figure 4.5A). In the primary of the transformer there is a 5 Ω resistor (modification from the 1 Ω resistor that is standard on the board) to prevent the SQUID bias current from being completely shunted through the primary of the transformer. The current leads have 100 Ω resistors in each line inside the package. Beneath the SQUID, there is a 2-mm diameter, 20 turn feedback coil wound out of 75-µm diameter niobium wire. This coil has an estimated coupling to the SQUID of 0.5 nH. This entire setup is then enclosed in the niobium shield shown in the bottom of Figure 4.5A.
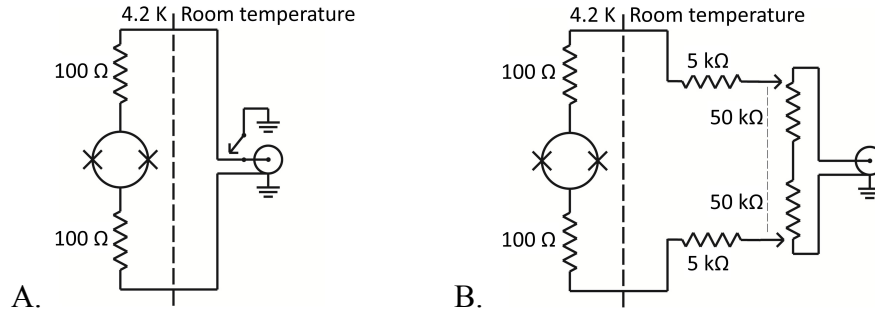
Figure 4.6. Protection for SQUID leads. A. Original protection scheme inside the probe top for the current leads. This serves as protection when connecting and disconnecting wires. When protected, both sides of the circuit are shorted to ground. B. New protection scheme for bias current leads. When protected, the wipers for the double ganged pot are towards the middle, thus there is 10 kΩ across the SQUID, and 50 kΩ to any exposed connectors.

The package has a 10-pin LEMO connector which connects to the probe. The probe is wired with twisted pairs of copper wire, each pair inside its own grounded CuNi shield.   Inside the breakout box at the top of the probe, each line has protection against electrostatic discharge. The flux in the SQUID is read out with home-built flux-locked loop electronics with a flux modulation frequency of 2 MHz. The measured effective area of the SQUID is 22.3 mm^2, and the lowest noise achieved with all MRI coils in operation is 0.7 fT Hz$^{-1/2}$.

At one point, for a period of months, each SQUID we installed in the system stopped working after days or weeks in operation because one of the junctions became a superconducting short. This was likely due to electrostatic discharge destroying the insulating barrier.   After the following changes in handling protocol, this problem has been greatly reduced.

•   When handling the SQUID or probe, one should be grounded.
•   When the probe is cold, always keep the probe grounded.
•   Before turning the SQUID readout electronics on or off, be sure that the outputs for the bias current and the flux modulation amplitudes are turned all the way down. This minimizes possibly damaging transient voltage spikes.
•   We installed a continuous protection circuit for the bias current leads using potentiometers (Figure 4.6B) instead of a switch (Figure 4.6A). The voltage and modulation leads still have the switched protection shown in the room temperature section of Figure 4.6A.

4.3   Magnetic field coils
A schematic of the coil system is shown in Figure 4.1. All coils except the prepolarization coil are grounded at the wall of the shielded room

4.3.1   Static coils
The static coils are all powered with current controlled power supplies, and have filters in line.

Earth field cancellation coils, C_x and C_y: Because our imaging field (~100 μT) is not much larger than the earth's magnetic field (50 μT), we must cancel the earth's magnetic field in the two perpendicular directions in order to have control over the fields in our system.   The

amplitude of current flowing through each of the coils is that which best cancels the magnetic field. This is measured with a fluxgate magnetometer that has been zeroed in a mu-metal shield. We tune the current in the C_x, C_y, and B_0 coils to zero the field in the 3 directions. For the system in place now, this occurs near 0.45 A in each coil cancellation coil. Subsequently, the current in the B_0 coil is changed in preparation for NMR.

Measurement field (B_0) coil: This coil was originally of a four-coil biplanar design, with the larger, 1.37 m diameter coil having 20 turns, and the smaller 0.36 m diameter coils having 10 turns. The coils are separated by 0.6 m. The ratio of current in the large coils to the small coils was designed to be 20. However, we never implemented the smaller coils and have been operating with only the large coils.

We wound two sets of this biplanar B_0 on top of each other, with plans to use one coil as the measurement field, and the second coil to increase or decrease the measurement field strength during portions of the imaging sequence (field-cycling). Using an identical set of coils for field-cycling would be advantageous because the field profile would not change with applied cycling field amplitude, as it might when the inhomogeneity of the two coils is very different.

Coil name	Coil description (wound on wood frame unless noted)	Turns, wire gauge Inductance Resistance	Typical field/gradient Typical current
Earth field cancellation coils, C_x ($\hat{\mathbf{x}}$), C_y ($\hat{\mathbf{y}}$)	Square coils on opposite sides of 1.8 m cube	100, 18 AWG 110 mH 31 Ω	23 μT 0.45 A
Measurement field B_0 ($\hat{\mathbf{z}}$)	Circular coils 1.37 m diameter spaced 0.6 m apart	20, 18 AWG 5.9 mH 3.8 Ω	132 μT 4.2 A
Gradient G_z (dB_z/dz)	Maxwell pair, diameter 1.13 m	26, 18 AWG 6.8 mH 4.0 Ω	100 μT/m 1.5 A
Excitation field B_1 usually oriented in $\hat{\mathbf{y}}$	Helmholtz pair, diameter 0.56 m Acrylic frame	15, 22 AWG ~1 mH 5 Ω	5 μT 100 mA
Planar gradient coil G_x (dB_z/dx)	Biplanar coil, 0.9 m wide, 1.28 m high, 0.76 m separation	20, 17 AWG ~4.5 mH 3.8 Ω	700 μT/m (max) 9 A
Planar gradient coil G_y (dB_z/dy)	Biplanar coil, 1.45 m wide, 1.02 m high, 0.86 m separation	20, 17 AWG ~5 mH 4.3 Ω	700 μT/m (max) 11.6 A
Polarizing coil B_p ($\hat{\mathbf{x}}$)	ID 32 mm, OD 230 mm, height 50 mm	650, 30-28 AWG Litz 2 Ω	60 mT at surface 20 A
Eddy current cancellation coil, in $\hat{\mathbf{x}}$	Square 1.8-m coil wound horizontally	20, 18 AWG 3.1 Ω	13 μT 1 A

Table 4.1. Properties of magnetic field coils used in the MRI system

However, due to the large mutual inductance of the field cycling coil with the B_0 coil, the current in the B_0 coil was affected by the field cycling pulse. The constant current supply (HP 6267B) has a long time constant that requires seconds to recover from any pulse on the field cycling coil. Because the field cycling coil could not be used as planned, it is possible to connect the two larger coils in series, forming a single coil with 40 turns. This allows us to apply the same field with lower power dissipation. A single coil is operated at around 4 A; the two coils combined in series are usually operated between 2 and 3 A, giving an NMR frequency on the order of 6 kHz.

Frequency encoding gradient: The Maxwell gradient (G_z) coil is typically used as the frequency encoding gradient, but any direction could be used. The frequency encoding gradient is generally operated with a constant current power supply, even during the excitation pulses. Thus, the NMR frequency varies spatially across the sample. As discussed in Chapter 3, a rectangular excitation pulse profile, such as that we typically use of about 1.25 ms, excites multiple frequencies surrounding the excitation frequency, in a sinc profile with bandwidth about 1000 Hz. This gives slightly uneven excitation across the sample which usually has a bandwidth of less than 400 Hz. In the future, one improvement to make would be to only turn this field on during encoding and readout. This is not currently done because it would require a constant current amplifier so that the current would not drift during measurement, and this was not readily available. The G_z coil is generally operated at 100 µT/m with a current of 1.5 A.

4.3.2 Pulsed coils

All pulsed coils are powered by Techron amplifiers in voltage controlled mode, which in turn are controlled by the NMR console (a Tecmag Orion^{TM}). Each pulsed coil circuit passes through a relay at the wall of the shielded room. These relays open during SQUID operation, for the purpose of decoupling the amplifiers and for noise reduction. The relays are controlled by TTL pulses coupled to the relay circuit (Figure 4.7B) through optical isolators (Figure 4.7A). The optical isolators are all in individual Pomona boxes so that they may be placed where they are needed. The relay power supply is connected to several similar circuits in parallel, with each relay controlled by a separate TTL pulse.

Excitation coil (B_1): The orientation of the excitation coil must be orthogonal to B_0, and is placed as orthogonal as possible to B_p to minimize the mutual inductance between the two coils. In some cases, the geometry of the sample requires non-orthogonal placement, such as a 45° relative placement used in imaging the head. The excitation coil is powered by a Techron 608
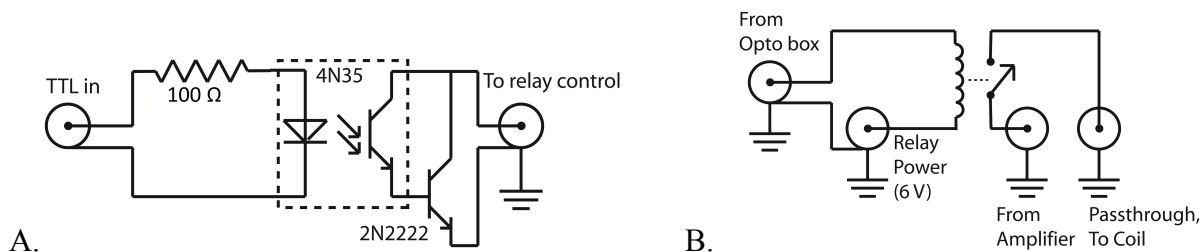
Figure 4.7. Circuit schematics of components of the relay circuits. A: Schematic of the box containing the optical isolator (Opto box). B: Schematic of relay circuit for all pulsed coils except polarizing coil. The BNC connector "From Opto box" can either accept the input from the Opto box, or a shorting cap to activate the relay circuit.
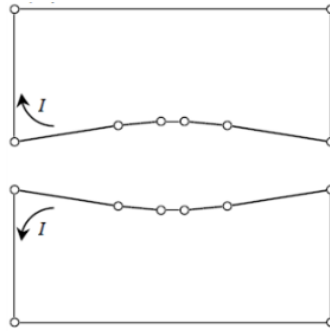
Figure 4.8. Diagram of one plane of the planar gradient coils. Current flows in the direction indicated.

amplifier sourcing roughly 100 mA, and produces a field on the order of 5 µT. To help reduce the effect of the reactive component of the impedance, we have placed a 15 Ω resistor in line. The pulse shape of this coil is generally a sine wave of 8 or16 cycles at the frequency of the NMR.

Phase encoding gradients: We typically use the planar gradient coils (G_x, G_y) as the phase encoding gradients, but any combination can be used here. The G_x and G_y coils are each of biplanar design, with the planes each having a configuration depicted in Figure 4.8. They each have a coil constant of roughly 70 µT/m/A. Details of the exact positioning and calculations can be found in [19]. The pulse shape of a phase encoding gradient is generally a 1 ms linear ramp up, hold for 10-15 ms, and 1 ms linear ramp down, all in the time between the 90° and 180° pulses.

Prepolarization coil (B_p): This coil is wound from 30 individually insulated 28 AWG wires in parallel (litz wire, typically used in high frequency applications). The room temperature resistance of the coil is about 2 Ω. We typically operate the coil with a controlled voltage Techron 7780 amplifier, at 40 V. The pulse control profile (Figure 4.10, top) is a 20 ms ramp up, followed by a hold that can last from 10 ms to 10 s (typically either 300 ms or 2 s), followed by a 20 ms turn off.

This coil must be cooled before use, and between images. The cooling is accomplished with a manifold of liquid nitrogen injected into cooling channels designed within the coil. We typically cool the coil until the overall resistance is 1.4 Ω. Then, after about 250 s of total operating time, the coil warms up to 2.5 Ω, at which point we must cease imaging and the coil must again be cooled before proceeding. Cooling the coil continuously during operation is not advised, because this situation allows for uneven cooling of the wire, leading to hot spots which cause local runaway heating and can burn through the wire insulation. Cooling before imaging gives the wire time to thermalize, minimizing the potential for hot spots.

To isolate the coil during SQUID operation, there are two relays in parallel, each having 4 contacts wired in parallel, on each side of the coil. When the relays have disconnected the coil from the amplifier, they connect the amplifier leads across a 1-Ω resistor. This is important for noise reduction. The polarizing coil circuit is shown in Figure 4.9.
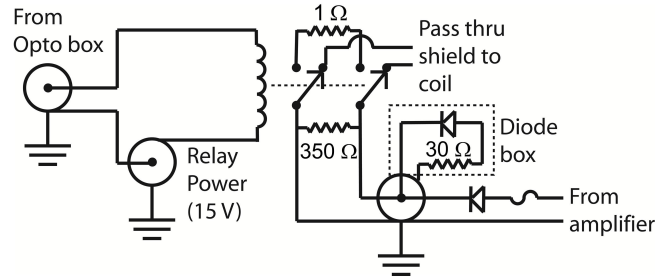
Figure 4.9. Schematic of the polarizing circuit. The same optical isolator box (Figure 4.7A) attaches here for operation of the relays.
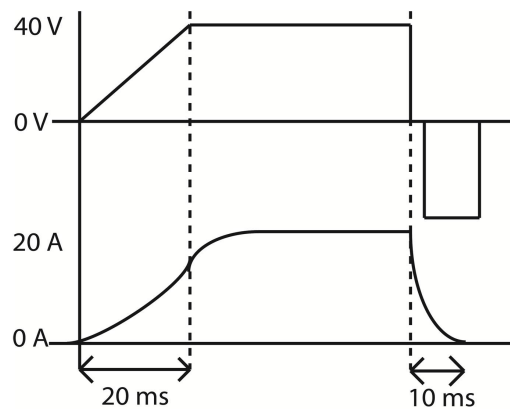
Figure 4.10. Polarizing coil applied voltage and current profiles.

In the circuit is a box containing a fuse, diodes, and the 350-Ω resistor which control the current in the circuit. The diode box indicated in Figure 4.9 attaches to this box via a BNC coaxial connector, with the purpose of increasing the resistance of the circuit during turn off, to allow for a faster turn-off. The control profile for the voltage along with the corresponding current profile in the coil are shown in Figure 4.10.

Most of the measurements described in this thesis were taken with this prepolarization coil. However a major part of the work I have done is in the implementation of a new, higher power, higher field prepolarization coil. The details of this new coil, along with new aluminum shield and auxiliary coils required, will be discussed in Chapter 5.

Belly "cancellation" coil: This coil was implemented because pulsing the B_p coil caused eddy currents in the aluminum shield. This field from the eddy currents was not large enough to affect the MRI, however the drift was large enough to exceed the dynamic range of our SQUID flux-locked loop electronics. To decrease the magnetic field at the wall, this 20-turn, 1.8-m square coil was wound horizontally around the existing coil structure. The height was placed as required (about 0.3 m from the top of the coil structure) to ensure the dynamic range of the SQUID was not exceeded. This coil was counter pulsed at the same time and with the same current profile as the prepolarization coil. This coil decreased the amplitude of the field at the shield walls and therefore decreased the resulting eddy currents. The gain of the Techron 608 amplifier controlling this coil needed to be adjusting by hand throughout the sequence as the

(voltage controlled) prepolarization coil heated up and therefore was pulsing less field. Because we have replaced the aluminum shield with a thinner one in 2010 the eddy currents in the shield have decreased to the point that they do not exceed the dynamic range of the flux-locked loop, and this coil is now obsolete.

4.4   Shielding

As mentioned previously, operation of the SQUID requires shielding against radio frequency interference.   To make use of the high sensitivity of the sensor, sufficient shielding of environmental field noise at the NMR frequency (~6 kHz) is also required, such that the remaining environmental noise is less than the intrinsic SQUID noise of ~0.5 fT $Hz^{-1/2}$.

In this section, I will describe the second generation, 6-mm thick aluminum shield that was used during most of the data acquired here. A third generation, 2-mm thick shield was installed in 2010 to reduce the eddy currents caused by large transient magnetic fields, and will be described in Chapter 5.

The second generation shield (Figure 4.11) was a cube measuring 2.4 m on each side constructed from 6.35-mm thick plates of 5052 aluminum which were bolted to a frame made of 38-mm square hollow aluminum tubing. Three of the sides, the bottom, and top were each constructed from 2 pieces, each 1.2 m x 2.4 m. The front was made from two 0.76-m wide vertical plates on either side of a 1 m wide by 2 m high hinged door. An electrical connection was made from the door to the rest of the shield by compressible copper-beryllium fingers.   The design considerations are more thoroughly discussed in Michael Hatridge's thesis [21].

As a measure of the shielding, I measured with a fluxgate magnetometer the 60 Hz field amplitude outside the shield to be 70 nT_{pp}. Inside the shield it was 8 nT_{pp}. As an additional measure of the rejection of external noise, the field I measured with the SQUID, referred to the bottom loop of the gradiometer, was 0.2 nT_{pp}. This indicates that for 60 Hz, the noise is decreased is a factor of 350. The shielding of the screened room should improve with frequency.

Figure 4.11. Photograph of the second generation shielded room, installed in Birge B203.

Before building this screened room, a copper mesh shielded room was at the location we planned for the aluminum room. We measured the noise with the SQUID and gradiometer inside the copper mesh room. At the precession frequency, the noise in the copper mesh room was gradiometer 1.1 fT Hz$^{-1/2}$ referred to the bottom loop of the gradiometer. After the copper mesh room was disassembled and the aluminum room was built in its place, the noise was again measured with the same SQUID and gradiometer to be 0.75 fT Hz$^{-1/2}$ relative to the lowest loop of the gradiometer. This indicates that the aluminum room improved the shielding of external noise.

Chapter 5

A new, larger prepolarizing coil

5.1 Introduction

In an effort to increase the prepolarizing field toward the requirements for *in vivo* imaging (150 mT at the imaging location), we decided to drastically change our prepolarizing coil technology. The previous polarizing coil used litz wire and liquid nitrogen cooling. As discussed in Chapter 4, the imaging time with this coil is limited. Additionally, we are unable to cool the coil continuously during an image, due to the formation of hot spots. We tried cooling the litz wire coil with water which has a high heat capacity that would enable continuous operation at slightly higher currents than we were previously using. Unfortunately, the high dielectric constant of water drastically increased the turn-turn capacitance of the coil, and thus decreased the-self-resonant frequency of the coil. As a result, the coil would ring down slowly on a timescale of seconds, irrespective of the state of the power supply.

The reason that we have previously used litz wire in the construction of prepolarization coils is that by breaking up the metal of the coil into smaller pieces, the Nyquist noise currents are greatly reduced [22], allowing the metal to be placed in close proximity to the SQUID detector. This requirement can be relaxed if the metal is placed sufficiently far away from the detector. In such a case, it is possible to wind a prepolarizing coil out of copper tubing, with cooling water flowing right through the center of the conductor. This would allow for the benefits of water cooling without affecting the turn-turn capacitance.

Conolly *et al*. successfully used square hollow copper tubing in their prepolarized MRI system, achieving high current densities and field strengths [10]. This wire, 4 mm × 4 mm in outer diameter (shown in Figure 5.1A), produces excessive amounts of Nyquist noise when placed directly next to the gradiometer. However, these fields fall off rapidly away from the coil, so a coil sufficiently far away from the gradiometer can be fabricated with an arbitrary cross section. We were fortunate enough to acquire an unused coil from the Conolly group which was nearly ideal for human arm and brain applications. The coil, shown in Figure 5.1B, has inner diameter 0.324 m, outer diameter 0.413 m, and height 0.115 m. It consists of 240 turns, with an inductance of 24 mH, self-capacitance 0.93 nF, 0.5 Ω resistance, and achieves 150 mT field at

A.

B.

C.

D.
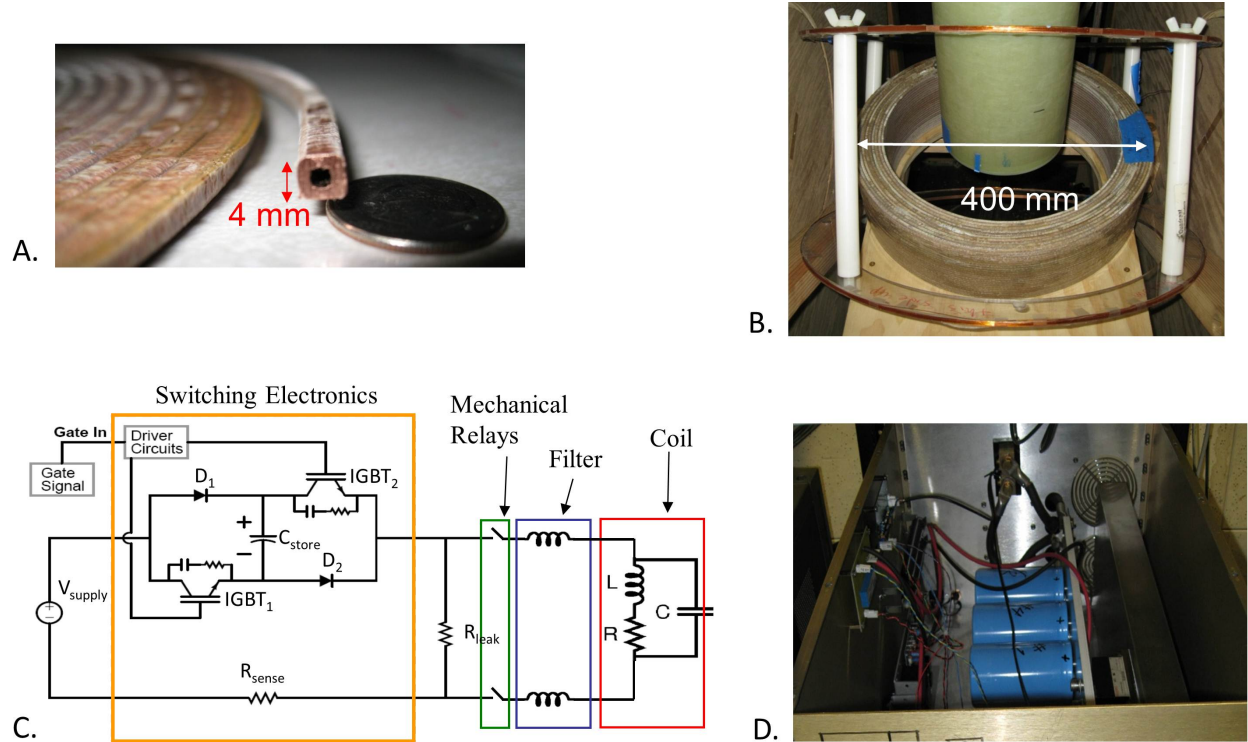
Figure 5.1. Description of prepolarizing coil and associated electronics. A. Image of square-hollow copper tube cross section used to wind coil. Quarter included for scale. B. Image of prepolarizing coil in the MRI system. The outer diameter of the coil is 0.413 m. C. Schematic prepolarizing circuit with switching electronics (orange box), mechanical relays (green), filter (blue), and coil (red) indicated. D. Picture of assembled switcher box. Capacitors are blue cylinders, connected to low-inductance bus (green/white bar). IGBTs and diodes are black objects visible between low-inductance bus and aluminum heat sink.

the center when driven with 200 A (current density of 9.25 A/mm^2, a substantial increase over the litz wire coils with current density 4 A/mm^2).

5.2   Implementation

The coil represents a substantial increase in polarizing field strength and area, but this is associated with substantial infrastructure costs. At 50% duty cycle, the coil dissipates an average of 10 kW, necessitating 1 gallon per minute of cooling water with a 40 °C temperature rise, and the inductive kick when the coil current is switched off is nearly 1 kV. It is no longer feasible to achieve this with a linear voltage amplifier. Fortunately, the Conolly group had also developed a resonant switch technology [10] which could be adapted to use in our SQUID based MRI system. This switch, shown in Figure 5.1C, is a modified H-bridge geometry with three possible current flow paths and a large capacitor in the center of the bridge. Starting with the capacitor uncharged, the Integrated Gate Bipolar Transistors (IGBTs) are biased to the conductive state, and the coil is allowed to ramp up slowly to full current with the current flowing around the capacitor.   Then the IGBTs are biased off, and the current flows through the diodes and capacitor. The current charges over a quarter cycle of the resonance frequency formed by the combination of the coil inductance and the capacitor, transferring the energy stored in the

inductor to the capacitor. At this point, the current drops to zero and the capacitor is held isolated by the combination of IGBTs and diodes. For subsequent pulses, the IGBTs are switched back to the conductive state, the energy held in the capacitor is exchanged with the inductor, and the cycle repeats. This circuit allows the power supply to provide only the static current and power requirements of the coil.

We designed and implemented a similar version of the resonant switch, with the added filters and switches required to make the system compatible with SQUID based MRI. The resonant frequency was designed to be 9 ms, to ensure that the rate of field change from the coil switch is less than the 20 T/s limit set by the FDA. This required a capacitance of 1.7 mF. This was achieved using three Cornell Dubilier 550CE1184 capacitors (selected for their high capacitance, low series resistance and relatively high voltage rating) in series. The series combination was necessary as the voltage rating was only 400 V per capacitor. The capacitors used were selected for matching capacitance values to avoid potentially damaging voltage redistribution effects. The IGBTs (Powerex CM300DY-28H) and power diodes (Eupec ND260N16-K) used were selected for their high breakdown voltage (1400 V) and maximum current (300 A) ratings. Modern IGBTs are designed to switch extremely quickly (300 ns in the model we used) in order to minimize dissipation during switching, so that there must be very little stray inductance in the circuit to avoid voltage transients which can exceed the breakdown voltage of the various components. Consequently, the core elements of the circuit were connected through a custom designed low inductance bus (custom built by Thermaflo), which can be seen in the photo of the finished circuit (Figure 5.1D). In order to dissipate the 20 kW dissipated by the IGBTs and diodes when the 200 A pulse is active, these elements are heat sunk on a large aluminum heat sink which is fan cooled. The IGBTs were additionally protected through the installation of RC style snubbers across them, constructed with 0.5 Ω resistance (Caddock MP2100-0.5 Ω), and 0.2 μF capacitance (3 Cornell Dubilier 942C16S68-F 0.68 μF in parallel) The components used and their connections were carefully designed to minimize stray inductance which can defeat the utility of the snubber.

5.3 Relays and filters

It was also a challenge to identify mechanical relays which will tolerate 200 A while also switching in a few milliseconds. We used Gigavac model G2SP relays, which switch in around 10 ms (this becomes longer as the switches age). These switches are actually intended for high voltage applications, but seem to be holding up well in our application. Most switches explicitly rated for 100 A or greater currents are motor/generator contactor style switches, and their switching times and isolation properties are completely unsuitable. A mercury or equivalent wetted switch would be ideal due to their extremely low contact resistances, but we were unable to identify a commercial product with the needed properties.

5.4 Adiabatic turn off of prepolarizing field

This prepolarization field has a turn-off profile that is inherently non-adiabatic for our B_0 field, oriented perpendicularly to the B_p field. Using a non-adiabatic turn-off instead of a 90° pulse is commonly used in other implementations of the prepolarization technology [23], however this

requires the field direction of the B_p to be fairly homogeneous. This would likely require a two-coil system, doubling the power of a single coil. In prepolarized MRI, as long as the prepolarization field is turned off adiabatically, the spins will align with the spatially homogeneous B_0 field. This alleviates homogeneity requirements on the B_p coil, because any inhomogeneity in field direction will be corrected, and any inhomogeneity in field amplitude will manifest as a smoothly varying and correctable intensity variation. The adiabatic condition can be expressed as

$$\frac{d\theta_B}{dt} = \frac{d}{dt}\left\{\tan^{-1}\left[\frac{B_p(t)}{B_0}\right]\right\} = \frac{dB_p/dt}{\left[B_0 + B_p^2(t)/B_0\right]} \ll \omega = \gamma\sqrt{B_0^2 + B_p^2(t)}, \qquad (5.1)$$

where θ_B is the angle between the total applied field and the direction of B_0, and ω is the spin angular precession frequency. Assuming dB_p/dt is constant, $d\theta_B/dt$ has a maximum at $B_p=0$, and Equation 5.1 reduces to $dB_p/dt \ll \gamma B_0^2 = 5.2$ T/s for $B_0 = 140$ μT. The quarter sine wave profile has $dB_p/dt = 26$ T/s and would therefore need to be modified. There are two ways that one could imagine doing this: One is to slow down the end of the polarizing pulse, by implementing a coil parallel to B_p which is turned off in a controlled way after the quarter sine wave turn-off of B_p. The second is to temporarily raise B_0 during the turn-off. We chose to implement the second option.

Because we run the B_0 coil with a low-noise current controlled power supply with a long time constant, an additional coil was made for this purpose. The coil arrangement along with the B_0 coil is depicted in Figure 5.2.The additional field need not be very homogeneous, so a pair of small coils with diameter 0.36 m and 37 turns is used for this purpose. By winding an additional turn on each side around the B_0 coil in the opposite direction, the mutual inductance between this coil and the B_0 coil of 220 μH was reduced by two orders of magnitude to 2.6 μH to prevent additional transients from occurring.

This coil is powered with 18 A, which along with the B_0 field produces a total field of about 800 μT. The field is turned on during the prepolarization pulse, and is ramped down linearly in 10 ms beginning right after the prepolarization pulse is finished.

The improvement in NMR can be seen in Figure 5.3. The red line shows the NMR peak before the adiabatic turn off pulse was implemented. The black line, which is higher amplitude and more symmetric, shows the NMR peak after the pulse was implemented. The data here are the results of a simple spin-echo sequence. After implementing the adiabatic turn off, we also measured the measured NMR peak when omitting the 90° excitation pulse from the spin-echo sequence. If the turn-off of the B_p is non-adiabatic, there would be an NMR peak. If the turn-off of the B_p is adiabatic, there should be no NMR peak. Indeed, after the adiabatic turn-off pulse was implemented, the NMR peak was negligible even after 100 averages. This indicated that the level of adiabaticity is sufficient, and there is no significant component of the magnetization left in the transverse plane.
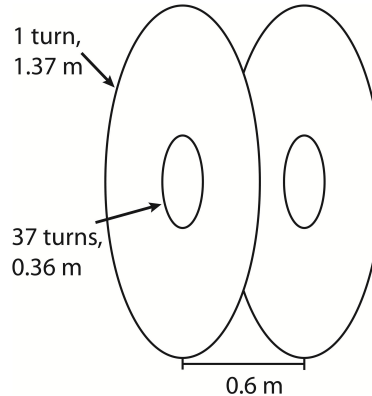
Figure 5.2. The additional coil constructed to ensure the adiabatic turn off. The coil is wound with 37 turns on the smaller frame, and with 1 turn in the opposite direction wound on the larger frame. The B_0 coil is also wound on the larger frame.
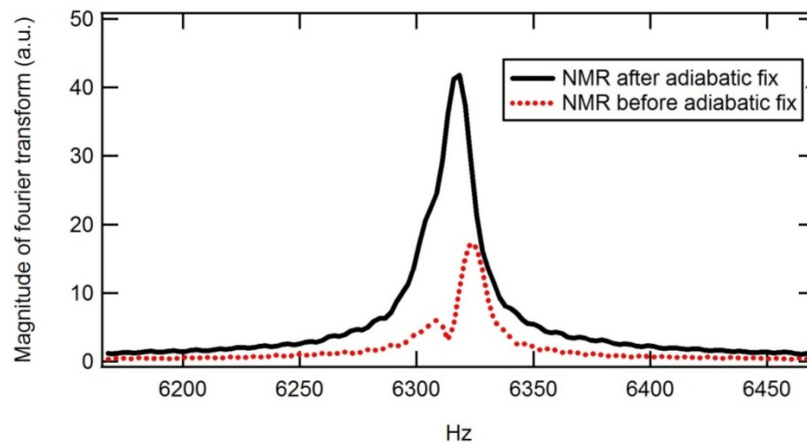
Figure 5.3. NMR amplitude spectrum before (red) and after (black) ensuring the adiabatic turn-off of the prepolarization pulse.

5.5   Eddy currents in aluminum shielded room

5.5.1   Second generation aluminum room description

A cubic aluminum shielded room surrounds the MRI system. For successful implementation of this larger prepolarization coil, the previous room needed to be replaced.   The previous-generation room had dimensions $2:44 \times 2:44 \times 2:44$ m^3 (8 ft^3), and was made of 6.4-mm-thick (1/4") aluminum plates. The plates were bolted tightly to a frame made of hollow aluminum bars, using a great number of brass bolts. Even without welded seams, a shielding factor of 10 was achieved at the fairly low frequency of 60 Hz.

This water cooled coil, with its much larger dipole moment compared with previous prepolarizing coils, caused eddy currents to flow around the aluminum room and in the plates. As shown in Figure 5.4, the field produced at the center of the room was larger than B_0 and decayed with a time constant of 50 ms. This timing corresponds roughly to the T_1 and T_2 timescales of tissue, and therefore waiting until the eddy currents was not possible.
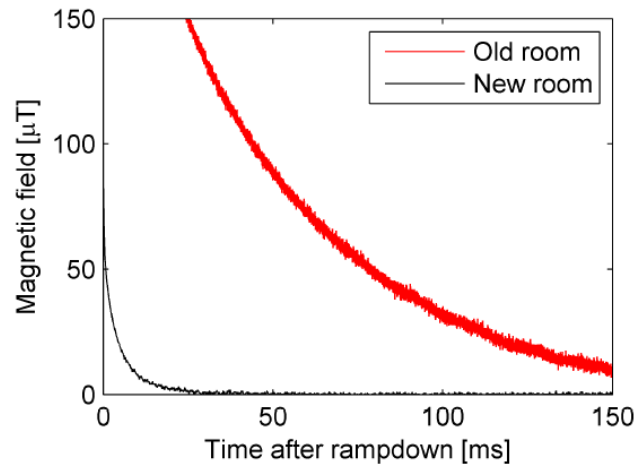
Figure 5.4. The transient magnetic fields produced by eddy currents in the old (red line) and new (black line) aluminum shielded rooms. Time t=0 corresponds to the end of the quarter sine wave turn off profile of the prepolarization coil.
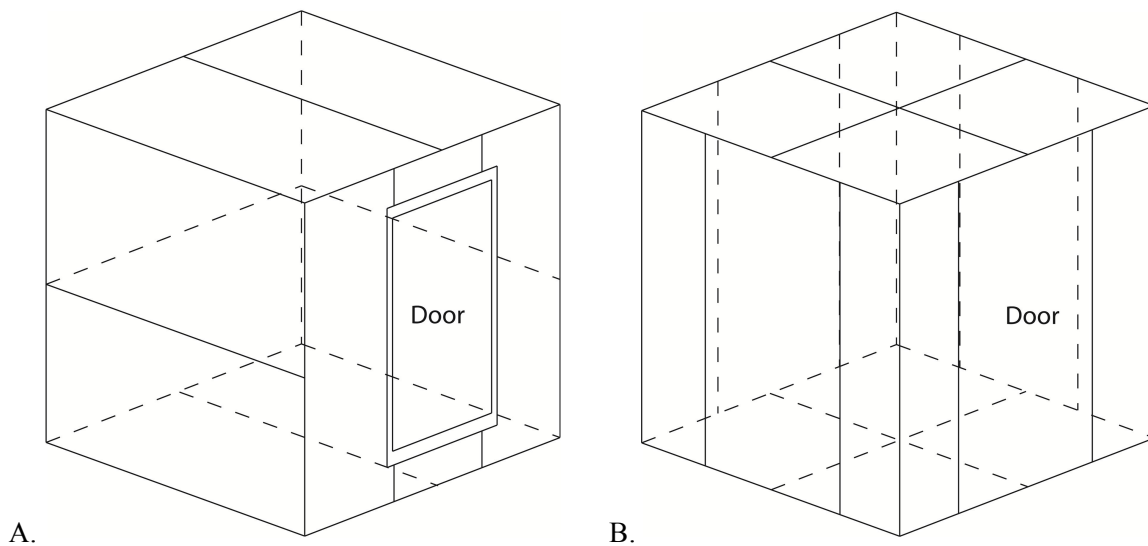
Figure 5.5. Schematic of the arrangements of the aluminum plates in (A) the previous aluminum shielded room with 6.4 mm-thick plates, and (B) the new aluminum with 1.6 mm-thick plates. Both rooms measure 2.4×2.4×2.4 m^3.

5.5.2 Third generation aluminum room description

The time constants in the shield can be controlled in two ways. First, decreasing the thickness of the shield brings more resistance in the eddy current circuits, shortening the time constants. Second, using disconnected or weakly connected plates reduces the sizes of the effective current loops, which removes the modes with the longest time constants in the system. Given that a door in the room already introduces weak connections between plates, and that the resistances of connections at the edges of the cube are difficult to regulate, a combination of both approaches was used. To keep a high level of symmetry in the design, each of the four sides was divided into individual plates in the same way as the front wall, which has a door in the middle. The division is illustrated by Figure 5.5B.

A high priority was given to symmetry for two reasons. Should one, for whatever purpose, require a smaller transient than produced by the shielded room, the compensation is much easier when the room is highly symmetric. With a B_p coil centered and aligned with the room, the transient is homogeneous to first order at the center. Such a field can be compensated to a high accuracy in a small volume by using just one compensation coil, or afterwards by software. Conversely, a transient from an asymmetric room, such as the previous shielded room shown in Figure 5.5A, with its complicated spatio-temporal profile can be difficult even to analyze. The other thing in favor of symmetry is that an asymmetric shield can turn an external uniform field into a gradient detectable by the gradiometer, resulting in an increase in noise instead of shielding. We also explicitly chose not to divide the wall plates by a horizontal seam because the transient eddy currents due to a polarizing pulse do not cross the horizontal symmetry plane. Therefore, a division along that plane would not reduce the transient, but only impair the shielding. However, carefully chosen horizontal division planes symmetrically around the middle plane could reduce the transient, while not compromising the shielding.

The new aluminum shielded room was made the same size as the previous one. Based on measurements of the current paths and estimations of how the time constants scale with plate dimensions, the thickness was chosen to be a quarter of that of the previous room, 1.6 mm (1/16"). The aluminum alloy used was 6061. To keep the plates electrically separate, the supporting frame was made of wooden 2"× 2" boards (finished cross section 38 × 38 mm^2). The sheet metal was bolted onto the frame using steel bolts, and masking tape was used to prevent direct electrical contacts between the plates. The new shielded room is shown in Figure 5.6.

To make the shield effective against RF interference, which is required for the SQUID to operate, the narrow slits between the plates were covered by 2" wide aluminum foil tape. Further complying with the symmetry requirements, tape with a conducting adhesive was used

Figure 5.6. Photograph of the new aluminum shielded room.

for the corner seams as well as the seams dividing the ceiling and floor. Before applying the tape, the surfaces were cleaned with vinegar and isopropanol to remove the oxidized surface. The other seams were covered using tape with a non-conductive adhesive. The door plate, which was suspended of four heavy-duty stainless-steel hinges, was RF sealed using a commercial EMI gasket. The gasket is a strip of rubber foam covered with a conducting fabric such that even a modest pressure will seal the electrical connection along the full length of the seam. While one side of the gasket touches the door plate, the other touches a thin aluminum strip that overlaps with both the door plate and the surrounding plates. The strips are kept from direct contact with the surrounding plates by an insulating layer of masking tape, although RF-sealed to them using aluminum foil tape with non-conductive adhesive. Pass-throughs for coolants and helium gas were implemented by the same wave-guide-type pass-throughs present in the old shielded room.

The eddy currents from the new shielded room are indeed reduced compared to the previous shielded room (Figure 5.4). The longest time constant of the eddy currents was measured to be 5.8 ms. At 15 ms after ramp-down, the transient has decayed to roughly 5 µT. Since this field is perpendicular to B_0, the total field magnitude is $\sqrt{132^2 - 5^2}$ µT = 131.9 µT. The change from B_0 = 132 µT is less than 1 part per 1000, corresponding to a frequency shift of 4 Hz. This is the same order as the natural line width of the NMR peak of typical soft tissue, and can therefore have only a minor effect from an imaging point of view. At 20 ms, the transient has practically no effect at all.

5.5.3   Third generation room shielding capabilities

The results of noise scans by our gradiometer in identical situations in the two rooms are shown in Figure 5.7. The new shielded room shows a much higher contribution from 60 Hz harmonics below our imaging band, and many more and stronger interferers above our imaging band. However, as shown in Figure 5.7B, the noise is our imaging band did not change much. This may be because we are limited by the intrinsic noise of our detector instead of external noise. In any case, the new shielded room is perfectly adequate from a shielding point of view, as well as from an eddy current point of view.

5.6   Induced voltage on other field coils from the pulsed polarizing coil

The eddy currents in the shielded room were not the only B_p-induced transients. The mutual inductance of the polarizing coil and the Earth's field cancellation coil in the same direction is high. For high stability and low noise, the DC current source used for the cancellation coils has a slow response. During the ramp-down of the polarizing pulse, and EMF is induced in the cancellation coil. The current source attempts to compensate for the EMF, but cannot keep up with it. After the ramp-down, the EMF is zero, but a current transient remains (Figure 5.8A, red line), with a time constant of 15 ms.

A.

B.
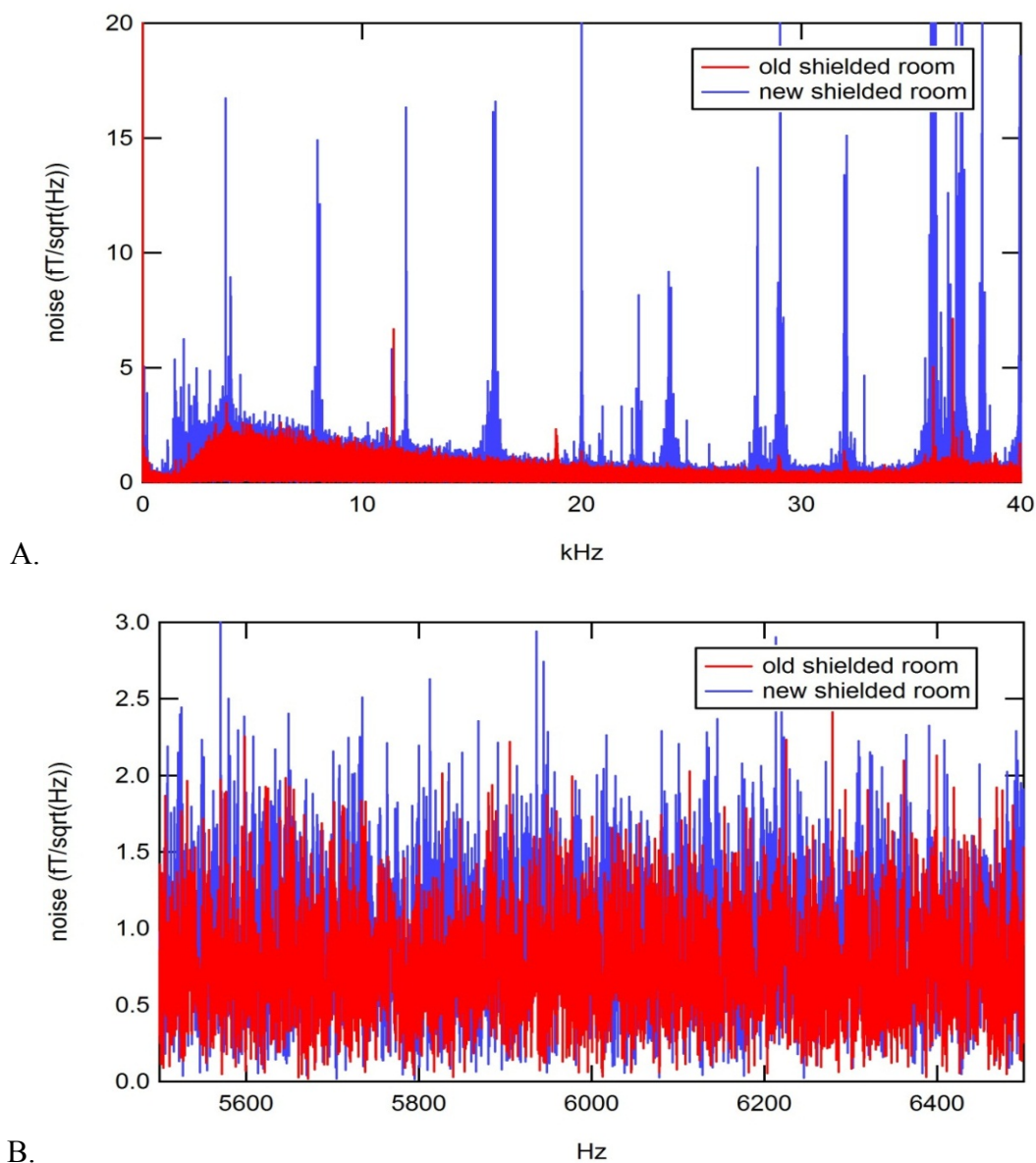
Figure 5.7. The noise spectrum as measured by our SQUID gradiometer in the old shielded room (red) right before disassembly, and in the new shielded room (blue) right after assembly. There is a bandpass filter from 3-10 kHz. A: Broadband noise spectrum. B: Noise in imaging band.
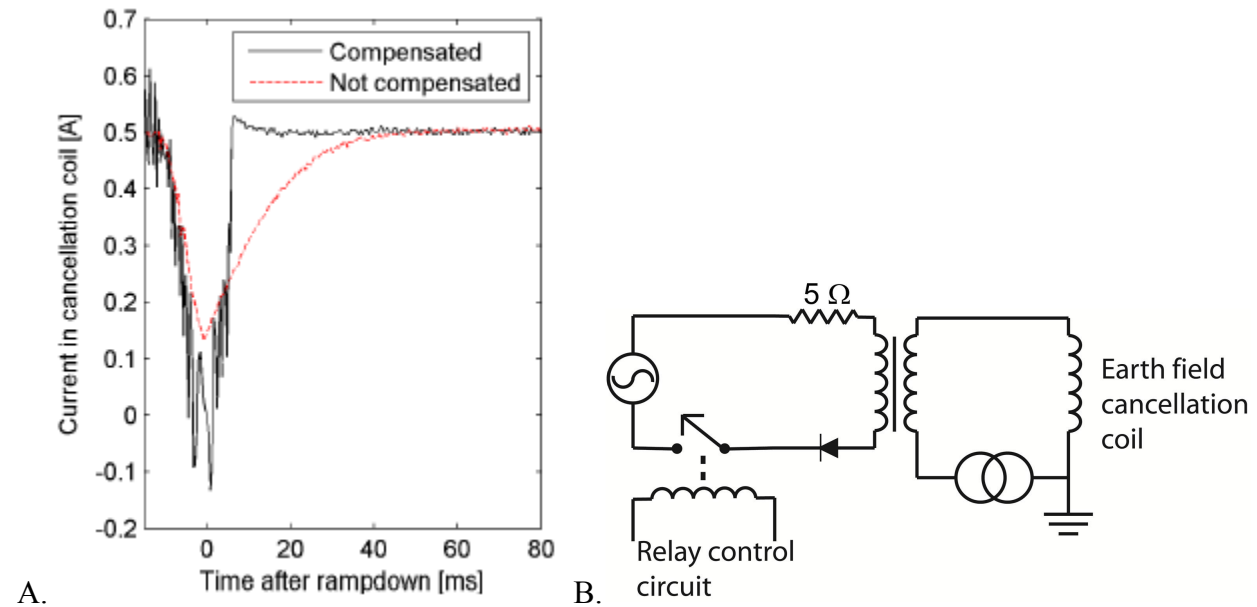
Figure 5.8. Induced current drift in Earth's field cancellation coil, and correction scheme. A: Current in the vertical Earth's field cancellation coil. A change in current of 0.5 A represents a 25 µT field change perpendicular to the B_0 field. B: Compensation circuit. A controlled waveform is coupled to the earth field cancellation coil via a transformer. The pulse is tuned so that the current in the earth field cancellation coil returns to the correct value as soon as possible after the polarization pulse.

Figure 5.9. The transformer used for solving the issue of current transients in the earth field cancellation coil due to polarizing pulses.

This problem was solved by inductively coupling a separate coil to the earth field cancellation coil via a steel-core transformer (Figure 5.9) originally used in a power supply. The primary was connected in series with the cancellation coil, while current was pulsed into the secondary during the polarizing pulse. Because of eddy currents in the steel core and other effects, the transformer becomes increasingly dissipative at high frequencies. Frequency dependence of the core

properties also introduces rounding and phase shifts in the response. The presence of such effects was evident from the softened shape of the induced EMF in the primary. As the effective pulse shape was not as intended, the fully simultaneous compensation of the B_p pulse did not work properly. To overcome this problem, the current pulse in the transformer was switched off after the ramp-down of B_p, and by careful tuning of the current and timing of the pulse, the transient could be suppressed to a sufficient accuracy. The response of the cancellation coil current source had apparent nonlinearities, and some smaller transients and oscillations remained, but which were small enough to be harmless (Figure 5.8A, black line).

5.7   Safety considerations

With the implementation of the larger prepolarization coil powered with 200 A, dissipating 20 kW, and transient voltages of around 1 kV, there were many safety issues to consider. The IGBTs are controlled with Powerex's purpose built IGBT driver circuit (BG2A), and the switching signal is provided by a logic circuit which integrates a number of interlocks together with both manual and computer external controls. One interlock connects to a water flow meter (Proteus Industries 203C24) mounted in series with the cooling water line downstream from the coil; flow drop below the set threshold switches the coil off and prevents further pulses that would heat the coil to the point of damage. Another interlock internal to the switcher box measures the electrical current returning from the coil, and prevents the mechanical relays from being opened unless the current flowing through the coils is less than an amp. A third is mounted with the mechanical relays, and prevents the coil from being switched on if the relays are open. The current is provided by a MagnaPower TS200-125 switched-style power supply, operated in constant-voltage mode. The high efficiency of the supply is very desirable in order to decrease the total power required by the experiment. However, its internal semiconductor switches generate a substantial 8 kHz signal as well as broadband current noise which is transmitted through the switcher box and relays even in the off state. This was addressed through the addition of ferrite cores between the power supply and the switcher box, and at the wall of the shielded room.

In the event that an IGBT breaks, the current flowing through the coil would be continuous and proportional to the voltage of the power supply. We use the computer inputs on the power supply to control the voltage of the supply to be high only for the period just before and during the time the pulse should be on. This has the additional benefit of decreasing the noise contribution from the power supply. Another protection circuit senses the current in the coil and compares it to the intended state of the pulse. If these are found to be incompatible, then a signal is sent to to the power supply's interlock to place the power supply in standby.

Because this system was intended to use with human subjects, it is necessary to ensure that the subjects would be protected from the high voltages present. Because we did not find commercially available tubes with the desired diameters in materials such as PVC or fiberglass, we made a custom enclosure. The enclosure is cast urethane (TC-892 A/B from BJB Enterprises) of thickness no less than 0.25" at any point. The enclosure has been verified to withstand voltages of above 2 kV.

5.8 Conclusions

We have successfully implemented this coil. The images of the NIST phantom described in Chapter 6 were acquired with this coil. We are in the process of complying with requirements from UC Berkeley's Environmental Health & Safety department in order to obtain human subjects certification before imaging human subjects with this coil.

Chapter 6

NIST phantom

To develop standards for ULF MRI, a team at the National Institute of Standards in Boulder, CO, including Ben Mates, Hsiao-Mei Cho, Michael Boss, Gary Zabow, and Kent Irwin, are designing standard phantoms. They visited in November 2010 to test some of their designs on our system. The phantoms included substances for proton density, T_1, and diffusion measurements. In collaboration with us, they developed a geometry suitable for use with our ULF MRI system, using either of the two prepolarization coils described in chapters 4 and 5. The data were acquired using the new water-cooled prepolarization coil.

The phantom consists of several vials 13 mm in diameter and 19 mm high that are arranged inside another cylinder that is 76 mm in diameter and 25 mm tall. The interior dimensions of this larger cylinder are 64 mm in diameter and 19 mm tall. To image at high fields, the larger
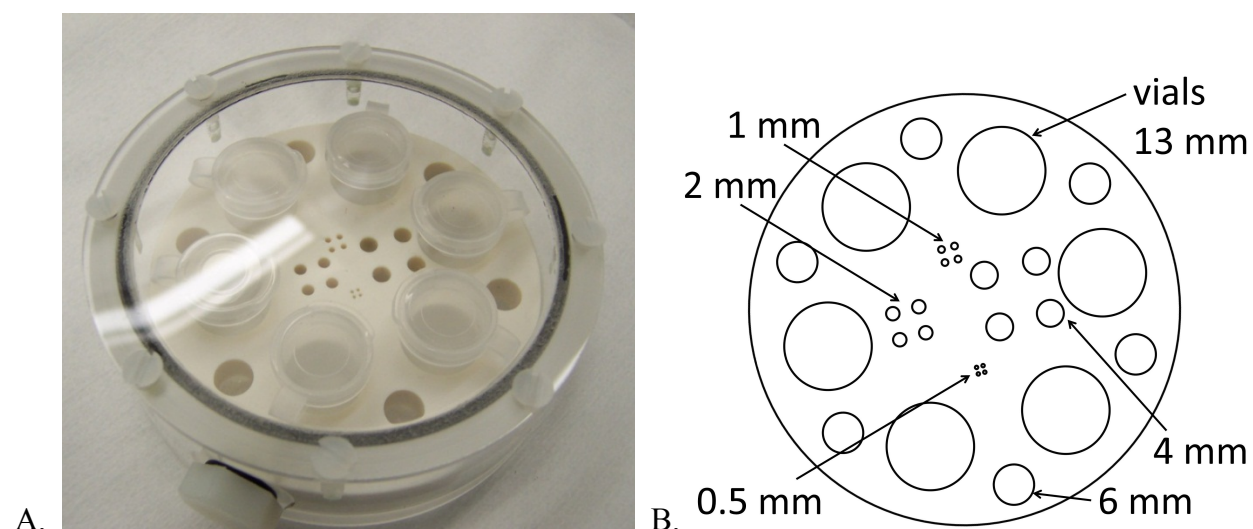
Figure 6.1. Images of a 6-vial phantom and resolution inset. A: Photograph of the phantom. The 6 vials contain various substances, described in the text for each phantom. The white plate is the resolution inset, with various diameter holes. The space inside the phantom can be filled with liquid (e.g. DI water) through the fill port on the bottom left. B: Diagram of the phantom showing the various hole sizes in the resolution insert.
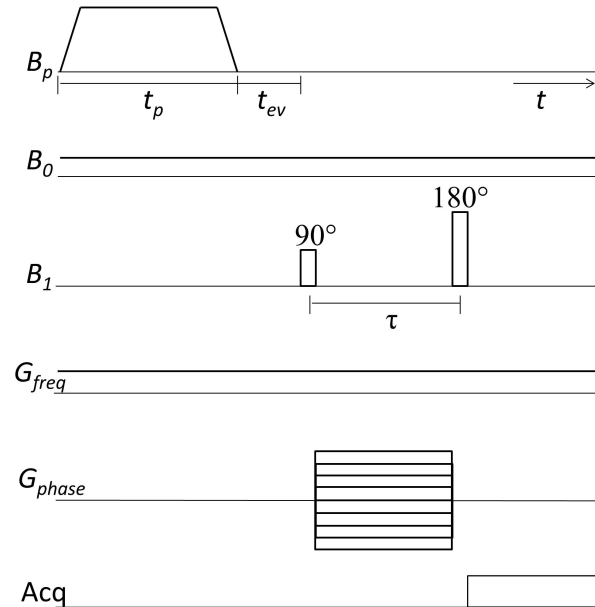
Figure 6.2. 2D imaging pulse sequence. For T_1 measurements, this image is repeated, changing the time t_{ev} for each image.

cylinder needs to be filled with liquid to avoid any susceptibility artifacts; however at low field this is not an issue. There are multiple phantoms, with each phantom containing either 6 vials and a resolution inset (Figure 6.1), or 10 vials. The resolution inset Figure 6.1B is a plate 6 mm thick with holes of varying diameters drilled in it: 4 holes each of diameters 4 mm, 2 mm, 1 mm, and 0.5 mm, along with 6 holes of diameter 6 mm and 6 holes of diameter 15 mm to hold the vials. A photograph of the 6-vial phantom is shown in Figure 6.1A.

The images were acquired with our standard 2D imaging sequence shown in Figure 6.2. Standard images are acquired with t_{ev} = 0 ms, and T_1-weighted images are acquired with a specified t_{ev}.

6.1   Proton density phantom

The 6 vials in the proton density phantom each contain different amounts of deionized (DI) water mixed with heavy water. Heavy water is water made with the hydrogen isotope containing deuterium, ^2H. This isotope of hydrogen has a different magnet moment than ^1H, and therefore a different precession frequency in a given field, and does not contribute to the ^1H NMR signal that we usually detect. Figure 6.3B shows the percentage of DI water in each vial. Measurements of this phantom were acquired using the standard 2D imaging sequence shown in Figure 6.2 with t_{ev} = 0. The resulting data are shown in Figure 6.3.

A plot of intensity of versus the percentage of DI water is shown in Figure 6.3C. The intensity scales linearly with the spin density, as expected. The exact slope of the line will vary with parameters such as: position with respect to pick up loop and polarizing coil, size of voxel, and imaging parameters like prepolarization time, low field T_1 delay time, and echo time.

A.   B.   C.
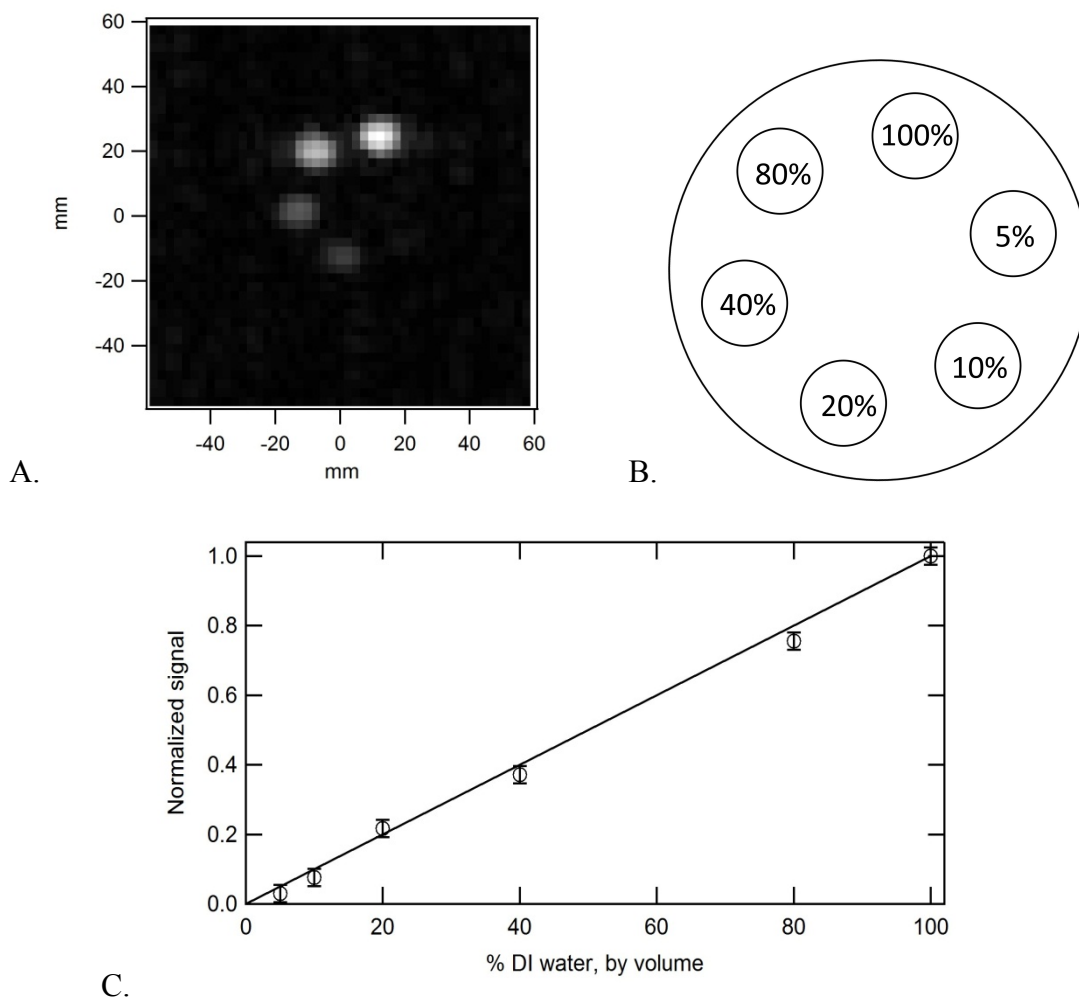
Figure 6.3. Measurements of the proton density phantom. A: MR image of the proton density phantom. The orientation of the phantom is shown in B. This MR image was acquired with only the vials, and without water filling the rest of the phantom. Image parameters: B_p=1 s, t_{ev}=0 ms, t_{phase}=15 ms, G_{freq}=90 µT/m, 21 phase encoding steps of 0.195 µT·s/m each. B: Schematic of orientation of the phantom. The numbers indicate percentages of DI water in each vial. Heavy water makes up the balance. C: A plot of intensity of each vial, normalized to the intensity of the 100% DI water vial, versus percentage of DI water in the vial. The line is y = 0.01 x.

6.2   T$_1$ phantom

This phantom consists of 10 vials filled with different concentrations of manganese chloride (MnCl$_2$) in water. The data were acquired using the standard 2D T$_1$ weighted imaging sequence shown in Figure 6.2. The first phantom consisted of concentrations as depicted in Figure 6.4A. The concentrations near 2 mM and near 0.5 mM caused too much relaxation for the timing of our system, resulting in very low- to no detectable magnetization in those vials. Figure 6.4B shows the MR image acquired with the shortest low field evolution time t_{ev} possible.   The magnetization from the vials on the sides has already relaxed too much for our system to be able to acquire any signal, indicating that we will be unable to measure the T$_1$ from these vials.
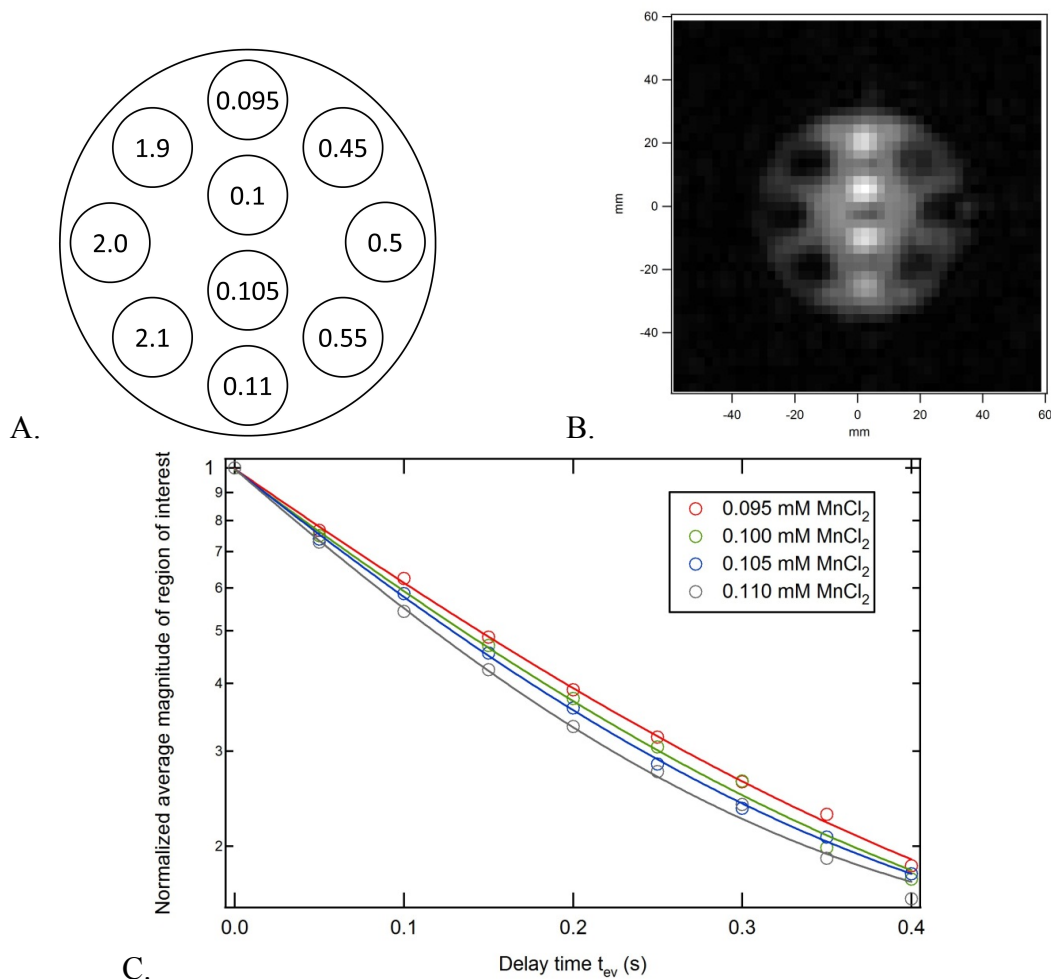
Figure 6.4. Images of low field T_1 phantom. A: Diagram of phantom. Numbers represent concentration of $MnCl_2$, in mM. B: MR image of phantom with shortest timing (highest intensity) possible. The signal from ouside the vials is from water filling the phantom. C: Plot of intensity versus low field delay time for each of the 4 center vials.

For the vials in the center column, we were able to acquire T_1 values for each vial. This was achieved by acquiring ten images, each with a different evolution time t_{ev} between prepolarization and excitation. The delay time increased by 50 ms for each image. We averaged the magnetic field intensity in a square measuring 6 mm × 6 mm centered on each vial. These values were then fit to the function $y = A \cdot exp(-t_{ev}/T_1) + y_0$. The results are displayed in Figure 6.5A. The same phantom was subsequently imaged in a GE 3T scanner at NIST. T_1 values were determined by inversion recovery, and are displayed in Figure 6.5B. At low field, we see a linear increase in $1/T_1$ vs. concentration, whereas at high field the data are scattered. These data demonstrate that we see better T_1 contrast at 132 µT than at 3 T.

Subsequently, the left and right columns of vials of the phantom were replaced with lower concentration solutions of $MnCl_2$. The concentrations were designed to be 0.21 mM, 0.2 mM, 0.19 mM, 0.31 mM, 0.3 mM, and 0.29 mM, but data taken from 7-T NMR show that they are 0.221 mM, 0.220 mM, 0.214 mM, 0.311 mM, 0.312 mM and 0.292 mM. The orientation is
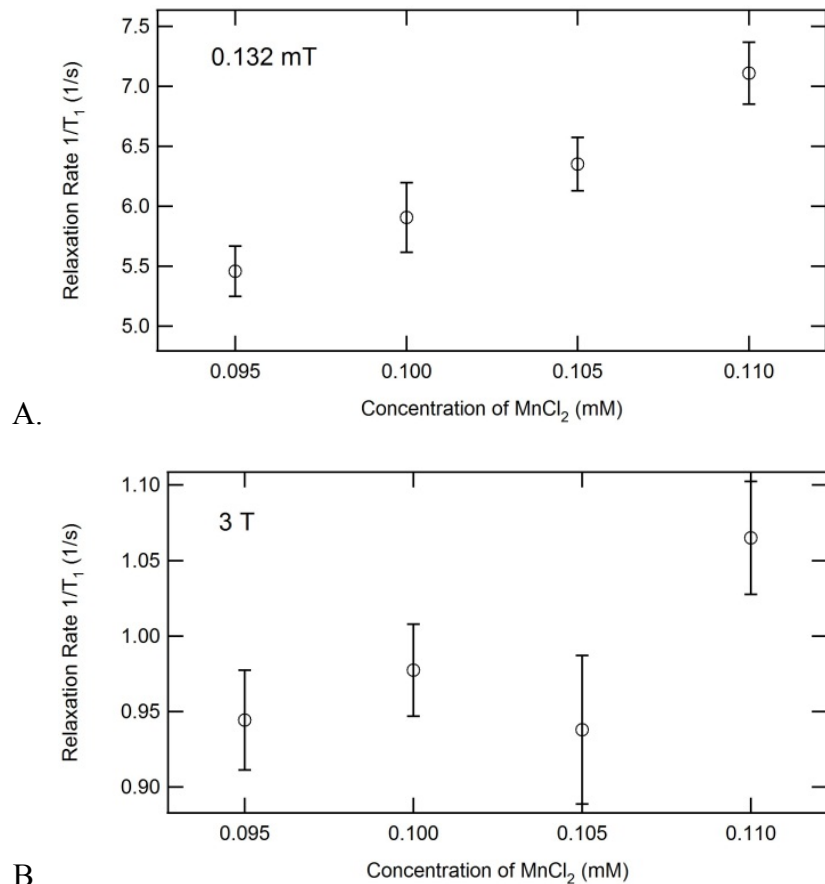
Figure 6.5. Dependence of relaxation rate on concentration of manganese chloride. A: Relaxation rate in 132 μT versus concentration of manganese chloride. B: Same display but after measuring the vials in a 3 T GE scanner.
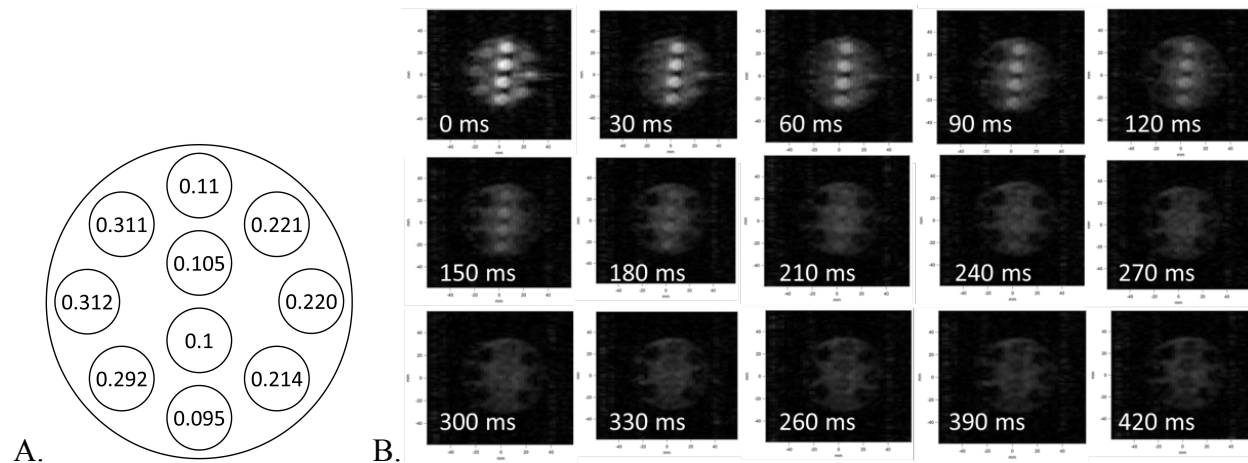
Figure 6.6. Images of the second version of the T_1 phantom. A: Concentrations of $MnCl_2$ in version 2 of the T_1 phantom. B: Images of the phantom v.2 acquired with low field delay times indicated in the labels. The signal from outside the vials is from water filling the rest of the phantom.
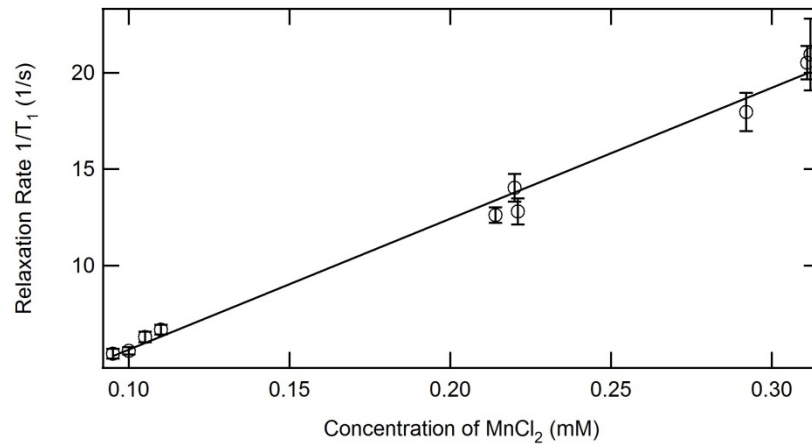
Figure 6.7. $1/T_1$ versus concentration of MnCl$_2$. The line is a linear fit to the data, with slope 67.9 +/- 2.5 mM^{-1} s^{-1}, as expected [24].

shown in Figure 6.6A. The images at each t_{ev} are shown in Figure 6.6B. At t_{ev} = 0 ms, all vials show signal, compared with the first version of the phantom where the side vials were already dark (Figure 6.4B).

Using the same fitting technique as described for version 1 of this phantom, we found the T$_1$ values for each vial. We then plotted the relaxation rate against concentration of MnCl$_2$, shown in Figure 6.7. As expected, we see a linear increase in the $1/T_1$ compared to the concentration of MnCl$_2$ with slope 67.9 +/- 2.5 mM^{-1} s^{-1}, in good agreement with Bloom [24], who finds 66.7 mM^{-1} s^{-1}.

6.3   Resolution phantom

The third type of phantom that we imaged was the resolution phantom. This phantom was originally designed as a 6.4-mm thick Ryton$^®$ plate with holes of varying sizes drilled in it and can be seen in Figure 6.1. One plate takes up roughly one-third of the vertical space in the phantom. The phantom is meant to be filled with water, and in a three-dimensional image, some slices showing a horizontal plane would show only the water in the holes of the phantom, whereas some slices would be completely filled with water. However, in our system, a high resolution three-dimensional image was not possible; therefore, we combined two of these plates, such that the columns took up 12.7 mm of the 19 mm space, and only filled the phantom with enough water to sit in the holes and not extend in the empty space above the plates. The water used was a roughly 0.1 mM solution of MnCl$_2$ to decrease the prepolarization time needed. This allowed us to acquire a two-dimensional image, shown in Figure 6.8A. The orientation of the resolution phantom is shown in Figure 6.8B.

The imaging parameters were as follows: 16 averages, t_p = 800 ms, t_{phase} = 15 ms, 101 phase encoding steps of 0.26 µT·s/m each, G_{freq} = 120 µT/m, and t_{ev} = 0 ms. The prepolarization field was around 120 mT. Total scan time: 2.4 hours, including 1.4 hours of waiting time between pulses required to cool the prepolarization coil which could be eliminated with a higher water flow rate. The SQUID noise between 60 Hz harmonics was 2.2 fT Hz$^{-1/2}$. The line on the zero
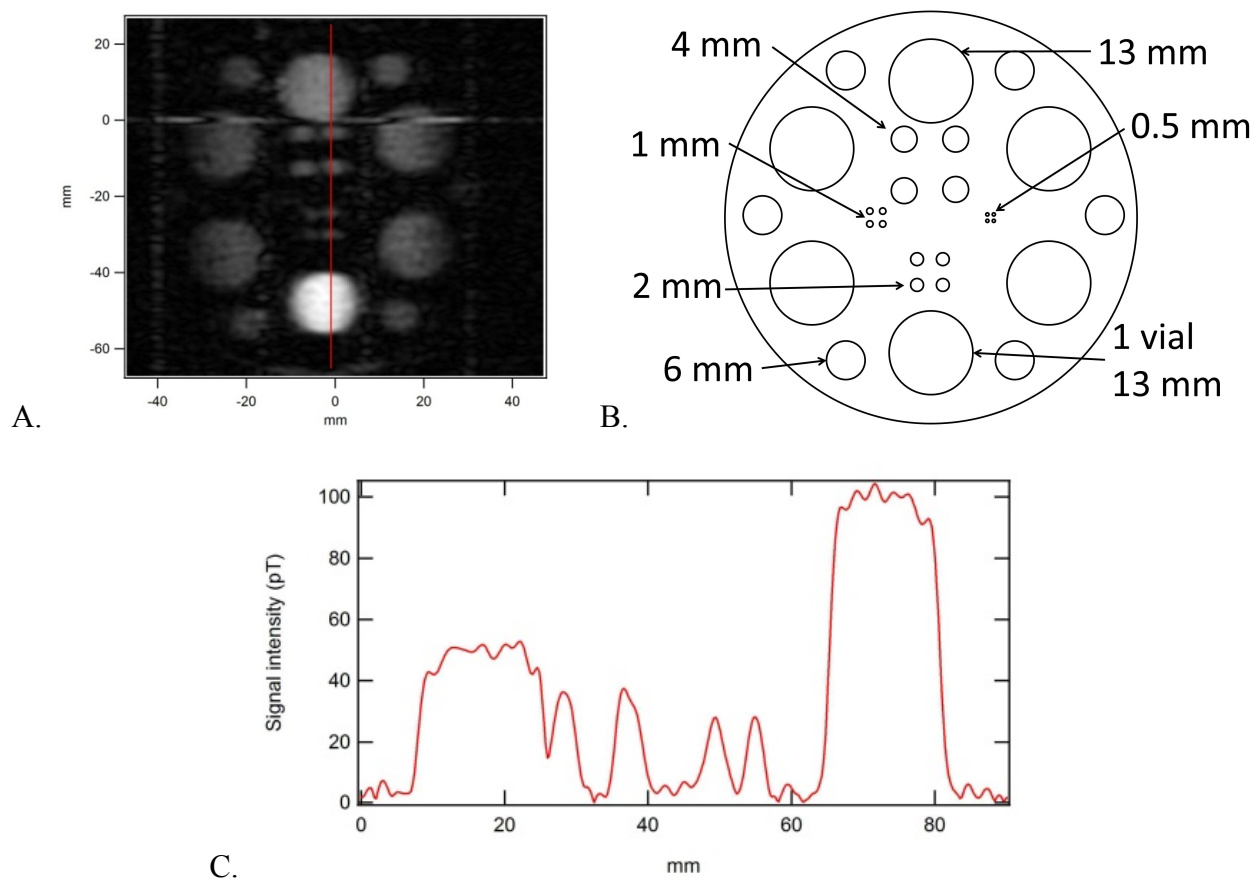
Figure 6.8. Resolution phantom images. A: High resolution image of the resolution phantom. The two grids were aligned by placing a vial in one of the larger holes (bright circle). The red line shows where the cut from C is taken from. B: Schematic of the orientation of the resolution phantom. C: Vertical intensity profile from A. The half-width of edges is 1.5 mm.

trace is caused by excess spins that have not been affected by the phase encoding gradient, and therefore contribute the same signal in each of the phase encoding lines, causing a delta function in the reconstructed image. We hope to eliminate this artifact in the near future. The 2 mm diameter columns in this image are clearly visible. Figure 6.8C shows a profile of the image in the vertical direction and is useful in determining the resolution of the image. The half width of the edge is 1.5 mm.

6.4   Discussion

The results of this study will enable us to help develop useful phantoms for imaging at ultralow fields. For example, the size and distributions of the proton density phantoms were adequate for calibrating our system. We learned that concentrations of $MnCl_2$ in the range of $0.1 - 0.3$ mM correspond to T_1 values typically seen *in vivo* at low fields (50 ms to 200 ms), and therefore would be a good range of concentrations to cover with the phantom. As well, further thought may need to be put into the resolution phantom to decide what parameters are valuable. For

example, a "negative" of the resolution phantom shown here may also be valuable, to measure the detection limit of dark areas.

In addition, the NIST group plans to test phantoms for diffusion weighted imaging, where the brightness of the image is related to the water diffusion constant, at ultralow fields. Unfortunately, the gradients required for such imaging are on the order of 500 mT/m—about 3 orders of magnitude higher than the capabilities of our current system. With the addition of a dedicated gradient coil, our ULF MRI system can be modified for diffusion imaging. At the time, though, there is no plan for this modification.

Chapter 7

Application to cancer

Some cancers—for example, breast cancer and brain cancer—can be imaged with high field MRI using T_1-contrast induced by an injected contrast agent, usually containing a Gd salt [25,26]. This technique, however, is unsuccessful in imaging some cancers like prostate cancer [9]. The value of T_1 of many tissues depends strongly on the magnetic field strength. T_1 values generally decrease as the magnetic field decreases below, say, 1 mT, but the rate of change in T_1 varies from tissue to tissue [5]. Thus, for certain tissues, the difference in $1/T_1$ values, and thus the contrast in an image, will be enhanced. However, the means to acquire images *in vivo* in microtesla fields that may possibly be of high enough quality to be useful to the medical community have been lacking until recently [8]. In this section, we report a study of *ex vivo* prostate tissue using our ULF MRI system aimed at investigating whether significant intrinsic T_1 contrast between healthy and cancerous tissue can be achieved at ULF. We describe and our techniques to measure T_1 and acquire T_1-maps in *ex vivo* specimens of prostate tissue. We present data indicating that T_1 progressively decreases as the percentage of tumor increases. We display a T_1 map showing the distinction between normal and cancerous tissue. We also discuss a simple model to analyze the signal-to-noise requirements for *in vivo* imaging and present a study using agarose gel to verify the model.

7.1 Prostate cancer measurements

7.1.1 Motivation

Prostate cancer is the second leading cause of cancer deaths among men [27]. As a result of increased screening using the prostate-specific antigen blood test, digital rectal exams, and transrectal ultrasound-guided biopsies, prostate cancer can now be diagnosed at an earlier and potentially treatable stage [28]. Managing prostate cancer, however, poses a dilemma because it exhibits a great range in malignancy and is treated with approaches including "active surveillance", hormone-deprivation therapy, surgical resection, radiation, brachytherapy, radiotherapy and cryosurgery [29]. To maximize the effectiveness of these treatments, a detailed knowledge of the location and spatial extent of the cancer is needed.

High-resolution MRI (3T) using an endorectal coil for signal detection yields T_2-weighted images with good sensitivity (79%) but low specificity (55%) in determining the location of tumors due to a large number of false-positives [30]. This low specificity arises, for example, from the complications due to other tissue types in the prostate, for example, benign prostatic hyperplasia (BPH), cystic atrophy and gland poor stroma (GPS). Magnetic resonance spectroscopic imaging (MRSI) provides a non-invasive method to improve the assessment of cancer location and spatial extent [31,32], extracapsular spread [33,31,32], and aggressiveness [34]. Studies show that MRI/MRSI significantly improves the detection of cancer tissues in patients with biopsy-proven prostate cancer, but the sensitivity and specificity are comparable to MRI alone for diagnosing the presence or absence of tumors before biopsy [35]. Studies by Kurhanewicz and others demonstrate that the detection and characterization of prostate cancer can be significantly improved through the addition of diffusion tensor imaging (DTI), dynamic contrast-enhanced (DCE) imaging and quantitative T_2 imaging to perform the multiparametric T_2 MRI/^{1}H MRSI/DTI/DCE exam at 3T [9]. Unfortunately, the cost of such an exam is very high, limiting its clinical utility. Furthermore, the space restriction of the bore of a 3-T magnet makes monitoring therapy in real time difficult, and MRIs of metallic implants (such as those used in brachytherapy) at these clinical fields show image artifacts which impair tissue visualization. ULF MRI would not have these restrictions [3,4].

7.1.2 Methods

For the measurements presented in this chapter, we used the nitrogen pre-cooled litz wire prepolarization coil and the ULF MRI system as described in Chapter 4. We used the T_1-weighted spin-echo imaging pulse sequences shown in Figure 7.1 [1].

The spins are initially prepolarized in the field B_p for time t_p. Subsequently, this field is reduced to B_{ev} in which the spins evolve for time t_{ev} decaying with different rates $1/T_1$ for different tissues and magnetic fields. After turning off B_{ev}, we apply a spin echo sequence. In the experiments presented, we used $B_{ev} = B_0$, Typical parameters are: $B_0 = B_{ev} = 132$ µT (Larmor frequency of 5.6 kHz), field gradient: 50-200 µT/m, $B_p = 100$ mT, $t_p = 300$ ms, evolution time $t_{ev} = 10$-100 ms, echo time $2\tau = 30$ ms, single acquisition time 50 ms, and total acquisition time 5-10 minutes.

Using these techniques, we measured T_1 in 30 pairs of de-identified prostate tissue specimens provided by the Genitourinary Oncology / Prostate SPORE Tissue Core at the University of California, San Francisco (UCSF). The research done on the specimens obtained in this manner and presented here is not considered human subjects research. Each sample consisted of two tissue specimens, each nominally 5x5x1 mm³, but with sizes varying from approximately 3x3x1 mm³ to approximately 10x10x2 mm³. Expert gross visual inspection judged one specimen to be nominally normal tissue and the other nominally cancerous tissue. The samples were acquired immediately after surgery at UCSF, and were selected from regions of the prostate not required for patient care. Each specimen was sealed in a biohazard bag, placed on ice and transported to UC Berkeley/LBNL for NMR measurements. The bag was placed in a polystyrene holder between the prepolarizing coil and the dewar, and measurements were made 2-6 hours after surgical ligature. Throughout the experiment, the specimens were maintained at 4 °C to slow degradation.
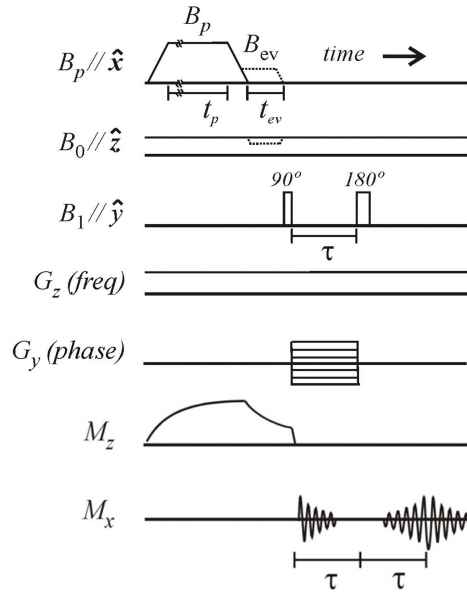
Figure 7.1. Pulse sequence for measuring the T_1 of prostate cancer. The time t_{ev} is varied. G_y is zero for cases where we do not image.

Following the prepolarization pulse, we applied a field gradient, acquired a one-dimensional projection with frequency encoding, and determined an average value of T_1 for each sample. Either 10 or 20 time delay points were acquired for each T_1 curve. Occasional system instabilities caused a fraction (~10%) of the acquisitions to have high noise. These traces were readily identified, and were removed from the averaging. We plotted the decay of the signal magnitude from each specimen versus t_{ev}. The resultant exponential decay was least squares fit to the function $y(t_{ev}) = A \exp(-t_{ev}/T_1) + y_0$. The offset y_0 was defined using the average noise 100 Hz off-resonance from the NMR peaks. The error bars are the standard deviations σ of this fit. To complement the T_1 data, we acquired a number of T_1 maps with 6 time delay points using frequency encoding and 21 phase encoding steps. The resolution was 3-4 mm. We also computed an average T_1 for each specimen represented in the T_1 maps by plotting the decay of the signal magnitude versus t_{ev}, and fitting as described for the projection data.

To obtain T_1, we examined data from the first hour of measurements, and averaged in more measurements from subsequent acquisitions when necessary to increase the SNR of the first point on the decay curve (amplitude of this point divided by y_0) to above 5. This method of constraining the exponential to the noise may reduce T_1 below its true value. We modelled this effect, and concluded that it is significant for SNR < 5, leading us to discard data from 12 of the 30 pairs of samples with SNR below 5.

After the MRI, the specimens were frozen on dry ice and returned to UCSF, where they were formalin-fixed, processed, sectioned, and stained with hematoxalin/eosin for histologic evaluation by a pathologist in order to determine percentages of tissue types present in each specimen (e.g. percent benign vs. carcinoma).

7.1.3 Results

The results of 18 pairs of specimens are summarized in Table 7.1. For each case, the specimens are labelled A, B (in one case A, B, C) in order of increasing percentage tumor, as found from the histological examination. The table shows case number, percentage of tumor, fit parameter T_1, standard deviation and contrast δ. In the majority of cases, the T_1 of the specimen with the smaller tumor percentage is higher than the T_1 of the specimen with the larger tumor percentage. There is, however, a general caveat: the histology is performed on one surface of the specimen, sampling a relatively small volume, whereas MRI samples the entire volume. Thus, it is possible for 3-dimensional structures to be under- or over-represented in the histology. While we believe that the histology generally represents the composition of the specimen, nevertheless, for a fraction of the specimens, the tumor content may be misrepresented by the histology. This possibly explains the inversion of the tumor and normal T_1 values for case numbers 14 and 17, and the outliers in Figure 7.2.

Another feature of the data is that, comparing patient to patient, there is substantial variation in T_1. For example, comparing sample 8 C (90% tumor) and 9 A (0% tumor), we find that 8 C has a higher T_1 value, even though these two cases individually show the typical trend where the T_1 for the specimen with the smaller percentage of tumor is higher than the T_1 of the specimen with the larger percentage of tumor. Variations in T_1 for (say) 100% tumor tissue may occur from patient to patient, but we emphasize that successful imaging is determined by whether there is a difference of T_1 values in a single patient. This leads us to define a figure of merit for contrast in a prepolarized ULF T_1-contrast weighted image. Following prepolarization, the magnetization decays for a time t_{ev} with time constant T_1 to its equilibrium value, which is essentially zero. Subsequently, a $\pi/2$ pulse is applied, the image is encoded, and the signal is acquired. Thus, the magnitude of the signal in an image voxel is proportional to $exp(-t_{ev}/T_1)$ If we assume tumor and

Case #	% tumor	T_1 (ms)	δ	Case #	% tumor	T_1 (ms)	δ	Case #	% tumor	T_1 (ms)	δ
1 A	2	85 ± 6	0.22	7 A	0	69 ± 8	0.36	13 A	0	56 ± 10	0.054
1 B	70	66 ± 6		7 B	20	44 ± 5		13 B	10	53 ± 1	
2 A	2	62 ± 9	0.081	8 A	0	78 ± 4	0.31	14 A	10	47 ± 4	-0.34
2 B	20	57 ± 2		8 B	20	70 ± 6	0.23	14 B	40	63 ± 3	
3 A	20	81 ± 6	0.36	8 C	90	54 ± 4		15 A	30	44 ± 3	0.068
3 B	80	52 ± 3		9 A	0	47 ± 7	0.21	15 B	60	41 ± 6	
4 A	0	54 ± 6	0.056	9 B	50	37 ± 3		16 A	25	62 ± 4	0.097
4 B	20	51 ± 4		10 A	0	56 ± 7	0.090	16 B	50	56 ± 8	
5 A	5	67 ± 4	-0.015	10 B	0	51 ± 4		17 A	0	47 ± 3	-0.19
5 B	20	68 ± 4		11 A	0	53 ± 4	0.17	17 B	30	56 ± 1	
6 A	0	62 ± 7	0.24	11 B	50	44 ± 4		18 A	0	57 ± 5	0.21
6 B	40	47 ± 4		12 A	5	75 ± 3	0.040	18 B	50	45 ± 2	
				12 B	5	72 ± 9					

Table 7.1. Percentage of tumor and relaxation times for *ex vivo* prostate specimens. Values of the contrast $\delta = 1 - T_{1B}/T_{1A}$ are also listed.

normal prostate tissue have identical proton densities, the contrast C (i.e. difference in signal intensities) between two tissues with time constants T_{1A} and T_{1B} is given by

$$C \propto exp(-t_{ev}/T_{1A}) - exp(-t_{ev}/T_{1B}). \tag{7.1}$$

Maximizing the contrast with respect to t_{ev}, and taking logarithms we obtain

$$t_{ev}(C_{max})\left(\frac{1}{T_{1B}} - \frac{1}{T_{1A}}\right) = \ln(T_{1A}/T_{1B}). \tag{7.2}$$

Setting $T_{1B} = T_{1A}(1 - \delta)$ in Equation 7.2 yields

$$t_{ev} = T_{1A}(1/\delta - 1)\ln(1 - \delta) \approx T_{1A}. \text{ (for small } \delta) \tag{7.3}$$

Finally, combining Eqs. 7.1 - 7.3, we find

$$C \propto \delta. \tag{7.4}$$

Thus, $\delta = 1 - T_{1B}/T_{1A}$ represents the maximum contrast available for two pieces of tissue with relaxation times T_{1A} and T_{1B} ($T_{1B} < T_{1A}$). The computed values of δ are listed in Table 7.1 for each sample pair. We expect two specimens with a large difference in percentage tumor to give a large value of δ, and those with tumor percentages close to each other to give a small value of δ. Although the samples are rarely 100% normal or 100% tumor, we expect an increasing trend if we examine δ versus the difference in tumor percentage.

The results of this analysis are displayed in Figure 7.2. For each specimen pair, A is the specimen with less tumor and B that with more tumor. This plot clearly shows that, in most cases, the specimen with more tumor has a lower T_1. There is a clear trend of δ upward with increasing tumor percentage difference. The least squares linear regression y=-0.004 + 0.0035x, with a correlation coefficient of 0.49. This correlation passes nearly through (0,0), indicating that, on average, the specimens pairs with similar tumor content have similar T_1 values. Extrapolating this line out to 100% difference in percentage tumor results in $\delta = 0.34 \pm 0.16$. On
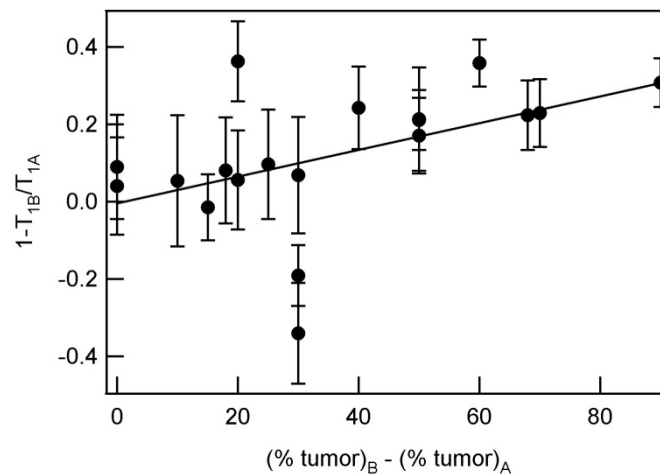

Figure 7.2. Contrast δ versus percentage tumor. Line is a linear regression to the data. Error bars are $\pm 1\sigma$.

average, therefore, we conclude that T_1 of 100% tumor is 66% that of 100% normal prostate tissue. If we remove the 3 outliers (case # 7,14,17) under the assumption that the tumor content was not represented accurately by the section on which the histology was performed, the linear regression gives y = 0.0231 + 0.0034x with a correlation coefficient of 0.86. This results in δ = 0.37 ± 0.06.

In addition to the average T_1 values listed in the table, in Figure 7.3 we display a T_1 map for case # 8, and a T_1 map of an additional large specimen, both cases of which were cut in a manner that allowed for mapping the histologic section back to the image without any ambiguity. The spatial information obtained in T_1 mapping is advantageous in identifying the T_1 of normal and cancer tissues for heterogeneous samples. Each pixel is more likely to contain only one tissue type, so that the T_1 values for each tissue type will be more accurate. The specimens were cut asymmetrically, so that the orientation is unambiguous. However, because the specimens are malleable, there is still some amount of uncertainty in the correlation between the MR image and the histology. In general, we are able to correlate the orientation and shape of the histological photograph with our T_1 map to typically ± 1 pixel. The T_1 map is constructed by acquiring six 2-dimensional images with different delay times t_{ev} between the prepolarizing pulse and the signal acquisition. Exponential fits of the decay of the signal amplitude at each pixel yield a T_1 value for each pixel in the MR image. Figure 7.3A shows a T_1 map of the 3 prostate specimens of case #8. We see that T_1 varies widely across the bottom specimen, and is relatively constant across the upper two specimens. Figure 7.3B shows the histology results for the same three specimens. For all three specimens the T_1 map reflects the tissue composition, with regions containing benign tissue having an average T_1 of 78 ms, and regions of cancerous tissue having an average T_1 of 54 ms.

Figure 7.3C shows a T_1 map of a large slice of prostate tissue. The outlined regions were identified through histology. For a specimen of this size with features this large, the alignment error of ± 1 pixel, while still large, does not eliminate the essential result. The red regions indicate tumor ($T_1 \sim 60$ ms), and green region normal ($T_1 \sim 75$ ms). As before, because the histology is performed on only a thin slice, we do not know what effects 3-dimensional
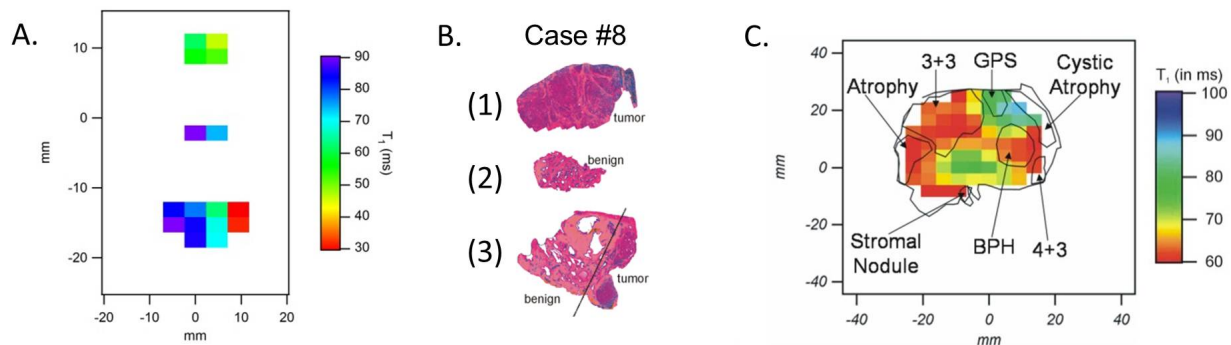
Figure 7.3. T_1 maps of prostate tissue. A: ULF T_1 map for three specimens showing average T_1 of 54 ms for the tumor and 78 ms for normal tissue. B: Histology results for the same three prostate specimens: (1) 0% tumor (2) 20% tumor and (3) 90% tumor. C: T_1 map of a larger specimen, showing variation in T_1 across the whole sample. The regions marked have been identified by histology. Numbers are Gleason score, GPS is gland poor stroma, and BPH is benign prostatic hyperplasia. Unlabeled areas are normal prostate tissue.

structures may have.   Even though other prostate tissue types such as benign prostatic hyperplasia and atrophy have T_1 values similar to those of tumor tissue, a large range of T_1 values is evident. Investigating other tissue types such as these, with a more statistically robust sample size, is a subject for future studies.

7.1.4   Discussion

Our measurements of T_1 in *ex vivo* specimen*s* of prostate tissue show that the contrast $(1 - T_{1tumor}/T_{1normal})$ scales linearly with difference in percentage of tumor tissue, with a value extrapolated to about 1/3 for 100% difference in tumor. In addition, T_1 maps clearly demonstrate the ability of ULF MRI to distinguish different tissue types. These results suggest that MR images with T_1 contrast established at ultra low magnetic field may discriminate prostate tumors from normal prostate tissue *in vivo* without a contrast agent.

This preliminary study has several limitations. An ongoing difficulty was the fact that T_1 appeared to change with time over a period of a few hours, presumably because the tissue began to decay. This decay both limited the time over which we could average the data and prevented our studying the dependence of T_1 on the evolution field B_{ev}. We limited our measurements to B_{ev} = 132 μT, but since T_1 may well depend on B_{ev} it is quite possible that a different choice could yield higher contrast. Furthermore, the fact that BPH and tumor have similar T_1 values is a potential complication for *in vivo* diagnoses. It is possible, however, that different values of B_{ev} would result in distinct values of T_1 in these tissues. Our system is able to measure T_1 at values of B_{ev} between 1 μT and 100 mT [6]. Another issue is that, to slow deterioration of the tissue, all of our specimens were maintained at about 4 °C. We do not know how the T_1 values will change at body temperature. We suspect that this limitation can be overcome only with *in vivo* studies.

On the other hand, ULF MRI has definite advantages. Our system is potentially much less confining than a conventional MRI system. If successful at discriminating prostate cancer *in vivo,* ULF MRI could be used to monitor changes in the prostate during active surveillance or therapies such as brachytherapy, avoiding the need for repeated biopsies. In the latter case, it is noteworthy that the very low imaging field enables one to acquire distortion-free images in the presence of metallic bodies [3,4]. Indeed, it may be possible to use ULF MRI to guide the placement of radioactive seeds or to target biopsies. Finally, ULF MRI may be applicable to the imaging of other types of cancer. Needless to say, the ultimate utility of this technique can be established only with *in vivo* studies.

7.2   Feasibility and requirements on B_p and SQUID noise

In this section, we explore the feasibility of using this technology to acquire images of a prostate *in vivo*.

The average distance of the prostate to the closest surface of the body (the front of the pelvic area) is 0.079 m. A conventional image of the prostate is shown in Figure 7.4. Assuming that all of our MRI equipment will be external to the body (no endorectal coils), the closest approach of our pickup coil to the prostate is 0.1 m.

Figure 7.4. Single sagittal slice of 3T MRI of the prostate (courtesy of John Kurhanewicz). The closest approach (7.9 cm) to the prostate from outside the body is from the front of the pelvic region.

According to a reciprocity principle of electromagnetism, the flux coupled to a loop of wire from a dipole $\boldsymbol{m}$ is

$$\Phi(t) = [\mu_0 \boldsymbol{\beta}(t)/4\pi] \cdot \boldsymbol{m}(t), \tag{7.5}$$

where $\mu_0 \boldsymbol{\beta}(t)/4\pi$ is the field produced at the dipole per current flowing in the loop. If we examine the voxel of volume V and magnetization M_0 a distance d along the axis of the loop of radius r, then the resulting flux from the dipole tipped into the transverse plane is

$$\Phi(t) = \frac{\mu_0}{4\pi} \frac{2\pi r^2}{(d^2 + r^2)^{3/2}} \, V M_0 \sin \omega_0 t. \tag{7.6}$$

Here, M_0 is the equilibrium magnetization of a sample of spin ½ particles of spin density ρ at temperature T_s,

$$M_0 = \frac{\rho \gamma^2 \hbar^2 B_0}{4 k_B T_s}, \tag{7.7}$$

where γ is the gyromagnetic ratio, $\hbar$ is the reduced Planck constant, and k_B is the Boltzmann constant. For the protons in water, $\rho = 6.69 \times 10^{28}$ protons/m^3. The spin density of human tissue is roughly 0.75 times that of water.   For tissue at body temperature (310 K), $M_0 = (2.34 \times 10^{-3} \text{ A m}^{-1} \text{ T}^{-1}) \, B_p$.

The amplitude of the magnetic field from this precessing voxel, averaged over the pickup loop is $\Phi/\pi r^2$

$$B_{det} = \frac{\mu_0}{2\pi} \frac{1}{(d^2 + r^2)^{3/2}} \, VM_0. \tag{7.8}$$

The variance of the fluctuating magnetic field noise of spectral density S_B (the detected flux noise that has been referred to the pickup loop) is

$$\sigma_B^2 = S_B \cdot BW = S_B/t_{acq}, \tag{7.9}$$

where BW is the bandwidth of the acquisition and t_{acq} is the acquisition time of one trace. The signal-to-noise ratio (SNR) of a single voxel from a single acquisition with no gradients is then

$$SNR_0 = \frac{B_{det}}{\sigma_B} = \frac{B_{det}\sqrt{t_{acq}}}{S_B^{1/2}} \tag{7.10}$$

assuming that the magnetization voxel does not decay over the time of the acquisition, which is a good approximation as long as $t_{acq} < T_2$.

When factoring in imaging parameters, it is easy to show that for an imagine containing N_{av} averages with N_x phase encoding steps with the G_x gradient and N_y phase encoding steps with the G_y gradient, then the SNR per voxel in the resulting image is

$$SNR_{voxel} = SNR_0\sqrt{N_{av}N_xN_y} = \frac{\mu_0}{2\pi} \frac{1}{(d^2 + r^2)^{3/2}} \frac{VM_0}{S_B^{1/2}} \sqrt{N_{av}N_xN_yt_{acq}}. \tag{7.11}$$

Incorporating the T_1 and T_2 decay factors simply changes M_0 in Equation 7.11 to M_{echo}, where

$$M_{echo} = M_0\{1 - exp[-t_p/T_1(B_p)]\} \cdot exp[-t_{ev}/T_1(B_0)] \cdot exp[-2\tau/T_2]. \tag{7.12}$$

The parameters in this equation are those of our standard pulse sequence, shown in Figure 7.1, and T_1 and T_2 are dependent on the substance. The time $T_1(B)$ is the T_1 of the material at magnetic field B. There are hidden relations in Equation 7.11, namely that the voxel volume and the number of phase encoding steps are related to the field of view, L_x and L_y, and the gradient values via the relations

$$\Delta x = L_x/N_x = \left(\frac{2\pi}{\gamma}\right)\frac{1}{2G_{x,max}\tau}, \tag{7.13}$$

$$\Delta y = L_y/N_y = \left(\frac{2\pi}{\gamma}\right)\frac{1}{2G_{y,max}\tau}, \tag{7.14}$$

$$\text{and } \Delta z = \frac{2\pi}{\gamma G_z t_{acq(after\ echo)}}, \tag{7.15}$$

where τ is the phase encoding time, $G_{x,\ max}$ and $G_{y,\ max}$ represent the maximum allowed gradients in the x and y directions respectively, G_z is the constant frequency encoding gradient, and t_{acq} (after echo) is the acquisition time after the echo occurs, which is typically roughly equal to t_{acq} - τ. The maximum available gradients are restricted due to concomitant gradient artifacts [16], however in practice it is usually the size of the field of view, the desired resolution, and SNR_0 that affect the imaging times, not the maximum gradient values.

To acquire a useful T_1 weighted image of the prostate *in vivo*, we require the CNR to be not less than 4 and the time to acquire the image to be less than 25 minutes. From our measured values of *ex vivo* prostate tissue, we assume low field $T_{1,normal} = 78$ ms, $T_{1,tumor} = 54$ ms, and high field $T_1 = 200$ ms and $T_2 = 50$ ms for both tissue types. Equation 7.3 then tells us that $t_{ev,opt} \sim 78$ ms. The field of view we require is 0.05 m in each direction, and the resolution we desire is 2 mm $\times$ 2 mm $\times$ 3 mm. We restrict the image time to 25 minutes. For our current system, with $r = 0.0325$ m, $d = 0.1$ m, this can be achieved as long as $B_p/S_B^{1/2} > 0.75 \times 10^{15}$ Hz$^{1/2}$, which can be achieved with, for example, $S_B^{1/2} = 0.2$ fT Hz$^{-1/2}$ and $B_p = 150$ mT. Both of these numbers seem achievable with enough effort.

This capability is not limited by this technology, but rather by the geometry of our current dewar and gradiometer which are not optimally sized for measuring an object 0.1 m away. The maximum flux coupling from a dipole to a loop a distance d away is when the radius of the loop is $\sqrt{2}$ d. For d=0.1 m, $r_{opt} = 0.14$ m, much larger that the inner diameter of our dewar. The increase in signal can be invested in higher resolution or lower imaging times, according to Equation 7.11.

7.3   Tumor phantom

7.3.1   Motivation

We have demonstrated significantly enhanced T_1 contrast at microtesla fields between healthy and cancerous prostate tissue *ex vivo*. From NMR measurements of healthy and cancerous prostate tissue specimens shortly after their surgical removal, we found the average T_1 of tumor to be 54 ± 5 ms and the average T_1 of healthy tissue to be 78 ± 2 ms. These values will likely change when measured *in vivo*. However we must verify that our imaging method would offer adequate contrast-to-noise ratio (CNR) to distinguish the two tissues. In this study, we analyze the present performance of our system, compare it to a simple model of the expected signal-to-noise ratios (SNRs) and CNR given the measured relaxation times of the material, described previously in section 7.2. This experiment will serve to verify the model and give credibility to the projected capabilities of a future system designed for *in vivo* prostate imaging.

7.3.2   Experiment

We developed agarose gel mixtures with relaxation times similar to those of the prostate tissue. The healthy prostate tissue is represented by 0.85% agarose gel made with 1 mM $CuSO_4$ doped water [$T_1(132 \, \mu T) = 80$ ms, $T_1(110$ mT$) = 200$ ms]. Cancerous prostate tissue is represented by 1.66% agarose gel made with 1 mM $CuSO_4$ doped water [$T_1(132 \, \mu T) = 50$ ms, $T_1(110$ mT$) = 120$ ms]. We constructed a phantom [Figure 7.5A] with various size "tumors." The resulting T_1-weighted MR image is shown in Figure 7.5B.

This image was taken with a polarizing field of 110 mT applied for 0.3 s, system noise of 1.0 fT/Hz$^{1/2}$, 101 phase encoding steps, 8 averages, frequency encoding gradient of 85 μT/m, low field delay time between polarization and imaging 35 ms, in 5.5 min total imaging time, resulting in a resolution of 1.6 x 3 x 12 mm^3.
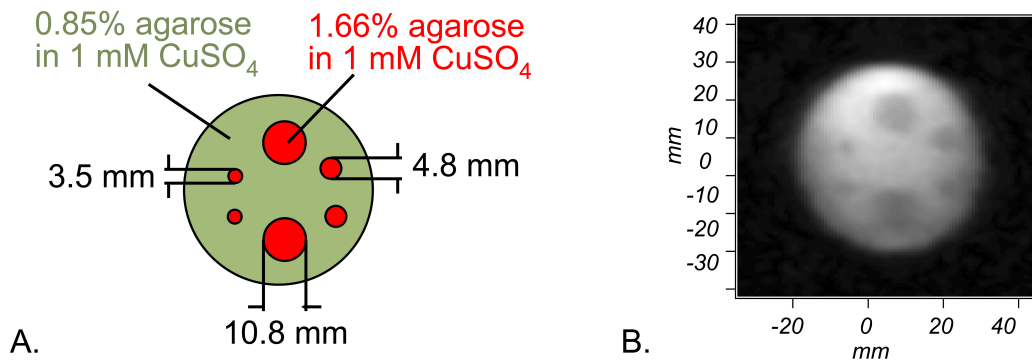
Figure 7.5. Images of agarose gel tumor phantom. A: Phantom structure. Green areas have T_1(132 µT) of 80 ms and red areas 50 ms. B: T_1-weighted MR image of phantom at 132 µT.

7.3.3 Discussion

The image has measured SNRs of 50 for the "healthy tissue" and 46 for the "cancerous tissue". From our model, we calculate the predicted SNRs to be 51 and 46, respectively, in good agreement. Along with estimates of feasible values for the future polarizing field (150 mT), system noise (0.2 $fT/Hz^{1/2}$), and estimated distance to the middle of the prostate (10 cm), we project to be able to image the prostate in 22 minutes with resolution 2 x 2 x 3 mm^3 and SNRs of 10.5 and 6.5 for healthy and cancerous tissues, respectively. These values give the same CNR as is seen in Figure 7.5B, which we believe to be adequate for differentiation.

7.4   Biological origin of T_1 difference

In collaboration with Prof. Jan Liphardt, experiments are underway to determine any biological origin of the difference in T_1 values between cancerous and normal tissues. For example, although tumors are more vascularized than normal tissue, they are less oxygenated. The resulting enhanced anaerobic processes lead to increased lactic acid production. Experiments were designed to test the various conditions known to be different between cancerous and normal tissue, including pH, level of oxygenation, hydrostatic pressure, and degree of polymer cross-linking in the extracellular matrix. Model systems fabricated from agarose gel samples will be tested first, followed by experiments with *ex vivo* tissue samples. The following are a series of experiments to be done with agarose gel.

(i) A series of agarose gel samples will be made with buffers of systematically varying pH, and T_1 will be measured as a function of pH.

(ii) A deoxygenated agarose gel sample will be made and then placed in an environment of oxygen. T_1 will be monitored as the system comes to equilibrium.

(iii) Because tumors have a higher hydrostatic pressure than normal tissue, a gel sample will be placed in a plastic container to which a controlled pressure of air can be applied. T_1 will be monitored.

(iv) Tumors secrete proteases that break down the extracellular matrix. It is possible that T_1 depends on the structural differences in the sample. A model system of extracellular matrix will be constructed, and proteases will be used to break it down. During the time for this evolution,

T_1 will be monitored. To explore further the effect of the degree of cross-linking in polymers, an agarose gel sample will be infused with sodium hypochlorite to break it down, and T_1 monitored.

7.5 Conclusion

The biggest unknown in this cancer study is whether or not the T_1 values of prostate cancer and normal tissue *in vivo* and at body temperature remain at the values we have measured at 4 °C. Further studies *in vivo* can be done to examine the magnetic field dependence of T_1 of all the different tissue types in the prostate, optimizing the value of B_{ev} at which the contrast is most enhanced. There is still much parameter space to explore, and therefore I believe after the necessary improvements in the SNR, this technology has a good chance of being useful for medical imaging.

Chapter 8

Tuning the SQUID input circuit at ULF

In our experimental setup, the input circuit to the SQUID is untuned, and therefore the SQUID is sensitive equally to signals at a large range of frequencies—up to half of the flux modulation frequency of the flux-locked loop electronics (f_m = 2 MHz for our system). The flexibility of this untuned detection can be very beneficial. It is possible to detect NMR of multiple species at the same time. In the event of extra environmental noise in the imaging band, it is very easy to change the NMR frequency in untuned detection to a better place. For measuring the characteristics of samples, such as T_1, at various low fields, the most straightforward way to do this is by changing the B_0 field throughout the whole experiment. (Another option for this experiment is to use field cycling and change B_0 only during the evolution period, but we do not have this feature enabled at this time.)

However, in some cases it may be beneficial to tune the input circuit. We employ a second-order gradiometer as the pickup coil. It is possible for large-amplitude, time-dependent, second order gradients to exceed the dynamic range of the feedback electronics but not have an effect on the NMR. This problem would be averted if the input coil of the SQUID were tuned to frequencies near the NMR frequency. Additionally, and especially at higher NMR frequencies, it is possible for the tuned circuit to have a lower magnetic field noise referred to the bottom loop of the gradiometer than untuned detection.

In the following analysis, we estimate the noise of various input circuit configurations using the parameters of the SQUID and gradiometer currently installed in our MRI system. As a standard of comparison, I will refer all noise sources to a magnetic field noise applied to the bottom loop of the gradiometer, resulting in the types of noise parameters I have been quoting throughout this dissertation. A typical noise figure for our ULF MRI system as it stands is 0.7 fT Hz$^{-1/2}$.

For the noise contributions from the SQUID, simulations [36] have shown that for an optimized device, a SQUID with resistance R shunting each junction and washer inductance L_{SQ} has a voltage noise V_N across the SQUID terminals with spectral density $S_V \approx 16\ k_B TR$ and a circulating current noise J_N with spectral density $S_J \approx 11 k_B T/R$ (k_B is Boltzmann's constant, and T is the temperature of the device). The voltage noise and current noise are correlated with cross-spectral density $S_{VJ} \approx 12\ k_B T$. The same simulations show that the maximum slope of the voltage

versus flux curve $V_\Phi \approx R/L_{SQ}$. The SQUID currently installed in the ULF MRI system has a washer inductance of $L_{SQ} = 400$ pH, shunt resistance $R = 12$ Ω, a 60-turn input coil with inductance $L_i = 1.2$ μH and a mutual inductance to the SQUID $M_i = 20$ nH. At 4.2 K, the theory predicts $V_\Phi = 3 \times 10^{10}$ s^{-1}, voltage noise $S_V^{1/2} = 0.11$ nV Hz$^{-1/2}$, and current noise $S_J^{1/2} = 7.3$ pA Hz$^{-1/2}$. The second-derivative axial gradiometer currently installed has an inductance $L_p = 1.6$ μH and a diameter of 65 mm.

8.1   Untuned input circuit

This section describes the configuration of our system at this time. Figure 8.1 shows the gradiometric pickup coil with inductance L_p connected in a superconducting circuit to the input coil of the SQUID. An applied external flux Φ_a in the pickup loop with area A_p induces a current in the input circuit of i_i. This current passes through the input coil and couples a flux into the SQUID, which is converted to a voltage across the SQUID with the multiplication of V_Φ.

From the principle of flux quantization within a superconducting loop, we relate the applied flux to the current flowing in the input circuit, and calculating the resulting voltage output:

$$V_{out} = i_i M_i V_\Phi = -\frac{M_i V_\Phi}{(L_i + L_p)}\Phi_a.$$

(8.1)

The noise sources in this configuration are the voltage noise and current noise of the SQUID. The voltage noise contribution is added to the contribution from the current noise of the SQUID. The circulating current noise induces currents in the input coil, which are then fed back to the SQUID.

A circulating current noise in the SQUID J_N will induce a flux $-M_i J_N$ in the input circuit. Using this value as the applied flux results in a voltage noise from the current noise V_N^J of

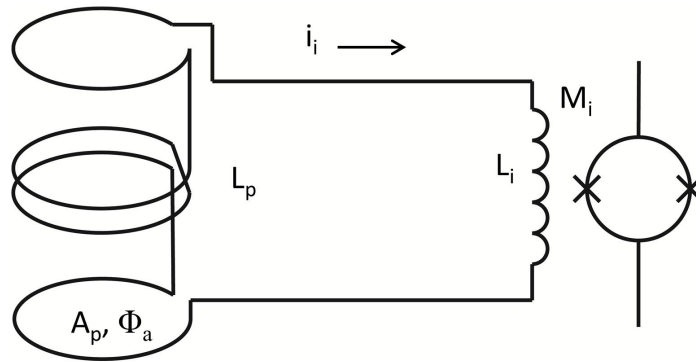$$V_N^J = \frac{M_i^2 V_\Phi}{(L_i + L_p)}J_N.$$

(8.2)

Figure 8.1. Diagram of untuned, superconducting input circuit for SQUID.

The voltage noise and current noise are correlated, resulting in a total voltage noise spectral density S_V^{tot} of

$$S_V^{tot} = S_V + \frac{M_i^4 V_\Phi^2}{\left(L_i + L_p\right)^2} S_J + \frac{2M_i^2 V_\Phi}{\left(L_i + L_p\right)} S_{VJ}. \tag{8.3}$$

Converting this to a magnetic field noise $S_B^{1/2}$ referred to the bottom loop of the gradiometer with area A_p yields

$$S_B^{1/2} = \frac{1}{A_p} \frac{\Phi_a}{V_{out}} S_V^{1/2} = \frac{1}{A_p} \frac{(L_i + L_p)}{M_i V_\Phi} \left\{ S_V + \frac{M_i^4 V_\Phi^2}{(L_i + L_p)^2} S_J + \frac{2M_i^2 V_\Phi}{(L_i + L_p)} S_{VJ} \right\}^{1/2}. \tag{8.4}$$

Using the values given in the introduction to this chapter, we find that the intrinsic magnetic field noise for untuned detection with the current device is 0.19 fT Hz$^{-1/2}$. This value is below the noise that we measure now, so we conclude that either the SQUID installed is non-optimal or we have additional external noise sources coupled in.

8.2   Input circuit with intermediate tuned circuit

The circuit we will analyze in this section (Figure 8.2) consists of two superconducting flux transformers that are coupled together by an intermediate tuned circuit. Because any resistance in the input circuit will produce substantial levels of Nyquist noise, the resistance in the circuit must be very low. In a series RLC circuit, this means that the Q of the circuit must be very high, above 20,000 in this case. However, the application of this circuit is for MRI, in which the
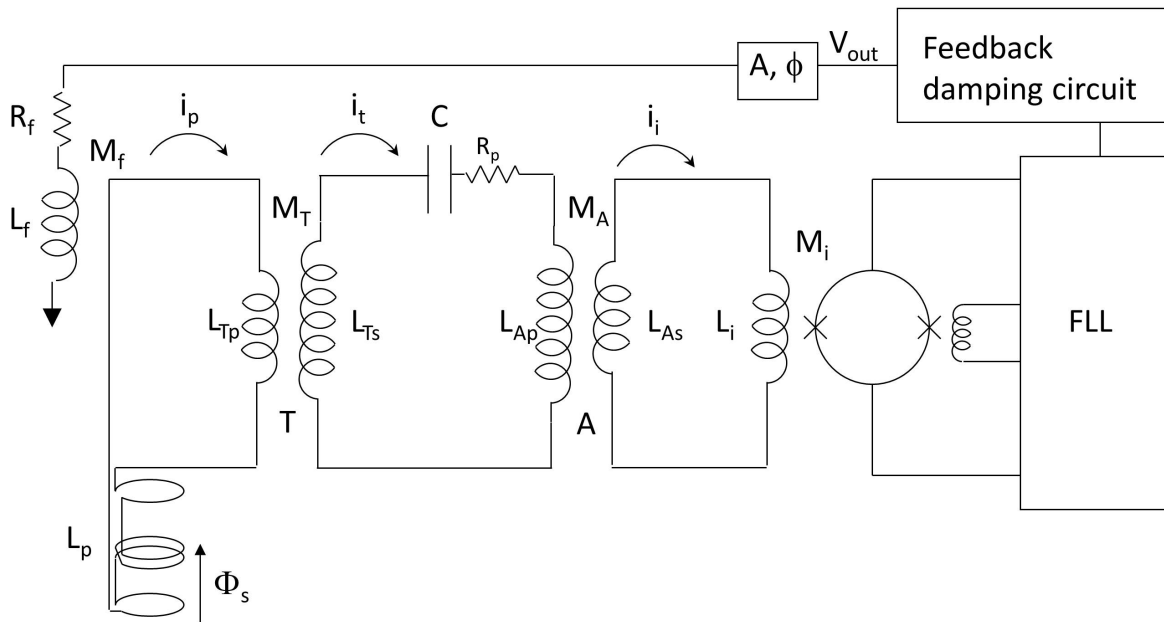

Figure 8.2. Diagram of input circuit with intermediate tuned circuit. A description of the circuit and the parameters is given in the text. FLL indicates the flux-locked loop SQUID electronics.

spectral components of the signal are spread over the imaging bandwidth by means of a frequency encoding gradient. Therefore, the effective Q of the circuit must ultimately be low enough to accommodate the imaging bandwidth. In our ULF MRI system, an imaging bandwidth of 1 kHz would be sufficient. If we assume an NMR center frequency of 10 kHz, this indicates we require a Q of 10 for imaging. To provide damping without introducing additional Nyquist noise, we apply feedback damping to the pickup coil, following Seton *et al.* [37] and Simmonds *et al.* [38]. To increase the bandwidth of the input circuit, they feed back the phase-shifted output of the flux-locked loop to cancel part of the flux in the pickup coil.

To analyze this circuit, we define the following parameters: Φ_a is the signal flux applied to the pickup loop. This causes a current i_p to flow in the superconducting pickup circuit. The pickup circuit is inductively coupled to the intermediate tuned circuit via a transformer T with inductances L_{Tp} and L_{Ts} and mutual inductance M_T. Through this transformer, the current in the pickup circuit induces a current in the tuned circuit i_t. From the principle of flux quantization within a superconducting loop, we relate the applied flux to the currents flowing in the pickup and tuned circuits:

$$\Phi_a - M_T i_t + i_p\left(L_p + L_{Tp}\right) = 0. \tag{8.5}$$

Rearranging this equation to solve for i_p yields

$$i_p = \frac{i_t M_T}{\left(L_p + L_{Tp}\right)} - \frac{\Phi_a}{\left(L_p + L_{Tp}\right)}. \tag{8.6}$$

The tuned circuit consists of superconducting inductors L_{Ts} and L_{Ap}, and a capacitor C. This circuit will have a finite Q which is represented by the parasitic resistance $R_p = \frac{1}{Q}\sqrt{L/C}$ which is likely due to the equivalent series resistance of the capacitor. The current in this circuit is coupled to a superconducting input circuit of the SQUID by another transformer A consisting of inductors L_{Ap} and L_{As} with mutual inductance M_A. This coupling causes a current i_i to flow in the input circuit of the SQUID which consists of the input coil of the SQUID L_i and superconducting inductor L_{As}. Assuming no backaction of the SQUID into the input coil, again from flux quantization, we solve for a constant flux in the superconducting input circuit:

$$-M_A i_t + i_i(L_i + L_{As}) = 0. \tag{8.7}$$

Rearranging this equation to solve for i_i yields

$$i_i = \frac{i_t M_A}{(L_i + L_{As})}. \tag{8.8}$$

Using Kirchoff's voltage law, we write the following equation to describe the tuned circuit:

$$i_t\left(j\omega L_{Ts} + j\omega L_{Ap} + R_p + 1/j\omega C\right) - j\omega M_T i_p - j\omega M_A i_i = 0. \tag{8.9}$$

Substituting i_p from Equation 8.6 and i_i from Equation 8.8, Equation 8.9 becomes

$$i_t \left(j\omega L_{Ts} + j\omega L_{Ap} + R_p + \frac{1}{j\omega C} - \frac{j\omega M_T^2}{(L_p + L_{Tp})} - \frac{j\omega M_A^2}{(L_i + L_{As})} \right)$$
$$= -\frac{j\omega M_T}{(L_p + L_{Tp})} \Phi_a. \tag{8.10}$$

The total inductance in the circuit is screened by the effects of the two superconducting circuits coupled to it. We define the term in parentheses on the left hand side of the equation to be the intrinsic impedance of the circuit, Z_i, such that Equation 8.10 becomes

$$i_t Z_i = -\frac{j\omega M_T}{(L_p + L_{Tp})} \Phi_a. \tag{8.11}$$

Solving for i_t, yields

$$i_t = -\frac{j\omega M_T}{(L_p + L_{Tp})Z_i} \Phi_a. \tag{8.12}$$

The voltage out of the SQUID V_{out} is related to the current in the input coil i_i by the mutual inductance of the input coil to the SQUID M_i and the flux-to-voltage coefficient V_Φ. Substituting in Equations 8.8 and then 8.12 yields the expression for V_{out}:

$$V_{out} = i_i M_i V_\Phi = \frac{i_t M_A M_T V_\Phi}{(L_i + L_{As})} = -\frac{j\omega M_T M_A M_i V_\Phi}{(L_i + L_{As})(L_p + L_{Tp})Z_i} \Phi_a. \tag{8.13}$$

Incorporating the feedback damping, using a feedback flux $\Phi_{fb} = V_{out} A M_f / R_f$ fed into the pickup circuit, we repeat the analysis assuming $\Phi_a \to \Phi_a + \Phi_{fb}$ and solve again for

$$V_{out} = -\frac{j\omega M_T M_A M_i V_\Phi}{(L_i + L_{As})(L_p + L_{Tp})Z_t} \Phi_a, \tag{8.14}$$

where we have defined the total impedance Z_t as adding an effective, noiseless damping resistance ΔR to the tuned circuit.

$$Z_t = Z_i + \Delta R, \tag{8.15}$$

where

$$\Delta R = A \frac{M_f M_T M_A M_i V_\Phi}{R_f (L_i + L_{As})(L_p + L_{Tp})} \omega. \tag{8.16}$$

The damping resistance has an arbitrary adjustable amplitude and phase A, and is set to be a certain value ΔR_0 at the resonant frequency necessary to give the desired imaging bandwidth. Therefore, it has the functional form $\Delta R = \frac{\Delta R_0}{\omega_0} \omega$.

Thus, Equation 8.14 relates the voltage output of the SQUID to an applied flux.

As in the untuned circuit, we now analyze the voltage noise of the circuit which will be referred to a field noise applied to the bottom loop of the gradiometer. Looking at the output voltage of the SQUID, we find two contributing noise sources: the Nyquist noise from the parasitic resistance in the tuned circuit and noise from the SQUID itself.

The parasitic resistance R_p in the tuned circuit produces a voltage noise with spectral density $4k_B T R_p$ in a circuit with impedance Z_t. The resulting current noise in the transformer circuit then causes a voltage noise across the SQUID. The spectral density of the voltage noise across the SQUID due to the Nyquist noise of the resistance S_V^R is

$$S_V^R = \frac{M_A^2 M_i^2 V_\Phi^2}{|Z_t|^2 (L_i + L_{As})^2} 4k_B T R_p.$$

(8.17)

The Nyquist noise of the resistor is uncorrelated with the SQUID noise.

For the noise contributed by the SQUID, the voltage noise contribution is added to the contribution from the current noise of the SQUID. The circulating current noise induces currents in the transformer circuit, which are then fed back to the SQUID. Assuming a circulating current noise J_N, we calculate the resulting flux noise in the pickup coil Φ_N. We then calculate the voltage resulting from that signal in the pickup coil. Going through a similar calculation as in Equations 8.5 to 8.14, except with $\Phi_a = 0$, and a flux coupled to the input circuit from the circulating current noise of $J_N M_i$ yields a flux in the pickup loop

$$\Phi_N = -\frac{M_A M_i}{M_T}\left(\frac{L_p + L_{Tp}}{L_i + L_{As}}\right)J_N.$$

(8.18)

Treating this flux as an input flux in Equation 8.14 yields a voltage noise due to the current noise of the SQUID V_N^J of

$$V_N^J = j\omega \frac{M_A^2 M_i^2 V_\Phi}{Z_t (L_i + L_{As})^2} J_N.$$

(8.19)

Thus, the spectral density of the voltage noise due to the circulating current S_V^J is

$$S_V^J = \frac{\omega^2 M_A^4 M_i^4 V_\Phi^2}{|Z_t|^2 (L_i + L_{As})^4} S_J.$$

(8.20)

Since the voltage and current noise of the SQUID are correlated, the spectral density of the voltage noise due to the correlation S_V^{corr} is

$$S_V^{corr} = -\frac{2\omega M_i^2 M_A^2 V_\Phi}{|Z_t|^2 (L_i + L_{As})^2} \times$$

$$\left[\omega\left(L_{Ts} - \frac{M_T^2}{(L_p + L_{Tp})} + L_{Ap} - \frac{M_A^2}{(L_i + L_{As})}\right) - \frac{1}{\omega C}\right] S_{VJ}.$$

(8.21)

This term vanishes on resonance.

Combining these equations yields the equation for the total voltage noise spectral density S_V^{tot} of

$$
S_V^{tot} = \frac{M_A^2 M_i^2 V_\Phi^2}{|Z_t|^2 (L_i + L_{As})^2} 4k_B T R_p + S_V + \frac{\omega^2 M_A^4 M_i^4 V_\Phi^2}{|Z_t|^2 (L_i + L_{As})^4} S_J
$$

$$
- \frac{2\omega M_i^2 M_A^2 V_\Phi}{|Z_t|^2 (L_i + L_{As})^2} \left[\omega \left(L_{Ts} - \frac{M_T^2}{(L_p + L_{Tp})} + L_{Ap} - \frac{M_A^2}{(L_i + L_{As})} \right) - \frac{1}{\omega C} \right] S_{VJ}.
$$

$$(8.22)$$

This voltage noise gives a field noise referred to the bottom loop of the pickup coil of

$$
S_B^{1/2} = \frac{1}{A_p} \frac{\Phi_a}{V_{out}} S_V^{1/2},
$$

$$(8.23)$$

where A_p is the area of one loop of the gradiometer. Minimizing $S_B^{1/2}$ with respect to the free parameters L_{As} and L_{Tp}, we find that $S_B^{1/2}$ is minimized when the two inductors in the superconducting flux transformer are equal. Specifically, we now set $L_{As} = L_i$ and $L_{Tp} = L_p$. If we also assume that the mutual inductances $M_T = \alpha_T \sqrt{L_{Tp} L_{Ts}}$ and $M_A = \alpha_A \sqrt{L_{Ap} L_{As}}$, then substituting these four relations into Equation 8.23, along with the definitions of S_V, S_J, and S_{VJ}, and $R_p = \omega_0 L_{tot}/Q$, we find

$$
S_B^{1/2} = \frac{4\sqrt{L_i L_p}}{A_p M_i V_\Phi} \frac{|Z_t|}{\omega \alpha_T \alpha_A \sqrt{L_{Ts} L_{Ap}}} \left\{ \frac{\alpha_A^2 L_{Ap} M_i^2 V_\Phi^2}{|Z_t|^2 4 L_i} 4k_B T \frac{\omega_0 L_{tot}}{Q} + 16 k_B T R \right.
$$

$$
+ \frac{\omega^2 \alpha_A^4 L_{Ap}^2 M_i^4 V_\Phi^2}{|Z_t|^2 16 L_i^2} \frac{11 k_B T}{R}
$$

$$
\left. - \frac{2\omega M_i^2 \alpha_A^2 L_{Ap} V_\Phi}{|Z_t|^2 4 L_i} \left[\omega L_{tot} - \frac{1}{\omega C} \right] 12 k_b T \right\}^{1/2},
$$

$$(8.24)$$

where

$$
L_{tot} = L_{Ts} \left(1 - \frac{\alpha_A^2}{2} \right) + L_{Ap} \left(1 - \frac{\alpha_A^2}{2} \right)
$$

$$(8.25)$$

and

$$
Z_t = j\omega L_{tot} + \frac{1}{j\omega C} + R_p + \frac{\Delta R_0}{\omega_0} \omega.
$$

$$(8.26)$$

Making the further substitutions $V_\Phi = R/L_{SQ}$, $M_i = \alpha_{SQ} \sqrt{L_{SQ} L_i}$, and collecting terms, we find

$$S_B^{1/2} = \frac{4\sqrt{L_p}}{A_p} \frac{1}{\alpha_T \sqrt{L_{Ts}}} \left\{ k_B T \frac{\omega_0 L_{tot}}{\omega^2 Q} \right.$$
$$+ \frac{k_B T L_{SQ}}{R} \left[16 \frac{|Z_t|^2}{\alpha_{SQ}^2 \alpha_A^2 L_{Ap} \omega^2} + \frac{11}{16} \alpha_A^2 L_{Ap} \alpha_{SQ}^4 \right.$$
$$\left. \left. - 6 \left(L_{tot} - \frac{1}{\omega^2 C} \right) \right] \right\}^{1/2} . \tag{8.27}$$

Equation 8.27 is independent of the SQUID inductance parameters L_i, and M_i, but still depends on $1/V_\Phi = L_{SQ}/R$ and the coupling constant for M_i, α_{SQ}. The quantity ΔR_0 is set by the required imaging bandwidth, 1 kHz. The desired Q for imaging is set by the feedback damping, $Q_{FB} = \omega_0 L_{tot}/(R_p + \Delta R_0)$. To obtain a feeling for the desired sizes of the various inductances L_{tot}, L_{Ap} and L_{Ts}, we examine Equation 8.27 on resonance, where $Z_t = R_p + \Delta R_0 = \omega_0 L_{tot}/Q_{FB}$, and the correlation term goes to zero:

$$S_B^{1/2} = \frac{4\sqrt{L_p}}{A_p} \frac{1}{\alpha_T \sqrt{L_{Ts}}} \left\{ k_B T \frac{L_{tot}}{\omega_0 Q} \right.$$
$$\left. + \frac{k_B T L_{SQ}}{R} \left[16 \frac{L_{tot}^2}{\alpha_{SQ}^2 \alpha_A^2 L_{Ap} Q_{FB}^2} + \frac{11}{16} \alpha_A^2 L_{Ap} \alpha_{SQ}^4 \right] \right\}^{1/2} . \tag{8.28}$$

From this equation, it is easy to see that the only noise term that depends on the resonant frequency is the contribution from the resistor, which decreases as the resonant frequency is increased. Assuming that $L_A \left(1 - \frac{\alpha_A^2}{2} \right) = p\, L_{tot}$ and $L_{Ts} \left(1 - \frac{\alpha_T^2}{2} \right) = (1 - p)\, L_{tot}$, Equation 8.28 becomes

$$S_B^{1/2} = \frac{4\sqrt{L_p}}{A_p} \frac{\sqrt{1/\alpha_T^2 - 1/2}}{\sqrt{(1 - p)}} \left\{ \frac{k_B T}{\omega_0 Q} \right.$$
$$\left. + \frac{k_B T L_{SQ}}{R} \left[16 \frac{(1/\alpha_A^2 - 1/2)}{\alpha_{SQ}^2 p Q_{FB}^2} + \frac{11}{16} \frac{p \alpha_{SQ}^4}{(1/\alpha_A^2 - 1/2)} \right] \right\}^{1/2} \tag{8.29}$$
.

The total inductance in the tuned circuit vanishes! Thus, the task is to make the highest Q circuit with the transformers having the highest mutual inductances possible, with only the combination of the capacitance and the total inductance entering into the calculation as the resonant frequency. Optimizing this equation for lowest field noise with respect to p, and using the parameters in Table 8.1, we find that $p_{opt} = 0.104$.

Nathan Kelso, a recent graduate of the Clarke group, undertook the task to test this tuned circuit design. We purchased high-Q 5-nF capacitors from American Technical Ceramics (part # 100E512JMS500X) with a design Q of 20,000 at room temperature. Using 4 of these in parallel to make 20 nF sets the total inductance to be 12.7 mH, $L_{Ts} = 19$ mH and $L_{As} = 2.2$ mH (recall that the sum of these two inductances will be reduced by a factor of $(1-\alpha^2/2)$ for the total

inductance). To create L_{Ts}, he wound a 2200-turn inductor from NbTi superconducting wire on a phenolic frame machined in the shape of a bobbin. When he tested the Q of the circuit at 4.2 K, he measured $Q = 60$! After various tests we concluded the phenolic frame was lossy.

Subsequently, we found a material called Rexolite® that boasts extremely low dissipation factors. To the great disappointment of Nathan, he discovered that thermal cycling machined Rexolite can cause the Rexolite to break at points of weakness. A few of his machined (and wound with 2200 turns) bobbins had one of the end caps break off during testing at 4.2 K. He found that machining the Rexolite slowly with lots of coolant, avoiding the machining sharp of angles where the end caps begin, and by cooling it slowly, the Rexolite bobbins survived. He measured a Q of 50,000 using the Rexolite frame.

The numbers we use in this calculation are given in Table 8.1. We assume the parameters of the SQUID and of the pickup coil to be fixed. The second column contains parameters that we have set or estimated. We use the measured Q of 50,000 and an estimate for well-coupled air-core transformers coupling parameter of 0.9. We set the NMR frequency to 10 kHz from our typical 6 kHz to decrease the inductor size. The capacitance is set to 20 nF but again does not enter into the calculation.

Using the values in Table 8.1, we plot Equation 8.27 versus frequency (Figure 8.3). The magnetic field noise in the imaging band is dominated by the Nyquist noise from the parasitic resistance. This contribution decreases with increasing frequency, so a higher NMR frequency would lower the total field noise.

Looking at the field noise on resonance, Equation 8.29, we now allow the resonant frequency to vary. In this case, the imaging bandwidth stays at a constant 1 kHz, and Q_{FB} varies with resonant frequency to accommodate this. We also recalculate the optimal p value at each frequency before calculating the noise at that frequency. Figure 8.4 shows the magnetic field noise versus resonant frequency. As expected, the total field noise decreases with increasing frequency. The curve for optimal p value versus resonant frequency has a similar shape, with p varying between 0.143 at $f_0 = 5$ kHz and 0.074 at $f_0 = 20$ kHz.

Fixed quantities	Estimated/desired quantities	Calculated quantities
$L_{SQ} = 400\ pH$	$\omega_0 = 2\pi \cdot 10\ kHz$	$L_{tot} = 1/\omega_0^2 C = 12.67\ mH$
$L_i = 1.2\ \mu H$	$Q = 50,000$	$L_{Ts} = 19.07\ mH$
$M_i = 20\ nH$	$Q_{FB} = 10$	$L_{Ap} = 2.21\ mH$
$\alpha_{SQ} = M_i/\sqrt{L_{SQ}L_i} = 0.913$	$\alpha_T = 0.9$	$\Delta R_0 = \omega_0 L_{tot}(Q_{FB}^{-1} - Q^{-1})$ $= 80\ \Omega$
$R = 12\ \Omega$	$\alpha_A = 0.9$	$p = 0.104$
$V_\Phi = R/L_{SQ} = 3\times10^{10}\ s^{-1}$	$C = 20\ nF$	
$L_p = 1.6\ \mu H$		
$T = 4.2\ K$		
$A_p = 0.00332\ m^2$		

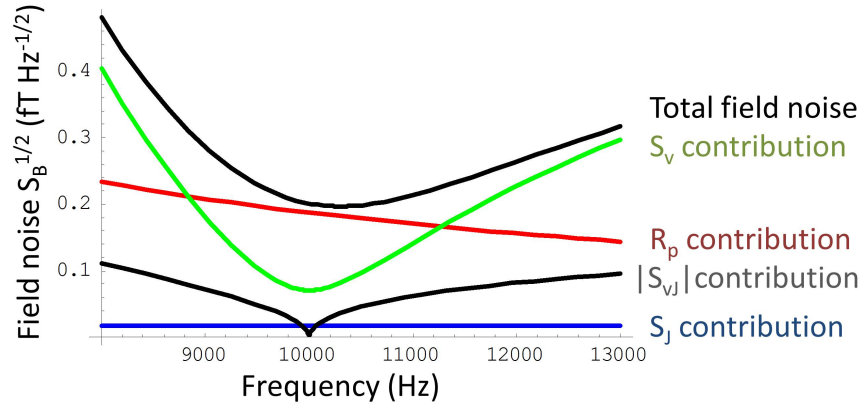Table 8.1. Parameters used in the tuned circuit calculation.

Figure 8.3. Frequency dependence of the magnetic field noise of the tuned circuit referred to the bottom loop of the gradiometer. The various curves represent the contributions from the various noise sources which add in quadrature. The dominant source of noise in the imaging band is from the parasitic resistance.
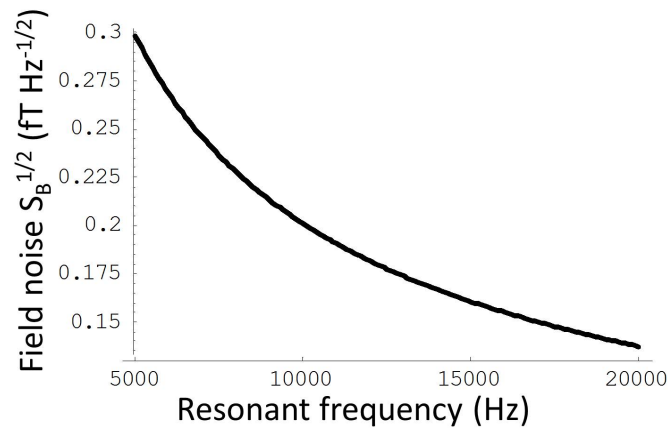

Figure 8.4. Dependence of the magnetic field noise on resonance as the resonant frequency is varied.

8.3   Simple tuned circuit

Another discussion of tuning the SQUID circuit at ULF can be found in Myers *et al*. [14] and is modeled after Seton *et al*. [37]. For the circuit described in this paper (Figure 8.5) a tuning capacitor is inserted into the untuned input circuit and feedback damping is used, as described in the previous section. The inductance of the pickup coil L_p would contribute the bulk of the inductance for tuning the circuit. The method described employs a reconstructed pickup coil which is essentially the frame of our same gradiometer with, at a resonant frequency of 10 kHz, 40 turns wound on it to increase the inductance to that required for tuning at low frequencies. The treatment here assumes that a gradiometer with 40 turns can be balanced to as high of degree as our gradiometer with 1 turn. A gradiometer with a lower balance will couple in more noise from external sources. Depending on whether the intrinsic detector noise or the external noise dominates, this may or may not be an issue. Assuming no additional external noise, this method of tuning at 10 kHz gives a field noise on resonance of 0.2 fT Hz$^{-1/2}$.
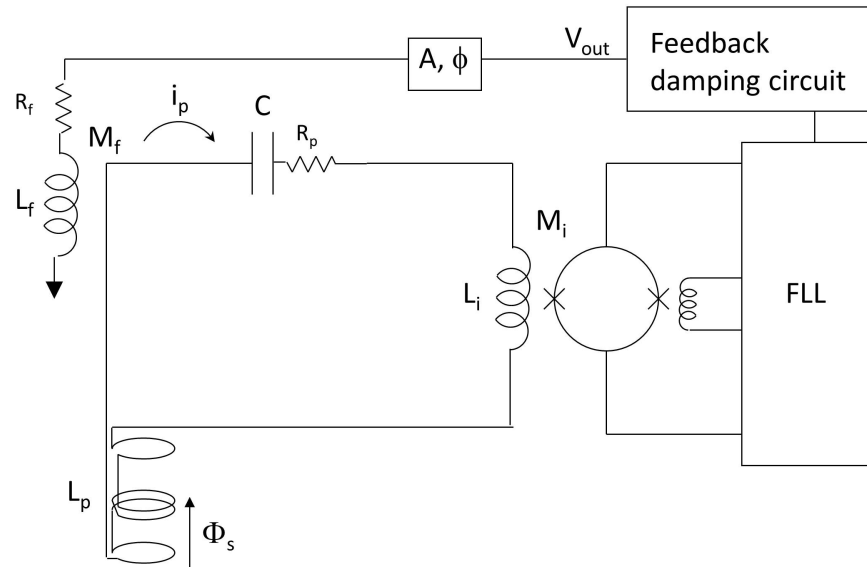
Figure 8.5. Diagram of a simple tuned input circuit. In this case, the tuning inductor is the pickup coil L_p.

8.4   Discussion

Even though the magnetic field noise of the tuned detection is not lower than that for untuned detection (0.18 fT $Hz^{-1/2}$), it may be beneficial to tune the detector for reasons other than noise. Additionally, when choosing between the two tuning methods presented here, a consideration of the contribution from the external noise and its rejection with the gradiometer is important.

When attempting to install the new water-cooled polarizing coil described in Chapter 5, the eddy currents produced in the shielded room after the coil was pulsed exceeded the dynamic range of our SQUID electronics. Because we use a second-order gradiometer that was placed vertically off-center of the shielded room, we assumed that the net signal in the gradiometer was due to a small eddy current field that would not affect the NMR, but had a high second-order gradient. In our ULF MRI system, we believe the gradiometer is rejecting external noise and did not want to degrade its balance by using the direct tuning method described in [14]. We designed this input circuit to eliminate the large, low-frequency response of the detection circuit while preserving the configuration of the pickup coil. After the design was completed, we discovered that the eddy current signals were indeed large enough to affect the NMR. After the new, thinner aluminum shield was built, the eddy current signal no longer exceeded the dynamic range of the SQUID, and we did not pursue the tuned gradiometer. Nonetheless, the tuned input circuit has considerable merit in that it rejects out-of-band noise, and might well find application in future systems. For example, since it rejects 60 Hz and its lower harmonics, it might well be feasible to operate the system with only rf shielding–for example, copper mesh–and no solid-sheet shielding.

Chapter 9

Outlook

The implementation of the water-cooled prepolarizing coil was a major step in the proof of principle of this technology to successfully image the prostate *in vivo*. Because this coil was designed as a test coil for the prepolarized MRI group at Stanford and subsequently given to us, it was not optimally designed for our application. A future *in vivo* ULF MRI system will need to include a coil that was specifically designed for this application, including the addition of turns to the inner radius of the coil. One hurdle remaining is to reduce the effective field noise of the system to 0.2 fT $Hz^{-1/2}$. At the time of this dissertation, the system noise is 0.6 fT $Hz^{-1/2}$. An improved SQUID readout system is being purchased from Star Cryoelectronics with the hope to reach 0.2 fT $Hz^{-1/2}$. An additional advantage would occur if the coupling of a sample at the distance of the prostate to the SQUID was increased. This could be accomplished by increasing the effective area of the SQUID, or by increasing the radius of the pickup coil so that it is on the order of the distance to the sample. The latter option would require a new dewar to be fabricated to accommodate the larger pickup coil, and therefore this option has not yet been pursued.

A SBIR project in collaboration with High Precision Devices (HPD) in Boulder, CO and funded by the NIH is currently underway to improve the signal-to-noise ratio of the system, to design portions of the system that will interface with patients, and to obtain approval of the system for use with human subjects from the UC Berkeley/LBNL human subjects internal review board. Among the improvements to be implemented by HPD is the replacement of all wiring passing through the shielded room with robust wiring and filtering, with the purpose of decreasing the rf noise coupled into the system. Additionally, they have contributed a heroic effort to have the system certified for use on human subjects.

Once the ULF MRI system is able to acquire *in vivo* images of the prostate, studies can then be done to measure the *in vivo* T_1 of prostate tissues at varying field strengths. Additionally, with such a system, studies of breast cancer *in vivo* can also be done fairly easily. For example, a breast cancer patient could be imaged, targeting the known location of the cancer with the goal of measuring the *in vivo* T_1 of the cancer and normal tissue. A system designed for breast cancer would be slightly different from that designed for prostate cancer, in that it would require the ability to image a larger area.

There is also the ongoing project with NIST in Boulder where they are designing standards for ULF MRI. Standard phantom are being designed for T_1 imaging, resolution, proton density, and diffusion weighted imaging. We are assisting them in the phantom design and testing the abilities in our ULF MRI system. Diffusion weighted imaging may be tested in this ULF MRI system only after dedicated gradient coils which can produce 500 mT/m are designed and integrated into the system.

Another project in progress is in collaboration with Prof. Jan Liphardt to explore possible origins of the T_1 contrast in prostate tumors that we have observed. The postdoc hired on this project, Paul SanGiorgio, will be designing phantoms to test the variation of T_1 with properties known to vary between normal tissue and tumors, such as pH, oxygenation, hydrostatic pressure, and degree of cross-linking in the extracellular matrix.

Bibliography

1 Haacke, Mark E., Brown, Robert W., Thompson, Michael R. et al. *Magnetic Resonance Imaging: Physical Principles and Sequence Design*. Wiley-Liss, 1999.

2 McDermott, R., Kelso, N., Lee, S-K. et al. SQUID-Detected Magnetic Resonance Imaging in Microtesla Magnetic Fields. *Journal of Low Temperature Physics*, **135** (2004), 793-821.

3 Mößle, Michael, Han, Song-I, Myers, Whittier R. et al. SQUID-detected microtesla MRI in the presence of metal. *Journal of Magnetic Resonance*, **179**, 1 (2006), 146-151.

4 Venook, Ross D., Matter, Nathaniel I., Ramachandran, Meena et al. Prepolarized magnetic resonance imaging around metal orthopedic implants. *Magnetic Resonance in Medicine*, **56**, 1 (2006), 177-186.

5 Koenig, S. H. and Brown, III, R. D. Relaxometry of tissue. In Gupta, R.K., ed., *NMR Spectroscopy of Cells and Organisms, Volume II*. CRC Press, Boca Raton, Florida, 1987.

6 Lee, Seung Kyun, Mößle, Michael, Myers, Whittier, Kelso, Nathan, Trabesinger, Andreas H., Pines, Alexander, and Clarke, John. SQUID-detected MRI at 132 µT with T1-weighted contrast established at 10 µT--300 mT. *Magnetic Resonance in Medicine*, **53**, 1 (2005), 9-14.

7 Packard, M and Varian, R. Free nuclear induction in the Earth's magnetic field. *Phys. Rev.*, **93** (1954), 941.

8 Clarke, John, Hatridge, Michael, and Mößle, Michael. SQUID-Detected Magnetic Resonance Imaging in Microtesla Fields. *Annu. Rev. Biomed. Eng.*, **9**, 1 (2007), 389-413.

9 Kurhanewicz, John, Vigneron, Daniel, Carroll, Peter, and Coakley, Fergus. Multiparametric magnetic resonance imaging in prostate cancer: present and future. *Current Opinion in Urology*, **18**, 1 (2008), 71-77.

10 Matter, Nathaniel I, Scott, Greig C, Grafendorfer, Thomas, Macovski, Albert, and Conolly, Steven M. Rapid polarizing field cycling in magnetic resonance imaging. *IEEE Trans Med Imaging*, **25**, 1 (2006), 84-93.

11 Clarke, John and Braginski, Alex I., eds. *The SQUID Handbook: Fundamentals and Technology of SQUIDs and SQUID Systems, Volume I*. Wiley-VCH Verlag GmbH & Co. KGaA, 2005.

12 Tinkham, Michael. *Introduction to superconductivity*. New York : McGraw-Hill, 1975.

13 Josephson, B.D. Possible new effects in superconductive tunnelling. *Physics Letters*, **1** (1962), 251-253.

14 Myers, Whittier, Slichter, Daniel, Hatridge, Michael et al. Calculated signal-to-noise ratio of MRI detected with SQUIDs and Faraday detectors in fields from 10 µT to 1.5 T. *Journal of Magnetic Resonance*, **186**, 2 (2007), 182-192.

15 Hahn, Erwin L. Spin Echoes. *Physical Review*, **80**, 4 (1950), 580-594.

16 Myers, Whittier R., Mößle, Michael, and Clarke, John. Correction of concomitant gradient artifacts in experimental microtesla MRI. *Journal of Magnetic Resonance*, **177**, 2 (2005), 274-284.

17 Kelso, Nathan, Lee, Seung-Kyun, Bouchard, Louis-S., Demas, Vasiliki, Mück, Michael, Pines, Alexander, and Clarke, John. Distortion-free magnetic resonance imaging in the zero-field limit. *Journal of Magnetic Resonance*, **200**, 2 (2009), 285-290.

18 Ungersma, Sharon E., Matter, Nathaniel I., Hardy, Jonathan W., Venook, Ross D., Macovski, Albert, Conolly, Steven M., and Scott, Greig C. Magnetic Resonance Imaging with T1 Dispersion Contrast. *Magnetic Resonance in Medicine*, **55** (2006), 1362-1371.

19 Myers, Whittier. *Potential Applications of Microtesla Magnetic Resonance Imaging Detected Using a Superconducting Quantum Interference Device*. Ph.D. Thesis. University of California, Berkeley, 2006.

20 Seton, H.C., Hutchison, J.M.S., and Bussell, D.M. Liquid helium cryostat for SQUID-based MRI receivers. *Cryogenics*, **45**, 5 (2005), 348-355.

21 Hatridge, Michael. *SQUID magnetometry from nanometer to centimeter length scales*. Ph.D. Thesis, University of California, Berkeley, 2010.

22 Clem, J. Johnson noise from normal metal near a superconducting SQUID gradiometer circuit. *IEEE Transactions on Magnetics*, **23**, 2 (1987), 1093-1096.

23 Zotev, Vadim S, Matlashov, Andrei N, Volegov, Petr L, Urbaitis, Algis V, Espy, Michelle A, and Kraus, Robert H. SQUID-based instrumentation for ultralow-field MRI. *Superconductor Science and Technology*, **20**, 11 (2007), S367.

24 Bloom, Arnold L. Field-Dependent Proton Relaxation Times in Solutions of Mn++. *Journal of Chemical Physics*, **25** (1956), 793-794.

25 Hesselink, J. R. and Press, G. A. MR contrast enhancement of intracranial lesions with Gd-

DTPA. *Radiologic Clinics of North America*, **26**, 4 (1988), 873-887.

26 Martincich, Laura, Faivre-Pierret, Matthieu, Zechmann, Christian M. et al. Multicenter, Double-Blind, Randomized, Intraindividual Crossover Comparison of Gadobenate Dimeglumine and Gadopentetate Dimeglumine for Breast MR Imaging (DETECT Trial). *Radiology*, **258**, 2 (2011), 396-408.

27 American Cancer Society. *Cancer Facts & Figures 2010*. American Cancer Society, Atlanta, 2010.

28 Han, Misop, Partin, Alan W., Piantadosi, Steven, Epstein, Jonathan I., and Walsh, Patrick C. Era specific biochemical recurrence-free survival following radical prostatectomy for clinically localized prostate cancer. *The Journal of Urology*, **166**, 2 (2001), 416-419.

29 Stamey, Thomas A. *Cancer of the prostate : an analysis of some important contributions and dilemmas*. Published for Burroughs Wellcome by Custom Pub. Services, 1982.

30 Hricak, H, White, S, Vigneron, D et al. Carcinoma of the prostate gland: MR imaging with pelvic phased-array coils versus integrated endorectal--pelvic phased-array coils. *Radiology*, **193**, 3 (1994), 703-709.

31 Scheidler, Juergen, Hricak, Hedvig, Vigneron, Daniel B. et al. Prostate Cancer: Localization with Three-dimensional Proton MR Spectroscopic Imaging—Clinicopathologic Study1. *Radiology*, **213**, 2 (1999), 473-480.

32 Wefer, A.E., Hricak, H., Vigneron, D.B. et al. Sextant localization of prostate cancer: comparison of sextant biopsy, magnetic resonance imaging and magnetic resonance spectroscopic imaging with step section histology. *The Journal of Urology*, **164**, 2 (2000), 400-404.

33 Yu, K K, Hricak, H, Alagappan, R, Chernoff, D M, Bacchetti, P, and Zaloudek, C J. Detection of extracapsular extension of prostate carcinoma with endorectal and phased-array coil MR imaging: multivariate feature analysis. *Radiology*, **202**, 3 (1997), 697-702.

34 Kurhanewicz, John, Swanson, Mark G., Nelson, Sarah J., and Vigneron, Daniel B. Combined magnetic resonance imaging and spectroscopic imaging approach to molecular imaging of prostate cancer. *Journal of Magnetic Resonance Imaging*, **16**, 4 (2002), 451-463.

35 Costouros, Nick G., Coakley, Fergus V., Westphalen, Antonio C., Qayyum, Aliya, Yeh, Benjamin M., Joe, Bonnie N., and Kurhanewicz, John. Diagnosis of Prostate Cancer in Patients with an Elevated Prostate-Specific Antigen Level: Role of Endorectal MRI and MR Spectroscopic Imaging. *Am. J. Roentgenol.*, **188**, 3 (2007), 812-816.

36 Tesche, Claudia D. and Clarke, John. dc SQUID: Current noise. *Journal of Low Temperature*

Physics, **37** (1979), 397-403.

37 Seton, H. C., Bussell, D. M., S., J. M., and Lurie, D. J. Use of a DC SQUID receiver preamplifier in a low field MRI system. *IEEE Transactions on Applied Superconductivity*, **5**, 2 (1995), 3218-3221.

38 Simmonds, M., Fertig, W., and Giffard, R. Performance of a resonant input SQUID amplifier system. *IEEE Transactions on Magnetics*, **15**, 1 (1979), 478-481.